
Università degli Studi di Ferrara

**Doctoral Course in Chemical Sciences**

**Cycle XXXVIII**

**Coordinator** Prof. Massi Alessandro

# Buried interfaces in 3rd generation photovoltaic materials: an atomistic insight

**Scientific/Disciplinary Sector (SDS) CHIM/03**

**Candidate**
Ribhu Bhatia

**Supervisor**
Prof. Simone Meloni

**Year 2022/2025**

**To my Parents**

# Acknowledgements

I would like to express my deepest appreciation and sincere gratitude to my supervisor, Prof. Simone Meloni, for his exceptional mentorship and consistent support throughout my doctoral research. I thoroughly enjoyed all the insightful discussions with him, and I am grateful for the time and thoughtful guidance he devoted to helping me develop and work on new scientific ideas, prepare presentations, and write manuscripts. His mentorship has helped me grow into a more independent researcher.

I extend my appreciation to our collaborators Prof. Gatti, Prof. Mendes, Dr. Schmitz, Dr. Emami, Eliana Loureiro and others for their contributions, expertise, and the productive discussions we shared. My sincere thanks to my current group members for all the engaging yet enjoyable discussions.

My sincere thanks to all my teachers Chandan Kumar, Mr. Vinayak Malhotra and Dr. Ramesh Kandadai for their guidance at different stages of my education.

I have been blessed to share this journey with my friends who feel like family- Shruti, Yash, Vishesh, Ritesh, Piyush, Yashita, Hrishikesh, Aquib, and Meghna. Their love, companionship, faith and reassurance have sustained and pushed me throughout my journey. I am deeply indebted to Marika and her family- Mauro, Teresa, Paolo, Noemi and Giuseppe, whose love, care, support and encouragement have been invaluable.

Last but not least, I owe the greatest debt of gratitude to my parents, Mr. Anil Bhatia and Mrs. Alka Bhatia, for their unconditional love, patience, and constant motivation. Their belief in me has been a continual source of strength throughout my life, and I remain forever grateful for their unwavering support. To my sister Ayushi, who placed my aspirations above her own, I offer my heartfelt thanks. I am also grateful to my elder cousins Stuti, Lubna, and my aunt Renu, who have always supported and encouraged me.

To all of you, my heartfelt thanks.

*"There's plenty of room at the bottom."*

- Richard P. Feynman

(Lecture at Caltech, 1959)

# Abstract

In this PhD thesis the interfacial behavior of perovskite and perovskite-inspired photovoltaic materials has been investigated using Density Functional Theory (DFT). We provide atomistic level insights on how chemical composition, crystallographic orientation and dimensionality (2D/3D) in these materials can influence charge extraction, defect formation and device stability.

Through density functional theory (DFT) simulations of the lead-free double perovskite $Cs_2AgBiBr_6$, we demonstrated that replacing the conventional Spiro-OMeTAD hole transport layer (HTL) with the 2D perovskite $(BA)_2CsAgBiBr_7$ to form a 3D/2D heterostructure significantly increases hole extraction probability. Furthermore, the 2D layer was also found to suppress defect accumulation near or at the interface. These findings were supported with the experimental results, that indicated an improved overall device efficiency when incorporating the 3D/2D architecture. In a subsequent DFT investigation, we examined the experimentally motivated lead-free BiOI/ZnO heterojunction. Our calculations revealed substantial atomic rearrangements at the interface, a phenomenon that has not been previously reported. These structural distortions were shown to generate deep defect levels within the bandgap, that can act as electron traps at the interface. While we did not conduct experimental measurements, our findings offer a theoretical explanation for reported device performances in the literature, where BiOI-based photovoltaic cells typically exhibit power conversion efficiencies below 4%.

Next, we switched to investigating the interface between mixed-cation, mixed-halide perovskites and two different hole transporting materials i.e. Spiro-OMeTAD and T2, using DFT. Our results underscore the combined influence of the crystallographic facet exposed at the perovskite surface and the choice of HTM, on hole extraction across the LHP/HTM junction. Lastly, through experimental investigation, the impact of different passivants like 2-cyclohexylethylammonium iodide (CEAI),

2-(4-fluorophenylethyl) ammonium iodide (p-FPEAI), and hexyltrimethylammonium bromide (HTAB), deposited on the perovskite under identical conditions, has been demonstrated. The champion passivated film exhibits only a 1% loss in efficiency after 1000 hours. In addition, our results also indicate that passivated perovskite/carbon architectures can enable stable hole transport layer (HTL) and gold (Au) free devices.

Overall, in this thesis, we reveal the rich diversity in interfacial behaviour of various perovskite and perovskite-inspired materials with their respective charge transport layers. These findings underscore the critical role of interfaces in governing the overall performance of photovoltaic devices.

# List of Publications

(1) F. Schmitz, R. Bhatia, F. Lamberti, S. Meloni, T. Gatti- Improved Hole Extraction and Band Alignment via Interface Modification in Hole Transport Material-Free Ag/Bi Double Perovskite Solar Cells, Solar RRL (2024). DOI: 10.1002/solr.202300965.
Status: Published

(2) F. Schmitz, R. Bhatia, F. Lamberti, S. Meloni, T. Gatti- Heavy Pnictogens-based Perovskite-Inspired Materials: Sustainable Light-Harvesters for Indoor Photovoltaics, APL Energy 1 (2023). DOI: 10.1063/5.0161023.
Status: Published

(3) S. Merchiori, A. Le Donne, R. Bhatia, M. Alvelli, J. J. Yu, X. D. Wu, M. Li, D. Li, Ł. Scheller, A. R. Lowe, M. Geppert-Rybczynska, B. A. Trump, A. A. Yakovenko, M. Chorazewski, P. Zajdel, Y. Grosu, S. Meloni- Counterintuitive Trend of Intrusion Pressure with Temperature in the Hydrophobic $Cu_2$(tebpz) MOF, Small (2024). DOI: 10.1002/smll.202402173.
Status: Published

(4) I. Poli, T. Gatti, Y. Li, A. Agresti, L. A. Castriotta, F. De Rossi, S. Shukla, T. Aernouts, S. Eslava, L. Malavasi, E. Mosconi, J. van Embden, D. Kalita, E. Della Gaspera, G. K. Grandhi, K. Mokurala, P. Vivo, N. K. Noel, J. B. Patel, M. Righetto, P. Ragonese, S. Ravishankar, C. Maurizio, F. Lamberti, K. P. S. Zanoni, M. Sessolo, M. Morales-Masis, R. Bhatia, S. Argiolas, A. Le Donne, A. Mattoni, S. Meloni, J. Baker, R. Vidal- Lead-free perovskites and derivatives for photogeneration: a roadmap to sustainable approaches for photovoltaics and photo(electro)catalysis.
Status:Accepted for publication in Journal of Physics:Energy, IOPscience

(5) R.Bhatia, S. Merchiori, S.Meloni- Photelectron extraction in BiOI:an atomistic

perspective

Status: Under review with Journal of Materials Chemistry A

(6) R.Bhatia, S.Meloni- Interfacial behavior of Spiro-OMeTAD and T2 hole transport materials(HTMs) across crystallographic facets in hybrid lead halide perovskites

Status: Under Preparation

# Contents

# 1 Introduction

In the last decade, the global demand for sustainable energy solutions has accelerated rapidly. This is driven by mounting concerns over climate change, rising greenhouse gas emissions, and the finite nature of fossil fuels. Photovoltaics (PV) has emerged as a cornerstone technology in this context being lightweight, scalable, and capable of harnessing the sun's and indoor light energy. While crystalline silicon (c-Si) remains the dominant commercial PV technology on a global production scale, it faces intrinsic limitations such as relatively slow and high energy consumption manufacturing, rigid module formats, and a theoretical efficiency limit of $\sim 29\%$ [1]. These constraints have motivated the pursuit of next-generation thin-film technologies that promise lower cost, greater flexibility, and novel device architectures.

Over the past decade, lead halide perovskites (LHP's) have displayed phenomenal advancements (figure 1) in power conversion efficiency (PCE) for both indoor and outdoor applications [1–3]. In fact, the most efficient LHP devices now outperform the industry standard multi-crystalline silicon solar cells under standard test conditions [3]. Classical LHPs (see figure 2 (a)) possess the stoichiometry $ABX_3$, where the A-site is occupied by an organic or inorganic monovalent cation such as methylammonium (MA), formamidinium (FA), or cesium (Cs); the B-site is occupied by lead ($Pb^{2+}$); and X is a halide ($I^-$, $Br^-$, or $Cl^-$) [4]. The structure consists of three dimensional network of corner sharing $BX_6$ octahedra with A cations in the center of these octahedra. This unique arrangement not only stabilizes (figure 2 (c)) the structure but also allows fine tuning of the optoelectronic properties [5] in these materials (figure 2 (d) shows some general properties).

More recently, LHPs with mixed cations and halide anions have attracted increasing attention because their pure counterparts viz. $MAPbI_3$, $FAPbI_3$, and $CsPbI_3$ exhibit several disadvantages [6]. For instance, a fundamental issue with $MAPbI_3$ based perovskite solar cells (PSC's) is their rapid degradation when exposed to light,

oxygen, and humidity [7]. This degradation has been attributed to a chemical reaction between oxygen and the MA cation under the presence of excess electronic charge in the perovskite [7, 8]. FA based perovskites exhibit a superior stability than their MA based analogues [9, 10].

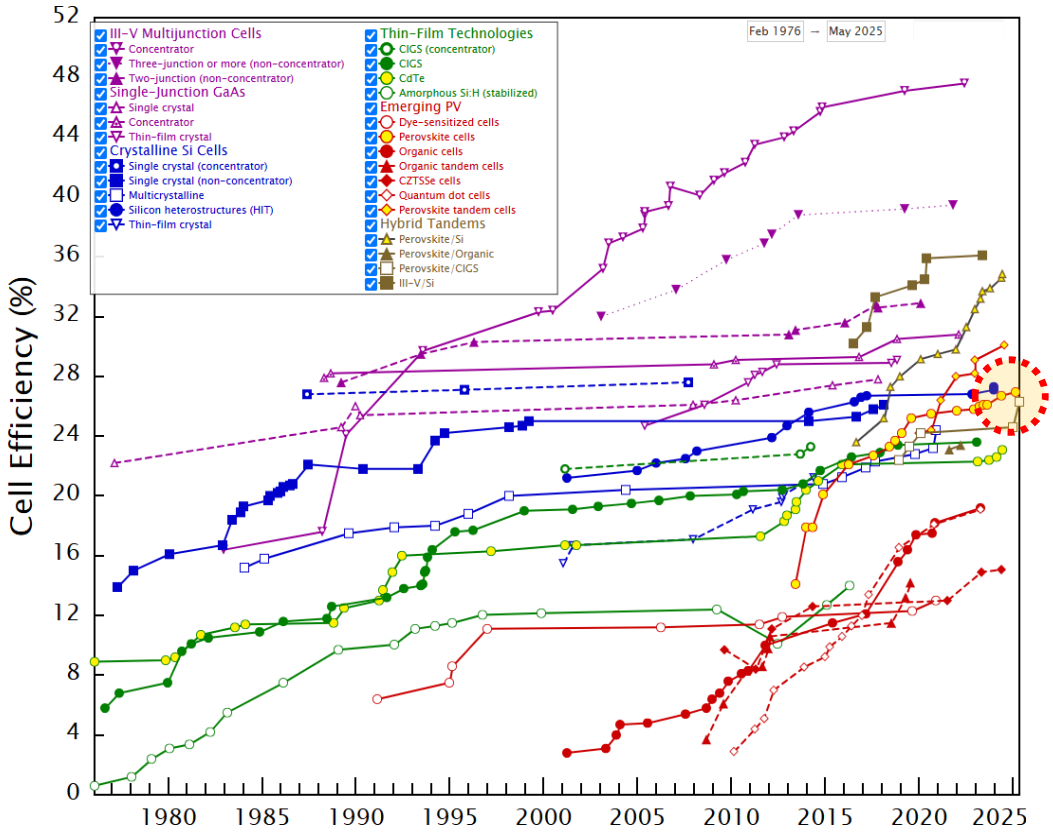


Figure 1: Best Research-Cell Efficiency Chart [3]. Highest efficiency of PSC's has been encircled.

Moreover, compared to $MAPbI_3$, the $FAPbI_3$ cells also exhibit reduced band gap ($\sim$ 1.48 eV) and lower defect density [11, 12], factors which are resposible for its superior efficiencies [13]. But one big obstacle is that $FAPbI_3$ is not thermodynamically stable in its black perovskite phase ($\alpha$-phase) and exhibits a structural transition to the yellow non-perovskite $\delta$-phase at room temperature [14–17]. However, when a part of $MA^+$ or $FA^+$ are substituted with $Cs^+$, the phase stability is dramatically improved

[18] along with further reduction in trap-state density, thereby enhancing the performance and reproducibility of PSC's [9, 10]. Unfortunately, intrinsic factors alone are not enough to produce the best devices, their architectures play a very important role as well. In perovskite solar cells, two main device architectures have become standard, as illustrated in figures 3(a-b): (i) the electron transport layer/perovskite/hole transport layer stack (n-i-p), and (ii) the hole transport layer/perovskite/electron transport layer stack (p-i-n) [19, 20]. In the n-i-p configuration, an electron transport layer (ETL) is deposited first onto the transparent conductive oxide (TCO), which causes the TCO to function as the negative electrode. Conversely, in the p-i-n configuration, the hole transport layer (HTL) is deposited first, so the TCO serves as the positive electrode. Although both architectures have achieved state of the art power conversion efficiencies surpassing 25% for n-i-p and approaching the same benchmark for p-i-n devices [21, 22], they each exhibit distinct advantages and limitations. The n-i-p structure often benefits from high temperature processing of compact or mesoporous ETLs, yielding good interfacial contact and efficient charge extraction. However, it typically relies on doped organic HTMs (e.g., Spiro-OMeTAD), which have been associated with long-term instability. In contrast, p-i-n architectures commonly use low temperature, solution processed ETLs (e.g., fullerene derived materials) that are more compatible with flexible substrates and scalable fabrication, and they reduce reliance on dopants [23, 24]. Nonetheless, p-i-n devices may suffer from increased non-radiative recombination at the perovskite/ETL interface, difficulty achieving high-quality perovskite crystallization on top of organic HTLs, and challenges in obtaining high fill factors and stable long-term performance [23, 25, 26]. Therefore, even though both configurations have displayed excellent efficiencies, substantial opportunities remain to optimize interface quality, carrier selectivity, stability, and scalability. A deeper understanding of interfacial energetics, passivation strategies, and transport layer design is essential to further enhance the performance and long term durability of both architectures.

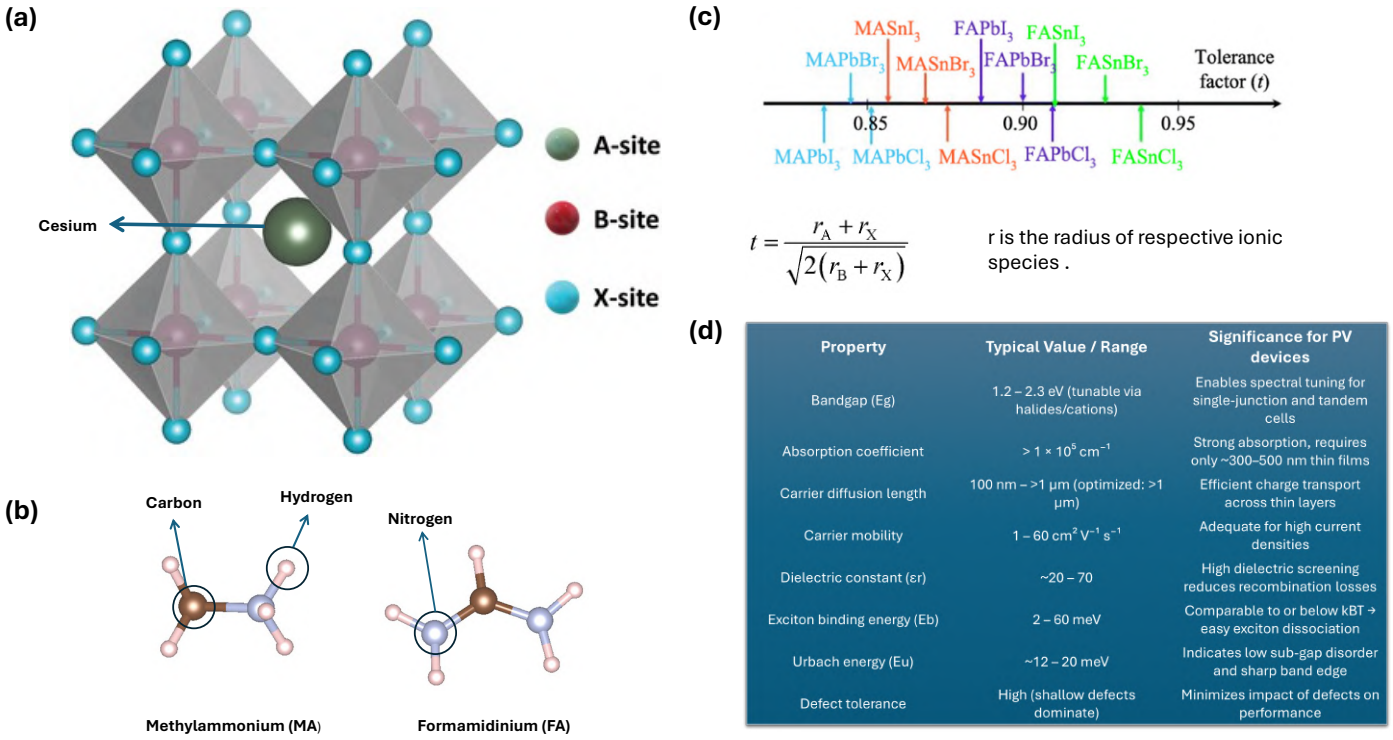


Figure 2: (a) Perovskite in cubic phase [27, 28]; (b) $A^+$ site cations; (c)Tolerance factor (t) of various perovskite absorbers (nearing 1-more stable and ideal cubic phase); (d)Properties responsible for exponential growth of perovskite based solar cells.

Central to the performance and longevity of PSC's, are the buried interfaces between the perovskite absorber layer and the adjacent charge transport layers [29, 30]. These buried interfaces play a decisive role in governing phenomenon like charge extraction, carrier recombination, and energy level alignment, which consequently affect operational parameters like the open-circuit voltage ($V_{oc}$), short-circuit current density ($J_{sc}$), fill factor (FF), and the overall PCE of PSCs [19, 29, 31]. Moreover, these interfaces are often the initiation points for degradation processes that can compromise the long-term stability of devices [32–35]. The strategic design and engineering of these buried interfaces have therefore become a major focus of research [36–39].

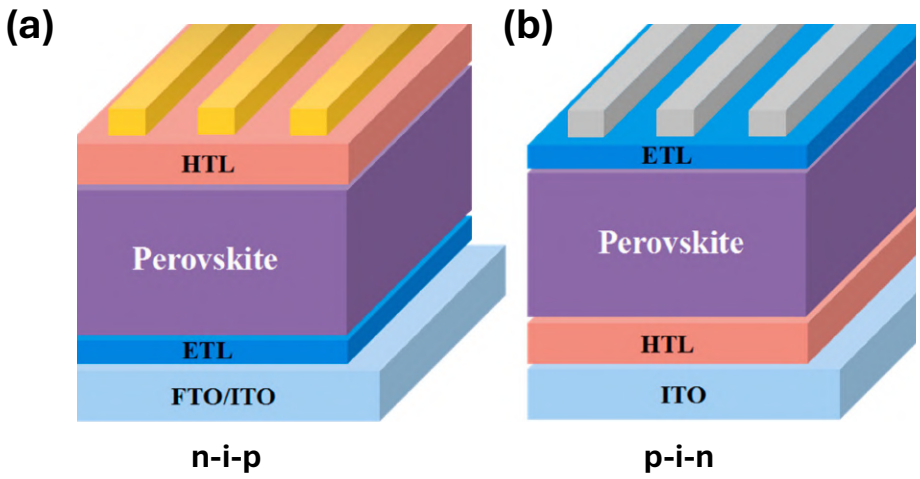


Figure 3: Commonly deployed architectures in perovskite solar cells [40]

Apart from this, there remains an ongoing debate concerning the toxicity of lead, which pose serious challenges for (i) terawatt-scale deployment, (ii) environmental and operational stability under ambient air, and (iii) indoor applications where human exposure is likely [41–44]. Although significant efforts have been made to mitigate these concerns through encapsulation strategies, over a 25 year utility timescale, perovskite solar cells remain far from full scale practical realization [1, 45–47]. Consequently, there is a pressing need to explore alternative materials that preserve the desirable optoelectronic properties [1, 48, 49] of lead halide perovskites while eliminating toxicity concerns. Lead free derivatives (see figure 4) have emerged as promising candidates, though their efficiencies remain considerably lower than their lead based counterparts [50]. Examples include tin based perovskites ($ASnX_3$), bismuth and antimony based halides (e.g., $Cs_3Sb_2I_9$)[51, 52], bismuth oxyiodide (BiOI)[42, 53], and double perovskites (DPs) such as $Cs_2AgBiBr_6$ [54, 55]. These materials expand the compositional landscape but also introduce new challenges: perovskites cell based on tin suffer from $Sn^{2+}$ oxidation and associated defect generation [56–58]; DPs often exhibit indirect bandgaps or high trap densities that limit their efficiency[59, 60]; BiOI's layered morphology can hinder intimate contact with charge transport layers [42]; and $Cs_3Sb_2I_9$ exhibit low carrier

mobility and are often prone to defects that introduce deep level trap states along with poor film morphology [42]. In the case of lead free materials, along with these intrinsic drawbacks, interfacial challenges that were already central in LHP's, play an equally important role. Indeed, these inspired materials present greater interfacial complexity than their lead-based counterparts, further underscoring the pivotal role of interface engineering in realizing efficient and stable perovskite-inspired photovoltaic devices.

Although experimental probes such as UPS, XPS, PL, or Kelvin probe provide valuable averaged or surface sensitive information, they cannot directly reveal the microscopic origins of interfacial barriers, trap states, dipoles, adsorption geometries, or the impact of specific defects and terminations. Fortunately, with continued advances in computational power, algorithms and simulation techniques, computational research has become increasingly effective in understanding and complementing experiments. Density functional theory (DFT) in particular, can provide atomic scale insights into the structural, electronic, and chemical properties that are difficult to access experimentally and therefore serve as a crucial bridge between experiment and theory. In this thesis DFT was used to model interfaces and surfaces of perovskites and inspired materials. The following sub-section presents an overview of the objectives reached.

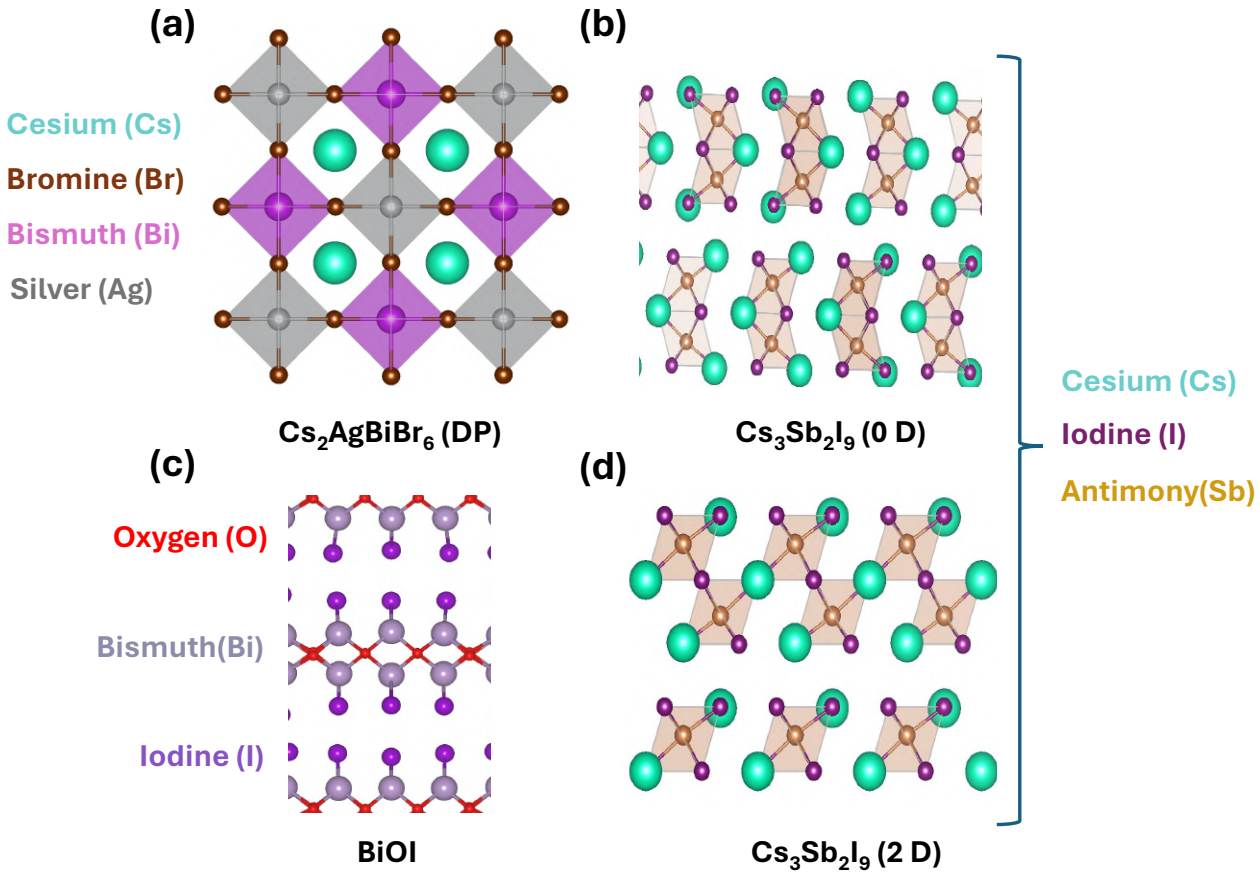


Figure 4: Perovskite Inspired Materials.

## 1.1 Thesis Overview

This thesis deals with various types of perovskite interfaces based on the kind of atomic or molecular species constituting the perovskite structure and explains the complex interplay between structure and properties in these materials. Starting with the $Cs_2AgBiBr_6$ inspired material, in chapter 4, the effect of substituting Spiro-OMeTAD, the most common hole transport layer (HTL), with a 2D $(BA)_2CsAgBiBr_7$ such that one obtains a 2D/3D (D-dimensional) mixed interface, is explored in the context of potential lead free and HTL-free photovoltaic applications. Using DFT, we showed that the presence of the 2D perovskite phase enhances the hole extraction probability

and prevents defects from accumulating at the interface. Next in chapter 5, we studied the ZnO/BiOI interface, where BiOI is another 2D material and ZnO is an electron transport layer, examining its atomistic and electronic structure, and interfacial charge transfer characteristics. We confirmed that, to transfer from bulk BiOI to bulk ZnO and be extracted, the electrons need to overcome an additional energy barrier, besides the one that has been reported in the literature [61, 62]. This barrier which has never been reported before, is a consequence of major atomic re-arrangements at the BiOI/ZnO interface. Switching to lead halide perovskites, in chapter 6, we present an investigation of the structural and electronic properties of interface between mixed-cation, mixed-anion lead halide perovskites with two different hole transporting layers (HTLs), such as Spiro-OMeTAD and T2. The aim here was to understand how HTL's interact with different facets of the perovskite and eventually compare the performance of these HTL's based on the electronic structure. Lastly, we present the outcomes of experimental studies regarding the role of different passivating agents between the HTL and the perovskite surface. Anticipating the results, we find that the chosen passivant deposited on top of the perovskite's surface not only improves the efficiency of the solar cell but also the stability, since after 1000 hours, we observed only 1% drop in efficiency. In addition to identifying the best passivant among the chosen ones, we also fabricated HTL and gold free cells with perovskite/passivant/carbon configuration, that exhibited excellent long term stability.

Overall, in this thesis, DFT simulations corroborated by experimental observations, reveal the rich diversity in interfacial behaviour among various perovskite and perovskite-inspired materials with their respective charge transport layers. These findings further underscore the critical role of interfaces in governing the overall performance of photovoltaic devices.

# 2 Theoretical Formalism and Methods

In quantum mechanics, all physically accessible information about a system is encoded in its wave function, or equivalently in its eigenstates and associated eigenvalues. The knowledge of the quantum mechanical ground states enables us to evaluate a wide range of structural, electronic, energetic, and mechanical properties for diverse systems, including thin films, surfaces, and bulk materials [63, 64]. However, the main challenge lies in determining the ground state, as one must solve a many-electron problem. More specifically, this involves solving the time-independent Schrödinger equation for a system with $n$ electrons and $N$ nuclei:

$$\hat{H}\Psi_i(x_1, x_2, \ldots, x_n, r_1, r_2, \ldots, r_N) = E_i\Psi_i(x_1, x_2, \ldots, x_n, r_1, r_2, \ldots, r_N), \tag{1}$$

where $x_i$ is the position of the $i^{\text{th}}$ electron, $r_I$ is the position of the $I^{\text{th}}$ nucleus, $\hat{H}$ represents the Hamiltonian operator, and $E_i$ is the corresponding energy eigenvalue of the $i^{\text{th}}$ state $\Psi_i$. The total Hamiltonian accounting for various interactions in such systems is given by:

$$\begin{aligned}\hat{H}_{\text{tot}} =& -\frac{1}{2M_I}\nabla_I^2 - \frac{1}{2}\sum_i \nabla_i^2 + \frac{1}{2}\sum_{i\neq j}\frac{1}{|x_i - x_j|} + \frac{1}{2}\sum_{I\neq J}\frac{Z_I Z_J}{|r_I - r_J|} - \sum_{i,I}\frac{Z_I}{|x_i - r_I|} \\ =& -\hat{T}_N - \hat{T}_e + \hat{V}_{ee} + \hat{V}_{NN} - \hat{V}_{eN}\end{aligned} \tag{2}$$

Here, $M_I$, $r_I$, and $Z_I$ are the mass, position, and charge of the $I^{\text{th}}$ nucleus, respectively, while $x_i$ denotes the position of the $i^{\text{th}}$ electron. (All quantities are expressed in atomic units unless stated otherwise.) Uppercase subscripts refer to nuclei, while lowercase subscripts denote electrons. The first two terms represent the kinetic energy of the nuclei and electrons, respectively, while the remaining terms account for electron-electron, nucleus-nucleus, and electron-nucleus interactions.

This Hamiltonian can be simplified if one takes advantage of significant differences between the nuclei and electron masses. Nuclei being heavier move much slower than electrons. Practically, atleast to a good approximation, one can consider electrons as

moving in the field of fixed nuclei. This approximation is called the *Born-Oppenheimer approximation* (BOA) [65]. Since the nuclei are fixed, their kinetic energy is 0 and the potential energy due to nucleus-nucleus repulsion is a constant. Thus, the first (nuclear kinetic energy) and fourth (nuclear-nuclear interaction) terms can now be neglected. The Hamiltonian reduces to that of electrons moving in the field of fixed nuclei (i.e., an external potential):

$$\begin{aligned} \hat{H}_{\mathrm{e}} &= -\frac{1}{2}\sum_{i}\nabla_i^2 + \frac{1}{2}\sum_{i\neq j}\frac{1}{|x_i - x_j|} - \sum_{i,I}\frac{Z_I}{|x_i - r_I|} \\ &= -\hat{T}_e + \hat{V}_{ee} - \hat{V}_{eN} \end{aligned} \tag{3}$$

The condition $i \neq j$ under the second summation ensures that self-interaction is avoided. Despite this simplification, solving the electronic Schrödinger equation remains practically impossible for most systems, due to the complex electron-electron interactions and the correlated motion of electrons:

$$\hat{H}_e \Psi_i^e(x_1, x_2, \ldots, x_n) = E_i^e \Psi_i^e(x_1, x_2, \ldots, x_n) \tag{4}$$

In this context, the development of *density functional theory* (DFT), first proposed by Hohenberg and Kohn [66] and later formulated in the Kohn-Sham scheme [67], represents a breakthrough. DFT replaces the complex many-body wavefunction, which depends on $3N$ spatial coordinates for a system of $N$ electrons, with the much simpler electron density $n(\mathrm{r})$, which depends only on three spatial variables. This reduction in complexity enables DFT to achieve an excellent balance between computational efficiency and accuracy [68]. In contrast to wavefunction based approaches such as Hartree-Fock (HF) or post-HF methods (e.g., configuration interaction or coupled-cluster theory), whose computational cost scales steeply with system size (typically as order- $\mathcal{O}(N^4)$-$\mathcal{O}(N^7)$), modern implementations of DFT scale roughly as $\mathcal{O}(N^3)$, making it feasible for systems containing hundreds to thousands of atoms [69, 70].

Furthermore, the introduction of the Kohn-Sham formalism allows for the treatment of exchange-correlation effects through suitable approximations, such as the local density approximation (LDA), generalized gradient approximation (GGA), and hybrid functionals, yielding results that are in remarkable agreement with experimental observations for a broad range of materials [67, 71]. Consequently, DFT has become popular for investigating the structural, electronic, optical, and vibrational properties. In the following sections I will briefly discuss the origin of DFT and the aforementioned approximations within it.

## 2.1 Hohenberg and Kohn Theorems

Hohenberg and Kohn (H-K), in 1964 [66], published a seminal paper in which they proposed and proved two theorems to formulate DFT as an exact theory for the ground state of many-body fermionic systems.

***Theorem 1***

*For any system of interacting particles in an external potential* $V_{ext}(\mathrm{r})$*, the potential* $V_{ext}$ *is determined uniquely, except for a constant, by the ground-state particle density* $n_0(\mathrm{r})$*. Therefore, all properties of the system are completely determined if* $n_0(\mathrm{r})$ *is known.*

***Theorem 2***

*A universal functional for the energy* $E[n]$ *in terms of the density can be defined for any external potential* $V_{ext}(\mathrm{r})$*. For any particular* $V_{ext}(\mathrm{r})$*, the exact ground-state energy of the system is the global minimum value of this functional, and the density* $n(\mathrm{r})$ *that minimizes the functional is the ground-state density* $n_0(\mathrm{r})$*.*

These two theorems reduce the number of variables of a function from $3N$ to 3 variables (in $n(\mathrm{r})$). This means that the calculation of the ground-state energy of an

$n$-electron system is no longer a function of a $3N$-dimensional wavefunction but rather the three-dimensional electronic density. Since the total energy is a functional of the ground-state electron density, the theory is known as density functional theory. The functional is given by:

$$E_{\mathrm{HK}}[n] = T[n] + E_{\mathrm{ee}}[n] + \int d\mathrm{r}\, V_{\mathrm{ext}}(\mathrm{r}) n(\mathrm{r}),$$

where $T[n]$ and $E_{\mathrm{ee}}[n]$ are the kinetic and potential energies of the interacting electron system. These theorems by H-K made a significant contribution toward calculating the ground-state energy by reducing the minimization problem from $3N$ to 3 dimensions[69, 70].

## 2.2 Kohn-Sham Ansatz

Although the H-K theorems greatly simplified the electronic Hamiltonian, they do not provide a practical scheme for determining the ground state electron density or the energy of an interacting electron system. In 1965, Kohn and Sham (KS)[67] proposed an ansatz to determine the ground-state electron density $n_0(\mathrm{r})$, expressed as follows:

$$n_0(\mathrm{r}) = \sum_{i=1}^{N_e} \phi_i^{\mathrm{KS}*}(\mathrm{r})\, \phi_i^{\mathrm{KS}}(\mathrm{r}) \tag{5}$$

This equation expresses that the exact ground state electron density $n_0(\mathrm{r})$ can be constructed as the sum of densities from single particle KS orbitals $\phi_i^{\mathrm{KS}}(\mathrm{r})$. These orbitals may be viewed as auxiliary variables, more specifically a mathematical construct that allows the electron density to be represented as $|\phi_i^{\mathrm{KS}}(\mathrm{r})|^2$ and are not meant to represent the true many body wavefunction.

Furthermore, the total energy can now be written as:

$$\begin{aligned} E_{\mathrm{KS}}[n] &= T_s[n] + \frac{1}{2}\iint \frac{n(\mathrm{r})\, n(\mathrm{r}')}{|\mathrm{r}-\mathrm{r}'|}\, d\mathrm{r}\, d\mathrm{r}' + \int V_{\mathrm{ext}}(\mathrm{r})\, n(\mathrm{r})\, d\mathrm{r} + E_{\mathrm{xc}}[n] \\ &= T_s[n] + E_{\mathrm{Hartree}}[n] + E_{\mathrm{ext}}[n] + E_{\mathrm{xc}}[n], \end{aligned} \tag{6}$$

where $T_s[n]$, $E_{\mathrm{Hartree}}[n]$, and $E_{\mathrm{xc}}[n]$ are the kinetic energy, Hartree (Coulomb) energy, and exchange correlation energy, respectively. By choosing to use non interacting auxiliary single-particle wavefunctions, the kinetic term can be rewritten as a sum over single particle orbitals rather than as a functional of the electron density.

By rewriting the kinetic contribution in this form, the single particle KS Hamiltonian, which can be solved self consistently (see figure 5), is given by:

$$\hat{H}_{\mathrm{KS}}\, \phi_i^{\mathrm{KS}}(\mathrm{r}) = \left[-\frac{1}{2}\nabla^2 + \hat{V}_{\mathrm{KS}}(\mathrm{r})\right] \phi_i^{\mathrm{KS}}(\mathrm{r}) = \varepsilon_i\, \phi_i^{\mathrm{KS}}(\mathrm{r}) \tag{7}$$

where $\hat{V}_{\mathrm{KS}}(\mathrm{r})$ is the Kohn-Sham potential accounting for all electronic interactions:

$$\hat{V}_{\mathrm{KS}}(\mathrm{r}) = \hat{V}_{\mathrm{Hartree}}(\mathrm{r}) + \hat{V}_{\mathrm{ext}}(\mathrm{r}) + \hat{V}_{\mathrm{xc}}(\mathrm{r}) \tag{8}$$

In this approach, the external potential includes contributions from electron-nuclei interactions and other applied fields. The Hartree potential accounts for the Coulomb interaction that each electron experiences. However, the exact form of the exchange-correlation potential, which incorporates all remaining electron-electron interactions including exchange effects arising from the Pauli exclusion principle and dynamic electron correlation is unknown. Since the exact functional form of $V_{\mathrm{xc}}(\mathrm{r})$ is unknown and expected to be highly complex and possibly non-analytical, approximate exchange-correlation functionals must be employed for this method to be applicable. In the following section, these approximations will be discussed in detail.

***Local Density Approximation (LDA)***: In this approximation, the exchange-correlation energy density at each point is the same as that of a homogeneous electron gas of the same density. In this form the exchange-correlation energy functional simply is given by:

$$E_{xc}^{\mathrm{LDA}} = \int d\mathrm{r}\, n(\mathrm{r})\, \epsilon_{xc}^{\mathrm{homo}}(n(\mathrm{r})), \tag{9}$$

where $\epsilon_{xc}^{homo}(n(r))$ is the exchange-correlation energy per particle of a homogeneous electron gas of density $n(r)$. The LDA neglects corrections to the exchange-correlation energy that arise from spatial inhomogeneities in the electron density around a given point r. As a result, it often provides reasonably accurate descriptions for weakly correlated systems such as semiconductors and the homogeneous electron gas. However, in complex systems, where the electron density changes rapidly, its accuracy decreases leading to significant errors in properties such as bond energies and lengths due to the inadequate treatment of density gradients and nonlocal effects [67, 70].

***Generalized-Gradient Approximation (GGA)***: One of the approaches that was introduced to improve LDA was the GGA, where the exchange-correlation potential is a functional of the local electronic density and its gradient:

$$E_{xc}^{\mathrm{GGA}} = \int d\mathrm{r}\; n(\mathrm{r})\, \epsilon_{xc}\left(n(\mathrm{r}), \nabla n(\mathrm{r})\right) \tag{10}$$

The GGA functional by Perdew, Burke and Ernzerhof (PBE) [71, 72] is the most widely used functional to simulate periodic materials with DFT as it features no empirical fitting parameters. A modification of PBE is the PBEsol [73] functional, which is often used to calculate equilibrium properties of bulk solids and their surfaces. The revised PBE (revPBE)[74] functional is an extension of the PBE functional with some extra fitting parameters and is typically used to simulate liquids, i.e. water. Although GGA functionals tend to agree for small gradient magnitudes, for the cases where the gradient of the electronic density is large the level of agreement is far less. In

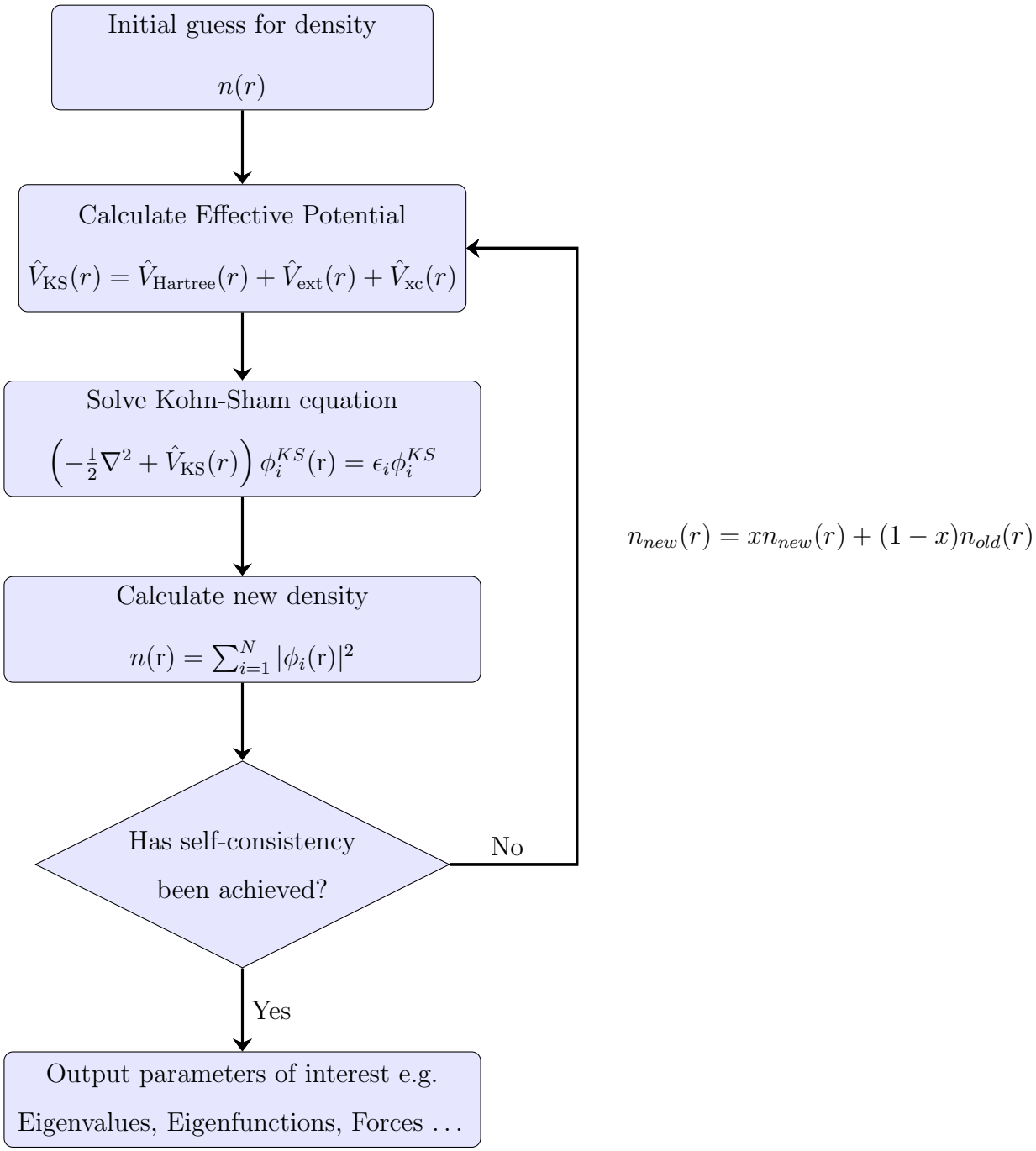


Figure 5: Flowchart illustrating the self-consistency loop of the Kohn-Sham equations.

such cases GGA may even perform worse than the LDA approach. However, most DFT calculations reported in the present thesis were performed using the PBE functional.

***Hybrid Functionals***: Hybrid functionals generally offer more reliable results than standard DFT because they combine the strengths of two different approaches. In these methods, a portion of the exact exchange from Hartree-Fock theory is mixed with the exchange-correlation term from a conventional DFT functional. Hartree-Fock itself represents the many-electron system using a single Slater determinant, which captures exchange effects accurately but neglects electron correlation. As a result, pure Hartree-Fock performs poorly for crystalline systems and greatly overestimates band gaps. On the other hand, local and semilocal DFT functionals tend to underestimate band gaps because of their approximate treatment of exchange and correlation. Hybrid functionals balances between these two errors, leading to band gaps that more closely match experiment. The HSE functional, in particular, improves accuracy by using a screened Coulomb interaction, implemented through an error-function decomposition to include exact exchange only at short range, making the approach more practical for periodic systems.

$$E_{xc}^{\mathrm{HSE}} = aE_x^{\mathrm{HF,SR}}(\omega) + (1-a)E_x^{\mathrm{PBE,SR}}(\omega) + E_x^{\mathrm{PBE,LR}}(\omega) + E_c^{\mathrm{PBE}} \tag{11}$$

where $a$ is the mixing parameter, $\omega$ is an adjustable parameter controlling the extent of short-range interactions, $E_X^{HF,SR}(\omega)$ is the short-range Hartree-Fock exact exchange functional, $E_X^{PBE,SR}(\omega)$ and $E_X^{PBE,LR}(\omega)$ are the short and long range components of the PBE exchange functional, and $E_C^{PBE}(\omega)$ is the PBE correlation functional. For $\omega$= 0 the HSE exchange-correlation functional reduces to the PBE0 hybrid functional. For most systems, $a = 14$ and $\omega = 0.2$ (referred to as HSE06)[75, 76], gives accurate results. While HSE improves accuracy for many materials, its high computational cost limits its routine use to moderately sized systems. Since in this thesis all the systems are large in size, I refrained from using hybrid functionals.

## 2.3 DFT in Periodic and Non-Periodic Systems

The self-consistent Kohn-Sham procedure is often implemented using the plane-wave pseudopotential method, which is well suited for periodic solids. In this approach, Bloch's theorem [77] is applied to periodic systems, allowing each Kohn-Sham orbital to be expressed as a sum of plane waves. For the periodic system, the Bloch wave function $\psi_{nk}$ of an electron in the $n^{th}$ band can be described as Bloch's electron, containing periodic cell function $u_{nk}(r)$ and a plane wave $e^{ikr}$.

$$\psi_{nk}(r) = e^{i\mathrm{k}\cdot\mathrm{r}}\, u_{nk}(r), \tag{12}$$

where k is the wave vector confined to the first Brillouin zone. The periodic cell function can further be expressed as the linear combination of plane waves in reciprocal space:

$$u_{nk}(\mathrm{r}) = \sum_{\mathrm{G}} c_{nk}(G) e^{i\mathrm{G}\cdot\mathrm{r}}, \tag{13}$$

where $G$ is the reciprocal lattice vector and $c_{nk}$ is the expansion coefficient. By combining the above two equations, the K-S orbitals can be expressed as the infinite sum of plane waves:

$$\psi_{nk}(\mathrm{r}) = \sum_{\mathrm{G}} c_{nk} e^{i(\mathrm{k}+\mathrm{G})\cdot\mathrm{r}} \tag{14}$$

In practice, the infinite plane-wave expansion of the Kohn-Sham orbitals is truncated by introducing an energy cutoff $E_{\mathrm{cut}}$, such that only plane waves satisfying

$$\frac{1}{2}|\mathbf{k}+\mathbf{G}|^2 \leq E_{\mathrm{cut}}$$

are included. This limits the number of reciprocal lattice vectors G in the basis and makes the calculation computationally feasible. For periodic systems, additional efficiency is gained by exploiting the point group symmetries of the lattice, which reduce the required Brillouin zone sampling to the irreducible Brillouin zone (IBZ). Proper choices of $k$-points in the IBZ and $E_{\text{cut}}$ are crucial for efficient and accurate DFT calculations. For instance, in metallic systems, where the Fermi surface introduces sharp discontinuities, a dense k-point mesh is essential, whereas insulators and semiconductors generally require fewer k-points. The most widely used scheme for generating k-point meshes is the Monkhorst-Pack method [78, 79], which defines a uniform grid according to:

$$\mathrm{k}(i,j,k) = \frac{2i - N_1 - 1}{2N_1}\,\mathrm{b}_1 + \frac{2j - N_2 - 1}{2N_2}\,\mathrm{b}_2 + \frac{2k - N_3 - 1}{2N_3}\,\mathrm{b}_3, \tag{15}$$

where $\mathrm{b}_1$, $\mathrm{b}_2$, and $\mathrm{b}_3$ are the reciprocal-lattice vectors and $i = 1, \ldots, N_1$, $j = 1, \ldots, N_2$, and $k = 1, \ldots, N_3$. This method ensures systematic sampling of the Brillouin zone and allows straightforward convergence testing. Convergence with respect to k-points is typically assessed by gradually increasing the grid density until the total energy changes by less than a pre-defined tolerance. For example, semiconductors may converge well with a $6 \times 6 \times 6$ mesh, while metals often require denser grids such as $12 \times 12 \times 12$ or higher. Another important consideration is the size of the simulation cell. When a super-cell containing $N$ primitive cells is used, the reciprocal lattice vectors shrink by a factor of $1/N$, reducing the effective size of the Brillouin zone. Consequently, fewer k-points are needed for convergence, and in very large supercells a single $\Gamma$-point calculation is often sufficient without significant loss of accuracy.

For slab and surface calculations, which are commonly used to model catalytic activity, adsorption, or thin-film growth, the periodicity of the system is effectively two-dimensional. The slab model consists of a finite number of atomic layers stacked along one direction, separated by a large vacuum region to decouple periodic images. In such cases, dense k-point sampling is required only in the two in-plane directions ( say $k_y$, $k_z$), while the out-of-plane direction ($k_x$) corresponds to the vacuum and

contains no periodic dispersion. Therefore, it is sufficient to sample this direction with a single k-point:

$$N_{k_x} = 1, \tag{16}$$

This significantly reduces computational cost without sacrificing accuracy. For instance, a surface calculation may employ a grid such as $1 \times 6 \times 6$, where the "1" explicitly accounts for the vacuum direction. This reduction is justified because additional k-points in the vacuum direction do not contribute to the description of electronic states, as the wavefunctions decay exponentially into the vacuum and no band dispersion occurs along that axis. Thus, a careful selection of k-point meshes is essential for reliable DFT simulations.

Furthermore, besides representing the K-S orbital as the finite sum of plane-wave, the pseudopotential approximation (illustration in figure 6) is implemented to reduce the number of basis functions required, by dividing the electrons as core and valence. In DFT calculations, core electrons are not treated explicitly (frozen core) since they do not significantly participate in bonding or determine the low-energy physical properties of the system, whereas valence electrons are treated explicitly. There are several schemes for constructing pseudopotentials viz. norm-conserving [80], ultrasoft [81]and projector augmented wave (PAW)[77, 82] methods. The norm-conserving pseudo-potential preserves the norm of the all-electron valence wave function within the core region and accurately reproduce its behavior outside the core. In ultrasoft pseudo-potential, there is no constraint of the norm conservation and uses lower cutoff energy for the convergence.

The PAW method transforms the rapidly oscillating all-electron wavefunctions into smooth pseudo-wavefunctions, while still allowing full reconstruction of the true all-electron states when needed. This transformation is expressed as:

$$|\Psi\rangle = |\tilde{\Psi}\rangle + \sum_i (|\phi_i\rangle - |\tilde{\phi}_i\rangle)\langle\tilde{p}_i|\tilde{\Psi}\rangle$$

where $|\Psi\rangle$ is the all-electron wavefunction, $|\tilde{\Psi}\rangle$ is the smooth pseudo-wavefunction, $|\phi_i\rangle$ and $|\tilde{\phi}_i\rangle$ are the all-electron and pseudo partial waves respectively, and $\langle\tilde{p}_i|$ are

the projector functions linking them. Within the core region, the method restores the full nodal structure using the partial waves, while outside this region, only the smooth pseudo-wavefunction is used. Thus, PAW combines the accuracy of all-electron methods with the efficiency of pseudo-potential approaches, making it one of the most powerful techniques for electronic structure calculations.

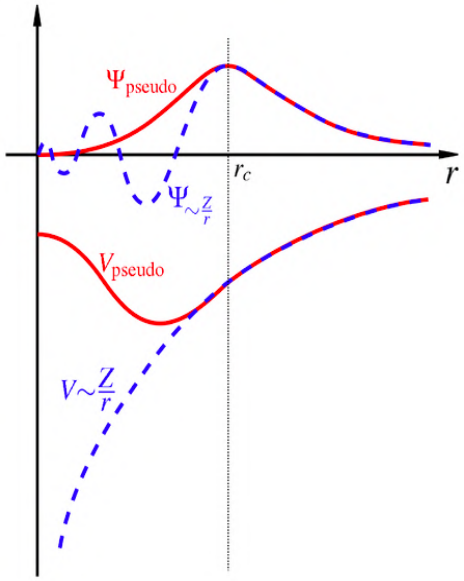


Figure 6: Schematic representation of an all electron potential (dotted line) and pseudopotential (solid line) along with corresponding wavefunctions[70]

While the use of pseudopotentials and the PAW method significantly reduces the computational cost without sacrificing accuracy, standard DFT calculations still suffer from well-known limitations arising from the approximate nature of exchange-correlation (XC) functionals [83–85]. In particular, conventional local or semi-local XC functionals such as LDA or GGA often fail to capture weak long-range dispersion (van der Waals) interactions and tend to underestimate the localization of strongly correlated $d$ and $f$ electrons. To overcome these shortcomings, various correction schemes such as dispersion-corrected DFT (DFT-D, vdW-DF [86, 87]) and on-site Coulomb interaction corrections (DFT+U) [88], are employed to improve the description of both

non-covalent interactions and localized electronic states, thereby extending the applicability of DFT to a broader range of materials.

## 2.4 Dispersion Corrections

Dispersion forces, also referred to as van der Waals (vdW) forces, can be classically seen as the instantaneous interactions between dipoles induced by charge fluctuations. The vdW interactions between atoms and molecules decay rapidly with the distance between interacting particles as $R^{-6}$ and play an important role in many chemical systems. These interactions are missing in the standard exchange-correlation functionals used in DFT and are essential for accurately describing weakly bonded materials or molecular adsorption on surfaces. Although several methods have been developed to include these dispersive interactions in DFT calculations [86, 89–93]. In this thesis, I have used the parameterized DFT-D3 scheme of Grimme [89] , where the dispersion energy $E_{disp}$ is simply added to the Kohn-Sham DFT energy $E_{KS\text{-}DFT}$. The DFT-D3 is preferred for perovskites and 2D/3D interfaces because it better balances long-range van der Waals attraction and short-range repulsion, preventing overbinding and yielding more accurate lattice parameters and interfacial binding energies [94**?** ]. The total energy with dispersion correction is given as:

$$E_{DFT\text{-}D3} = E_{KS\text{-}DFT} + E_{disp} \tag{17}$$

where $E_{disp}$ is the dispersion correction, expressed as follows:

$$E_{\text{disp}} = -\frac{1}{2}\sum_{i=1}^{N_{at}}\sum_{j=1}^{N_{at}}\sum_{\mathbf{L}}{}' \left( f_{d,n}(r_{ij,L})\,\frac{C_n^{ij}}{r_{ij,L}^n} + f_{d,n}(r_{ij,L})\,\frac{C_n^{ij}}{r_{ij,L}^n} \right) \tag{18}$$

where, $N_{at}$ is the number of atoms, the $C_n^{ij}$ is the $n^{th}$ order dispersion coefficient and unlike DFT-D2 [95], here they are calculated on the basis of the coordination

number around atoms $i$ and $j$. Furthermore, $f_{d,n}$ is the damping function expressed as:

$$f_{d,n}(r_{ij}) = \frac{s_n}{1 + 6(r_{ij}/(s_{R,n}R_{0ij}))^{-\alpha_n}} \tag{19}$$

where $R_{0ij} = \sqrt{\frac{C_{nij}}{C_{nij}}}$, the parameters $\alpha_n$, $s_n$ are adjustable parameters whose values depend on the choice of the exchange-correlation functional [96].

## 2.5 DFT + U Correction

DFT with semi-local functionals is inadequate in systems with partly filled $d$ or $f$ shells where on-site Coulomb interaction is very important, because of oversimplified treatment of exchange and correlation in an averaged way. Such systems are called strongly correlated systems and usually contain transition metal or rare-earth metal elements. When the on-site Coulomb repulsion(characterized by the Hubbard U in Hubbard Model)is large compare with the valence bandwidth(characterized by the overlap integral in Hubbard Model), hopping of electrons between metal ions will not happen, electrons will be localized and the system is an insulator. DFT with semi-local functionals often cannot obtain the right ground state for such systems, either finding a metallic state when the ground state is an insulator, or obtaining an insulator state with much smaller band gap than the true ground state. DFT+U [97] is a correction to DFT that adds a Hubbard-like orbital dependent penalty term to the total energy expression and can account for the strong on-site repulsion for the localized $d$ or $f$ electrons in the system. The total energy expression for DFT+U in Dudarev's formalism has the following form:

$$E^{\mathrm{DFT}+U} = E^{\mathrm{DFT}} + \frac{U - J}{2} \sum_{\sigma} \left[ \sum_{j} n_{jj}^{\sigma} - \sum_{j,l} n_{jl}^{\sigma} n_{lj}^{\sigma} \right] \tag{20}$$

Here, $U$ and $J$ are the on-site Coulomb and exchange parameters, respectively.

The indices $j$ and $l$ denote the magnetic quantum numbers, while $\sigma$ represents the spin index. The quantity $n_{jl}^{\sigma}$ is the on-site density matrix of the localized shell under consideration. Similar to the simple one-dimensional Hubbard model, this Hubbard-like penalty term enforces the on-site density matrix to possess eigenvalues of either 0 or 1, which physically implies that fully occupied or fully unoccupied states are favored. In this formulation, $U$ and $J$ do not appear separately but rather combine into a single effective Hubbard parameter $U_{\text{eff}} = U - J$[96]. This effective parameter can be obtained either from ab initio calculations or estimated semi-empirically. In Chapter 5, where I studied the BiOI/ZnO interface, the use of appropriate U parameters led to a theoretical bandgap estimation close the experimentally reported ones. The detailed values and outcomes have been discussed in the chapter. However, even with improved functionals, DFT results require further analysis tools to extract chemically and physically meaningful quantities. These are described in the next chapter.

## 2.6 Software and Implementation

Having established the theoretical foundations of DFT, it is now appropriate to describe the computational framework used to implement these methods in practice. All calculations presented in this thesis were carried out using the Vienna Ab-initio Simulation Package (VASP), a widely used DFT code for electronic structure calculations. In VASP, the Kohn–Sham equations are solved using a plane-wave basis set together with the projector augmented-wave (PAW) method. The software also supports a broad range of exchange-correlation functionals including LDA, GGA, hybrid functionals, and van der Waals-corrected approaches, although, as noted earlier, the GGA formalism was employed throughout the calculations in this thesis. VASP has capabilities to peform geometry optimization, electronic structure analysis, phonon calculations, molecular dynamics, and band-structure and density-of-states computations,

making it a powerful and versatile tool for investigating the structural and electronic properties of diverse material systems.

Structure optimization ensures that atomic positions correspond to a local minimum of the potential energy surface. VASP provides several ionic relaxation schemes [98], among which the quasi-Newton [99, 100] and conjugate gradient methods [101, 102] are the most widely used. These algorithms determine how atomic coordinates are updated during relaxation. Due to the rigorous implementation in this thesis, I will briefly describe the theory behind only the conjugate gradient method.

**Conjugate Gradient (CG) Method for Geometry Optimization**: The CG method constructs a series of search directions that are mutually conjugate with respect to the Hessian of the total energy, thereby leading to significantly faster convergence. The atomic positions $\{\mathrm{R}_i\}$ are updated iteratively by moving along a sequence of optimized search directions. The force on atom $i$ is given by

$$\mathrm{F}_i = -\frac{\partial E}{\partial \mathrm{R}_i}, \tag{21}$$

where $E$ is the Kohn-Sham total energy. In a simple steepest-descent method [103, 104], the search direction at iteration $k$ would be chosen as the negative gradient $\mathrm{g}_k = -\mathrm{F}_k$. However, CG improves this by defining search direction $\mathrm{d}_k$ that combines the steepest-descent direction with information from previous iterations:

$$\mathrm{d}_k = -\mathrm{g}_k + \beta_k \mathrm{d}_{k-1} \tag{22}$$

The coefficient $\beta_k$ ensures that the new direction is conjugate to all previous directions, which avoids revisiting already-optimized degrees of freedom. Different choices of $\beta_k$ exist, but in VASP the Polak–Ribière formulation [105] is used:

$$\beta_k^{\mathrm{PR}} = \frac{\mathrm{g}_k(\mathrm{g}_k - \mathrm{g}_{k-1})}{\mathrm{g}_{k-1} \cdot \mathrm{g}_{k-1}} \tag{23}$$

Once the direction is defined, an energy line minimization is performed along $\mathrm{d}_k$

to determine an optimal step length $\alpha_k$. The updated atomic positions are then:

$$\mathrm{R}_i^{(k+1)} = \mathrm{R}_i^{(k)} + \alpha_k \mathrm{d}_k \tag{24}$$

This procedure is repeated until the specified convergence criteria on the maximum force, energy change, and atomic displacement is satisfied.

In practice, the CG algorithm is used to optimize atomic positions while the electronic ground state is typically obtained using a separate algorithm such as Davidson [106] or blocked-Davidson for solving the Kohn-Sham equations. VASP, for example, can use CG to minimize the ionic forces while repeatedly recalculating the electronic structure until self-consistency is achieved at each ionic step. Overall, the CG method is quite robust for structural relaxation calculations, enabling us to determine the equilibrium geometries for molecules, surfaces, solids, and complex interfaces.

# 3 Post-Processing and Performance Evaluation descriptors

This section provides a brief theoretical overview of the performance descriptors employed throughout this thesis. These include quantities like the density of states (DOS), work function (WF), binding energy (BE), and electron localization function (ELF) etc, that are fundamental for interpreting the electronic and interfacial behavior.

## 3.1 Electron Localization Function (ELF)

Introduced by Becke and Edgecombe [107], the electron localization function (ELF) is a dimensionless quantity that represents the likelihood of finding an electron in the vicinity of another electron of the same spin. This is unlike the electron density $\rho(\mathrm{r})$, which only reflects the overall distribution of electrons ie. it does not distinguish between localized or delocalized electrons.

Defined as the ratio between the local Pauli kinetic energy density and that of a homogeneous electron gas:

$$ELF(\mathrm{r}) = \left[1 + \left(\frac{D(\mathrm{r})}{D_h(\mathrm{r})}\right)^2\right]^{-1}, \tag{25}$$

where $D(\mathrm{r})$ is the excess kinetic energy density due to the Pauli exclusion principle, and $D_h(\mathrm{r})$ is the kinetic energy density of the homogeneous electron gas with the same electron density. The value of ELF between pairs of atoms provides insights into the nature of chemical bonds between atoms. For light elements-like C, O, H etc. ELF values in the domain between atoms in the range $\sim 0.8 - 1$ are a signature of covalent bonding, moderate values $\sim 0.6 - 0.8$ are indicative of polar covalent interaction and low to moderate values $\sim 0 - 0.6$ implicate empty spaces and predominantly no bonding or ionic interaction. For example, in ionic crystals like NaCl, ELF highlights

the localization of electrons around anions (see figure 7 (b)). In this thesis I utilized ELF in chapter 5 to visualize bonding evolution going from bulk of the structure to the interface.

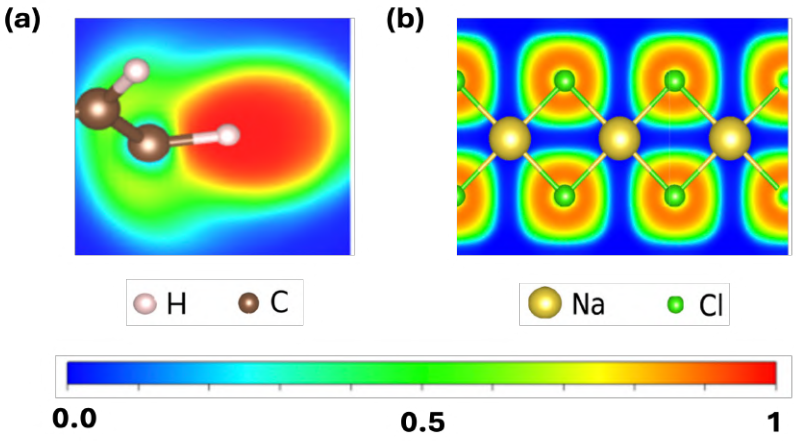


Figure 7: Typical ELF contours; a) Covalent C-H bonding;b) Ionic Na-Cl bonding. The images have been adapted from [108]

## 3.2 Rumpling and Rougness

At surfaces and interfaces, atoms may relax from their ideal bulk positions due to broken symmetry and altered bonding environments. A common measure of such structural relaxation is *rumpling* (see figure 8), which refers to the relative displacement between cations and anions within a single atomic plane perpendicular to the surface.

Quantitatively, the rumpling $\Delta z$ (in Å) is defined as

$$\Delta z = z_{\text{cation}} - z_{\text{anion}}, \tag{26}$$

where $z_{\text{cation}}$ and $z_{\text{anion}}$ denote the average positions of cations and anions along the surface normal. A positive value implies that cations are displaced outward with respect to anions, while a negative value indicates the opposite. This displacement modifies

the surface dipole moment and can thereby alter surface properties such as the work function, band alignment, and adsorption energies. In perovskite oxides and halide perovskites this can also influence the growth of over layers, the anchoring of adsorbates, and the energetics of interfaces with charge transport layers in devices. More broadly, rumpling is a measure of how atomic-scale relaxations give rise to electronic effects [87, 109, 110].

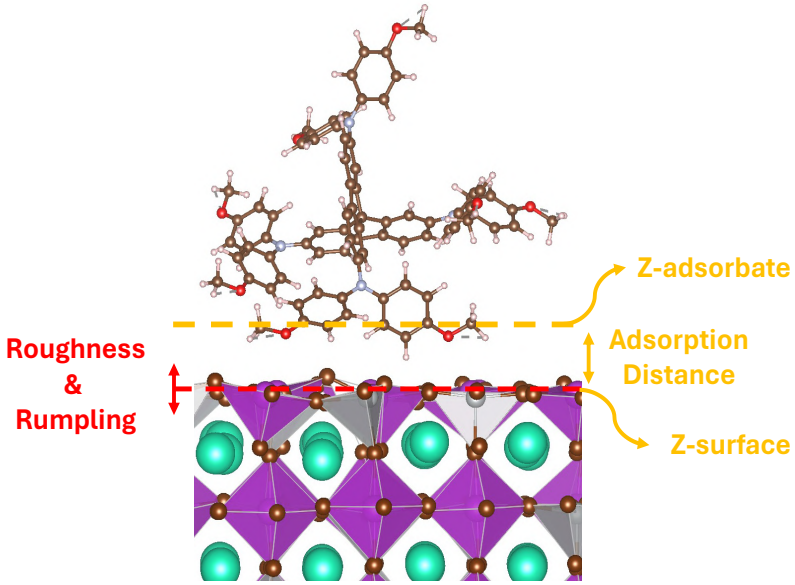


Figure 8: Visual of roughness, rumpling and adsorption distance on the surface of $Cs_2AgBiBr_6$ induced by Spiro-OMetad [37].

Another concept closely related to rumpling is the *surface roughness* $\sigma$, which measures the overall height (in Å) variation of atoms at the outermost layer of the slab after structural relaxation.

$$\sigma = \sqrt{\frac{1}{N}\sum_{i=1}^{N}(z_i - \bar{z})^2} \tag{27}$$

Roughness captures the global deformation of the surface induced by adsorption ie. how "uneven" the surface becomes as a whole. Larger $\sigma$ values correspond to stronger structural perturbation and stronger interfacial coupling.

In short, roughness describes how uneven the surface becomes overall and rumpling describes how much the cation and anion separate. Surface roughness has been utilized in chapter 6, where we investigated how different halide perovskite facets interact with hole transporting materials. An example showcasing this can be seen in the figure 8.

## 3.3 Adsorption Distance

One of the simplest geometric descriptors of adsorption is the *adsorption distance*, which characterizes how far the adsorbate sits above the substrate. This parameter is often correlated with binding energies and electronic structure modifications [111–113]. The adsorption distance $d_{\text{ads}}$ is typically measured as the shortest vertical distance between the adsorbate (or its centroid, or a key atom within the adsorbate) and the average plane of the topmost atoms of the surface as illustrated in figure 8:

$$d_{\text{ads}} = z_{\text{adsorbate}} - z_{\text{surface}}, \tag{28}$$

where $z_{\text{adsorbate}}$ is the vertical coordinate of the chosen adsorbate atom or molecular center, and $z_{\text{surface}}$ is the average coordinate of the topmost substrate atoms. In more complex geometries, adsorption distances may also be defined as the bond length between the adsorbate and the nearest surface atom. Small distances are typically associated with strong interactions, where significant charge transfer or hybridization can occur between adsorbate and substrate orbitals. Larger distances suggest that the interaction is dominated by van der Waals (vdW) forces. For halide perovskite surfaces, adsorption distances help differentiate between strong and weak interaction at the interfaces[111, 114]. In chapter 6 of this thesis, we have discussed in detail adsorption distances of different hole transporting materials on top of numerous facets in hybrid halide perovskites.

## 3.4 Binding Energy

The binding energy (BE) provides a quantitative estimate of adsorption stability and is essential for comparing different adsorbates or adsorption sites. The binding energy (measured in eV) is defined as:

$$E_{\text{bind}} = E_{\text{adsorbate+surface}} - \left(E_{\text{surface}} + E_{\text{adsorbate}}\right), \tag{29}$$

where $E_{\text{adsorbate+surface}}$ is the total energy of the combined system in its relaxed geometry, $E_{\text{surface}}$ is the energy of the clean relaxed surface, and $E_{\text{adsorbate}}$ is the energy of the isolated adsorbate computed in the same supercell. By this convention, negative binding energies correspond to stable and favoured adsorption. Furthermore,the magnitude of the binding energy provides insight into the nature of adsorption. Large negative values correspond to strong adsorption, where adsorbates might form covalent or ionic bonds with the surface. Smaller negative values are characteristic of weak adsorption dominated and 0 or positive binding energies indicate unstable adsorption. In perovskite materials, binding energies are crucial for evaluating the stability of defect passivators [115, 116], interfacial layers [117], and environmental species such as water or oxygen on perovskite surfaces [118]. By combining binding energy with adsorption distance, an in depth understanding of surface-adsorbate interactions can be achieved.

## 3.5 Density of States and Its Decompositions

Intensively used for analyzing the electronic structure [119, 120], the density of states (DOS) quantifies the number of available electronic states per unit energy (eV) and provides insight into the distribution of occupied and unoccupied states across the valence and conduction bands, thereby clarifying how electrons populate the material's electronic structure. It is defined as:

$$D(E) = \sum_{n,\mathrm{k}} \delta(E - \epsilon_{n\mathrm{k}}), \tag{30}$$

where $\epsilon_{n\mathrm{k}}$ are the Kohn-Sham eigenvalues corresponding to band index $n$ and wavevector k [66, 67]. In practice, the Dirac delta function is replaced by a smearing function to obtain a smooth DOS curve [121, 122]. The total DOS( TDOS) reveals the overall band structure features such as the bandgap, the position of the Fermi level, and the relative density of states near the conduction and valence band edges. Beyond the total DOS, it is often useful to resolve the contribution of specific atoms or orbitals to the electronic structure. This resolution of DOS leads to what is called the projected density of states (pDOS), in which the Kohn-Sham wave functions are projected onto a chosen set of localized atomic orbitals $\phi_\alpha$. The pDOS is expressed as:

$$D_\alpha(E) = \sum_{n,\mathrm{k}} |\langle \phi_\alpha | \psi_{n\mathrm{k}} \rangle|^2 \; \delta(E - \epsilon_{n\mathrm{k}}) \,, \tag{31}$$

where $\psi_{n\mathrm{k}}$ are the Kohn-Sham wave functions [67, 119, 121]. The pDOS reveals which atoms contribute to different energy ranges of the electronic structure, thereby allowing identification of the character of the valence and conduction band edges.

For a more detailed analysis, the pDOS can be further decomposed into the orbital (s, p, d, f) decomposed DOS (oDOS). For instance, one can use this to distinguish the relative weights of Pb $6p$ and I $5p$ orbitals at the conduction and valence band edges in lead halide perovskites. This is crucial for understanding the role of chemical bonding and hybridization in determining the electronic properties. In summary, the TDOS provides an overall picture of the electronic structure, the pDOS resolves atom specific contributions, and the oDOS highlights the orbital character of the bands. Together, these form a comprehensive framework for interpreting DFT results and connecting them to physical phenomena such as bandgap formation, charge carrier localization, and optical transitions etc.

## 3.6 Bader Charge analysis

In density functional theory (DFT), the total electronic density $\rho$(r) is readily available, but assigning electron density to individual atoms requires a partitioning

scheme. Bader charge analysis, a theory introduced by R. Bader [123], provides a way to define atomic volumes directly from the topology of the electron density. In this approach, real space is divided into regions bounded by zero flux surfaces of the gradient of the charge density [58, 124, 125],

$$\nabla\rho(\mathrm{r}) \cdot \mathrm{n}(\mathrm{r}) = 0, \tag{32}$$

where n(r) is the normal to the surface. Each of these regions, called a Bader volume, is uniquely assigned to an atom. The total number of electrons associated with an atom is then obtained by integrating the charge density within its Bader volume,

$$Q_\alpha = \int_{\Omega_\alpha} \rho(\mathrm{r})\, d\mathrm{r}. \tag{33}$$

By comparing $Q_\alpha$ with the neutral valence electron count of the atom, one obtains the net charge transfer. For lead halide perovskites solar cells, Bader analysis is particularly useful to quantify the charge transfer at interfaces, providing insights into interfacial electronic coupling [58, 124].

## 3.7 Work Function Calculation

The work function (WF) essentially determines the ease with which electrons can be emitted from a solid. It is defined as the energy required to move an electron from the Fermi level $E_\mathrm{F}$ inside the material to the vacuum level $V_\mathrm{vacuum}$ outside the material [119, 126],

$$\Phi = V_\mathrm{vacuum} - E_\mathrm{F}. \tag{34}$$

Here, $V_\mathrm{vacuum}$ corresponds to the electrostatic potential in the vacuum region [79]. In slab calculations, the vacuum level is determined by calculating the planar-averaged electrostatic potential along the surface normal direction:

$$\bar{V}(z) = \frac{1}{A} \int_A V(x, y, z)\, dx\, dy, \tag{35}$$

where $A$ is the in-plane area of the surface. The potential oscillates within the slab and plateau's outside. This plateau is what defines $V_{\text{vacuum}}$. In perovskite solar cells, for example, the WF of electrodes must be tuned to align with the conduction or valence band edges of the perovskite absorber [30, 127–129].

## 3.8 Charge Density Difference (CDD)

Charge density difference (CDD) analysis can be used for visualizing how electrons redistribute during bonding, adsorption, or defect formation. It provides a picture of charge accumulation and depletion compared to a reference state. The CDD is defined as:

$$\Delta\rho(\mathrm{r}) = \rho_{\text{tot}}(\mathrm{r}) - \sum_i \rho_i(\mathrm{r}), \tag{36}$$

where $\rho_{\text{tot}}(\mathrm{r})$ is the self-consistent charge density of the combined system, and $\rho_i(\mathrm{r})$ are the charge densities of the isolated subsystems (atoms, molecules, or slabs) calculated in the same supercell [121, 123]. Positive values of $\Delta\rho(\mathbf{r})$ indicate charge accumulation, while negative values correspond to charge depletion. By plotting isosurfaces or planar averages of $\Delta\rho(\mathrm{r})$, one can directly identify the regions where electrons are localized, transferred, or polarized [79].

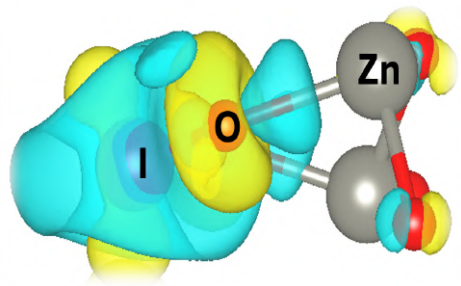


Figure 9: Example of CDD isosurfaces showcasing depletion (in cyan) and accumulation regions (in yellow) on I-O bond formation.

## 3.9 Electrostatic Potential

The electrostatic (Hartree)[130] potential $V(\mathrm{r})$ represents the Coulomb interaction due to the electronic and ionic charge distributions [70]. Analysing the potential one can obtain information complementary to the charge density, especially for surface and interface systems. It is common to calculate the planar-averaged potential along a chosen direction (e.g., the surface normal in slab geometries):

$$\bar{V}(z) = \frac{1}{A} \int_A V(x, y, z)\, dx\, dy. \tag{37}$$

The electrostatic potential helps in determining the vacuum level and consequently the work function. Moreover, by aligning potential profiles of different systems, one can compute band offsets at interfaces and heterojunctions [131, 132].In perovskite materials, analyzing the electrostatic potential is useful for understanding surface dipoles, interface energetics, and the effect of structural distortions on band alignment. Combined with CDD analysis, potential profiles can provide a complete picture of electronic redistribution and energy level alignment in complex device architectures.

## 3.10 Experimental Parameters

Practically, the performance of a solar cell is fundamentally evaluated in terms of its power conversion efficiency (PCE), which is defined as the ratio of the output electrical power to the input optical power under standard illumination conditions [49, 133]. The PCE represents the overall ability of a device to convert incident photons into usable electrical energy. However, this is not an intrinsic material property; rather, it depends on several parameters that govern charge generation, transport, and collection processes within the device. These parameters include the short-circuit current density ($J_{SC}$), the open-circuit voltage ($\mathrm{V_{OC}}$), the fill factor ($FF$), the maximum power point ($MPPT$), and the external quantum efficiency (EQE) [134, 135].

The $J_{SC}$ is determined by the number of photo-generated charge carriers that are successfully collected at the electrodes under short-circuit conditions, and it strongly depends on the optical absorption and carrier transport properties of the absorber layer [133]. The $V_{OC}$, on the other hand, is a measure of the maximum voltage attainable when no external current flows, and it reflects the balance between charge generation and recombination processes in the device [29]. The fill factor (FF) quantifies the squareness of the J-V curve and provides insight into resistive losses and recombination dynamics within the cell [29]. The product $J_{SC} \times V_{OC} \times FF$ yields the maximum extractable electrical power, which, when normalized to the incident power $P_{in}$, defines the PCE as:

$$\eta = \frac{J_{SC} \times V_{OC} \times FF}{P_{in}}. \tag{38}$$

Finally, the quantum efficiency (QE) which can be either internal (IQE) or external (EQE), provides wavelength resolved information on the device's ability to convert absorbed or incident photons into collected charge carriers. This provides insights into the optical and interfacial losses [134, 136]. Collectively, these parameters determine the operational efficiency of perovskite photovoltaic devices, making their optimization essential for achieving high performance solar cells. Indeed, in the last chapter of this thesis, we have evaluated J-V characteristics of several passivated cells.

# 4 Improved Hole Extraction and Band Alignment via Interface Modification in Hole Transport Material-Free Ag/Bi Double Perovskite Solar Cells

When the divalent lead is substituted from the $ABX_3$ perovskite structure by stoichiometric amounts[137] of monovalent silver and trivalent bismuth, the elpasolite (broadly named double perovskite (DP)) $Cs_2AgBiBr_6$ is formed, a material that possesses high environmental stability[138–140] and drastically reduced toxicity, in comparison to LHPs[141]. Like LHPs, this DP features long charge carrier lifetimes[142–144] and can easily be solution-processed [145–147]. Yet, the PCEs of solar cells that are based on pristine $Cs_2AgBiBr_6$ as sole light-harvesting material have not exceeded 2.81%[148] due to a large indirect bandgap,[138, 147, 149] strong electron-phonon coupling,[146, 150, 151] short electron diffusion length,[152, 153] and an unfavorable polaron-hopping transport mechanism and low selectivity of transport layers [154, 155].

One common strategy to tackle the low selectivity and improve the band alignment between perovskite layers and HTM (and electron transport layers (ETLs) in inverted solar cells) is creating a two-dimensional (2D) perovskite interlayer [156–158]. When the dimensionality of a perovskite crystal is reduced from three-dimensional (3D) to 2D, it undergoes quantum confinement that increases its bandgap with decreasing layer thickness [159–161]. In detail, the valence band maximum (VBM) is slightly elevated and the conduction band minimum (CBM) is strongly elevated. When the 2D layer is utilized as an interlayer between the perovskite layer and the HTM, the high CBM level serves as an energy barrier that suppresses the injection of excited electrons from the perovskite layer into the HTM [162, 163]. However, the VBM and CBM elevation of a 2D interlayer can not only improve the band alignment between perovskite and HTM but also allow the removal of the HTM to fabricate HTM-free

perovskite solar cells. In the latter case, the 2D interlayer adopts the HTM's purpose of blocking electron extraction into the back electrode and improving the valence band (VB) alignment toward the back electrode. The schematic band diagrams of a $Cs_2AgBiBr_6$ solar cell with HTM as well as of HTM-free solar cells with and without a 2D perovskite layer are depicted in Figure (10). While the removal of the HTM causes increased recombination at the back electrode in a pure $Cs_2AgBiBr_6$ solar cell (Figure 10 (b)), the presence of a 2D layer (Figure 10 (c)) will improve the selectivity and the band alignment toward the back electrode. Thereby, the 2D modification adopts the function of the HTM.

Herein, we carried out a combined theoretical and experimental investigation of the $Cs_2AgBiBr_6$ (double perovskite (DP))-based solar cells, in which the DP's surface was modified via a n-butylammonium post treatment to create a mixed 2D/3D interface. This modification allowed the replacement of the two expensive components in the cell viz gold,a typical choice for electrode and Spiro-OMeTAD, a frequently used hole transporting material (HTM), with carbon black electrode (CBE) obtained from hazelnut shells. The objective here was not to obtain the most efficient $Cs_2AgBiBr_6$-based PV devices, rather to take a step in the direction of developing less-toxic and low-cost PV device for indoor applications.

In this combined effort, the experiments were carried out by partners at Politecnico di Tornio, while I performed DFT calculations to uncover the atomistic origins of the performance we observed for the 2D/3D interface.

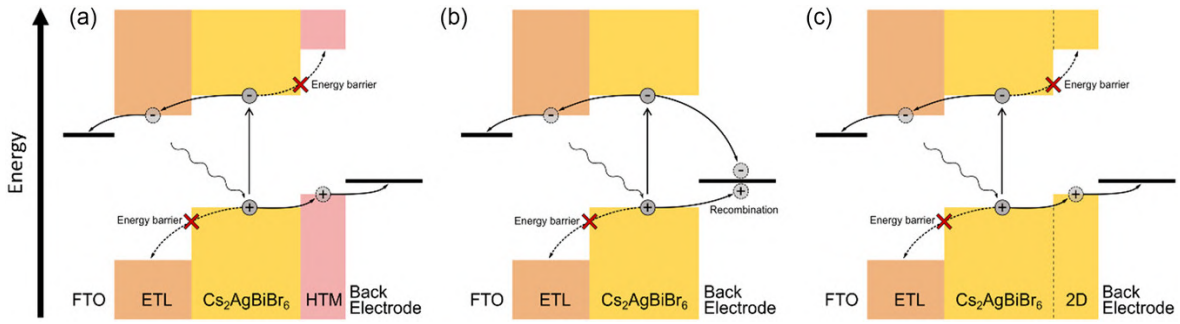


Figure 10: Schematic band diagrams of $Cs_2AgBiBr_6$ solar cell architectures. a) Classical n-i-p architecture in which $Cs_2AgBiBr_6$ is sandwiched between ETL and HTM, e.g., $TiO_2$ and Spiro-OMeTAD, respectively. The HTM creates an energy barrier for electrons and the band alignment favors the hole drift toward the back electrode. b) HTM-free $Cs_2AgBiBr_6$ solar cell. No energy barrier prevents the recombination of electrons and holes at the back electrode. c) 2D/3D surface modified $Cs_2AgBiBr_6$ solar cell. The 2D perovskite functions like an HTM, elevating the VBM slightly and the CBM strongly as will be shown in this chapter.

## 4.1 Experimental outcomes

The 2D/3D mixed perovskites films were developed using BABr (as described in the Film Preparation at the end) in three concentrations viz. 0.01, 0.05, and 0.1 M respectively. J-V measurements (see figure 11 ) under AM 1.5G demonstrate that after 2D modification of $Cs_2AgBiBr_6$ with 0.01 M BABr, the open circuit voltage ($V_{oc}$) and fill factor (FF) remain comparable to the reference case or unmodified DP, while the short circuit current ($J_{sc}$) increases, yielding a 7% higher average efficiency. At 0.05 M, $J_{sc}$ , $V_{oc}$, and FF all improve relative to both reference and 0.01 M, leading to 38% and 58% (record) PCE increases and a record $V_{oc}$ of 1.25 V. Such gains were attributed to the reduced interfacial recombination due to improved band alignment of the 2D/3D perovskite (see sketched alignments in figure 11 (c)) film with the CBE. However, beyond 0.05 M, though a thicker 2D layering further improves $V_{oc}$, it also

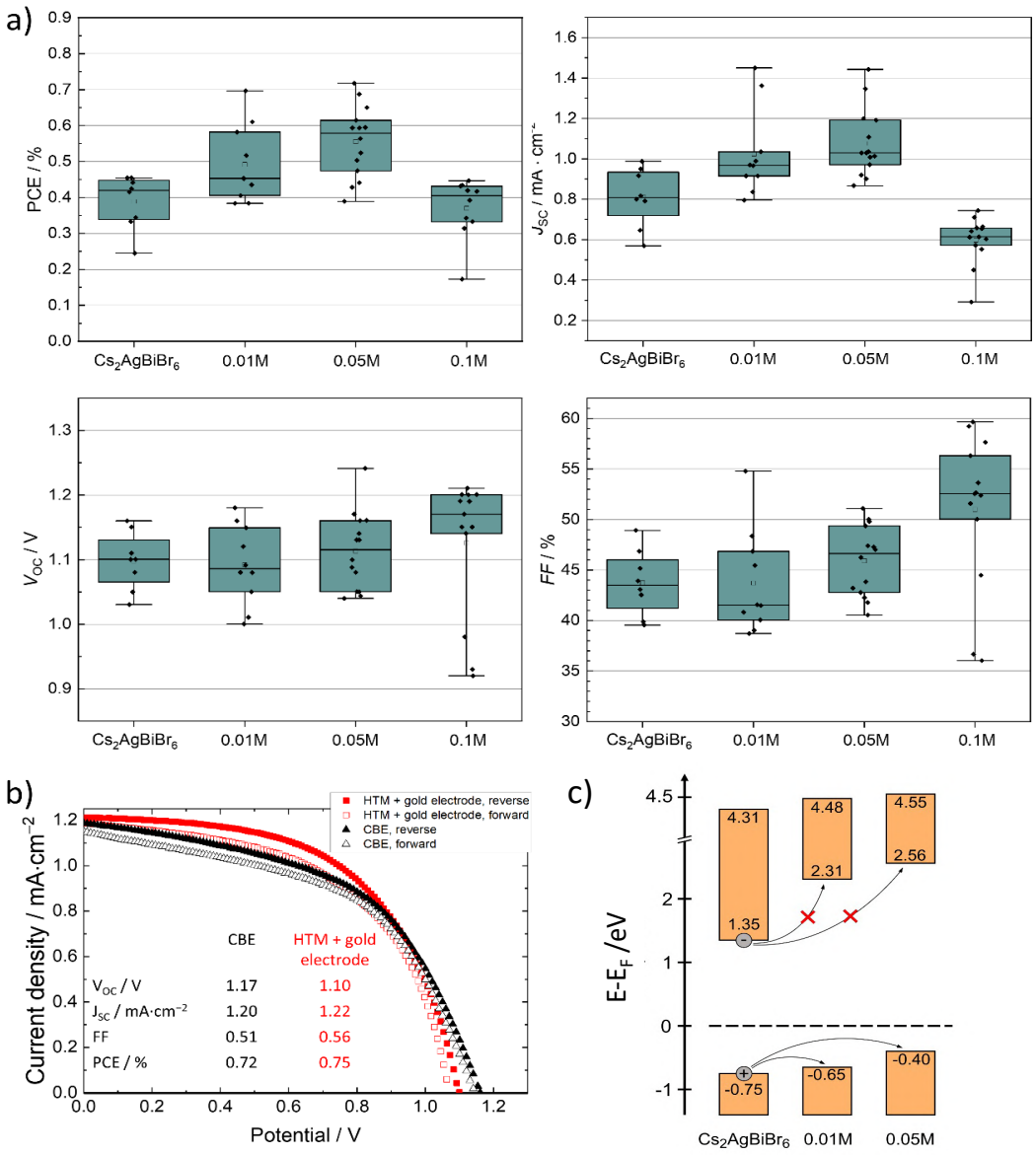


Figure 11: 2D/3D modified $Cs_2AgBiBr_6$ solar cells characterization;(a) Statistics on relevant figures of merits for HTM-free solar cells containing a CBE top-electrode;(b) Best J-V curves for 0.05 M modified devices containing either a CBE top-electrode or Spiro-OMeTAD HTM and gold electrode;(c) Sketched band alignment between $Cs_2AgBiBr_6$, and 0.01 M, or 0.05 M, respectively.

introduces insulating organic interlayers thus suppressing $J_{sc}$ and preventing further PCE improvement.

To uncover the microscopic origins of the experimental results, we performed DFT calculations consisting of 3D/2D heterostructures made of 8 symmetric layers of 3D $Cs_2AgBiBr_6$ cubic DP slab and a 2D $(BA)_2CsAgBiBr_7$ capping layer with growing number of layers (Figure 12 - see Table 19 for detailed structural information). In particular, we considered four hetero-structures containing 1, 2, 3, and 5 2D layers, dubbed hs1, hs2, hs3, and hs5, respectively.

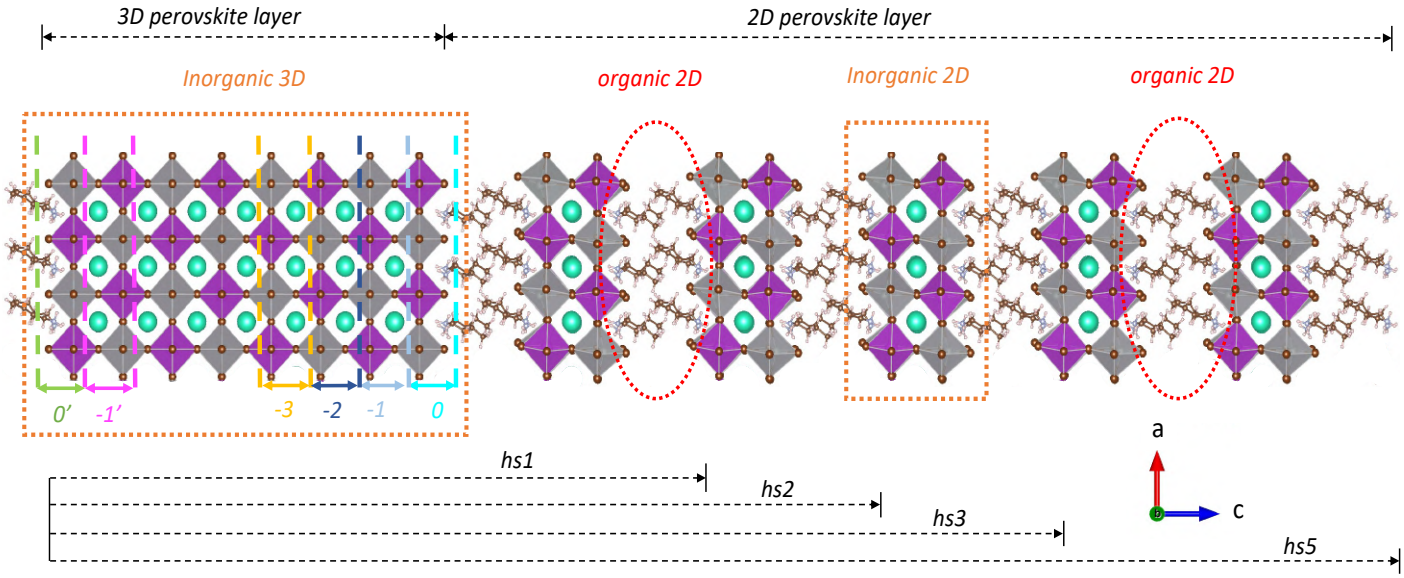


Figure 12: Slab models considered for DFT calculations. Divisions of 3D perovskite layer used to calculate npDOS for respective slabs. Periodic boundary conditions (PBC) applied along the direction perpendicular to the surface result in the creation of two equivalent 3D/2D interfaces.

## 4.2 Theoretical outcomes

### Density of states analysis

Figure 13 presents the density of states (DOS) projected (pDOS) on the 3D, and organic

and inorganic sublattices of 2D domains of the hs1,hs2 and hs3 heterostructures. It is evident that for all the three structures, the VBM and close-by energy states are related to the 3D and the inorganic sublattice of the 2D DPs, which are in agreement with other studies [138, 145, 164, 165]. To identify the microscopic origin of the enhanced charge extraction with BABr concentration up to 0.05 M, we computed the contribution of the various layers of Figure 12 of the 3D slab to the density of states (see Figure 14). This contribution, expressed in percentage and denominated normalized pDOS (npDOS), is obtained by dividing pDOS relative to one 3D layer by (total) DOS and multiplying by 100. npDOS is set to zero in the region of the bandgap.

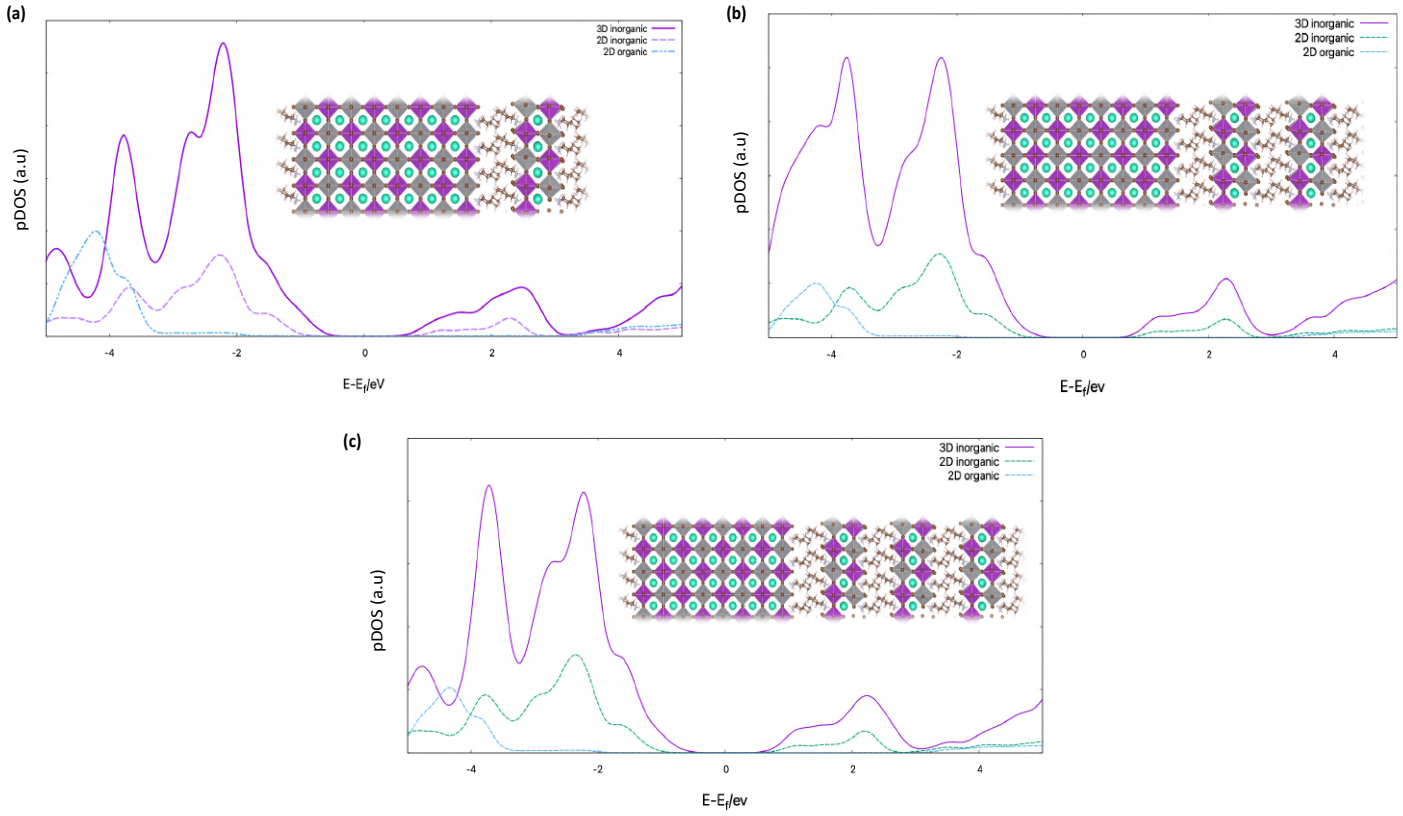


Figure 13: (a-c)pDOS calculated for 3D/2D hs1, hs2 and h3 heterostructures. The inset shows the cartoon of the heterojunctions fro each of the respective cases.

One sees that for the single 2D bilayer (hs1), the contribution of the interface 3D

layer (0) to the DOS at VBM and closer energies is the lowest among all the layers of the $(BA)_2CsAgBiBr_7$ computational slab, with the largest contribution arising from the bulk-like layers ($-3$). This implies that for the hs1 sample, one has little probability of finding holes at the 3D/2D interface and their extraction is inefficient. The picture changes with the increase of the thickness of the 2D slab, with the contribution of the interface layer to the VBM growing steadily from 3 to, 10, to 16, to 26% for hs1, hs2, hs3, and hs5, respectively. A similar effect of a thicker 2D layer is observed up to 0.7 eV below the VBM. This increase in the contribution of the interface layer to VBM means that thermalized holes are closer to the interface, which makes their extraction easier as revealed in the experiments (refer [37] for detailed experimental outcomes).

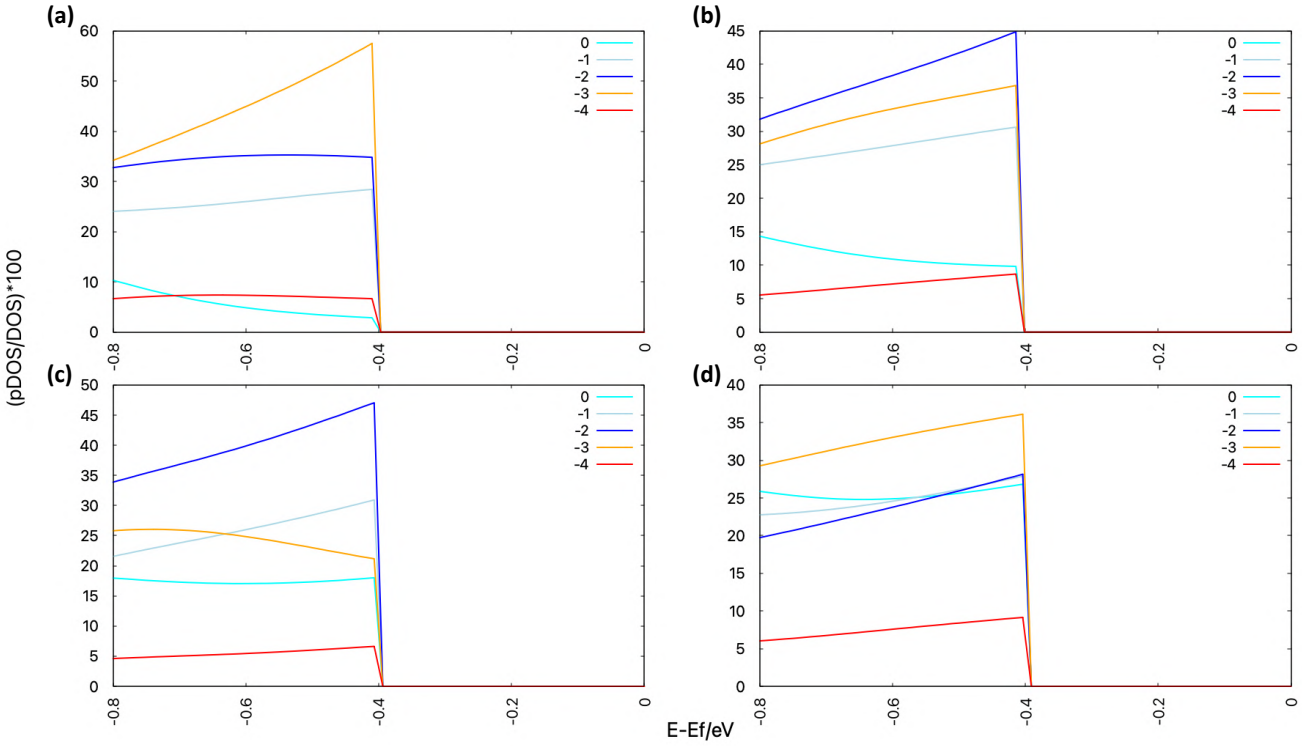


Figure 14: (a–d) Contribution of npDOS of each sublayer to the VBM for hs1, hs2, hs3 and hs5 respectively.

However, in experiments, a maximum bandgap for the 0.05 M solar cells was

observed (refer to [37] for details). This is attributed to two additional effects of the thickness of the 2D capping layer. First, the resistance of the 2D capping layer increases with its thickness, thus balancing the beneficial effect of the heterostructure in attracting holes at the interface. Moreover, 2D capping layer also increases the contribution of the interface 3D layer in the CBM (Figure 15), i.e., attracting electrons in the CB toward a region with higher concentration of holes. Thus, a longer residence time of holes at the interface due to the longer extraction time of the thicker 2D layer favors their recombination with electrons also present in this region. This leads to a reduction of the current density and, henceforth, PCE.

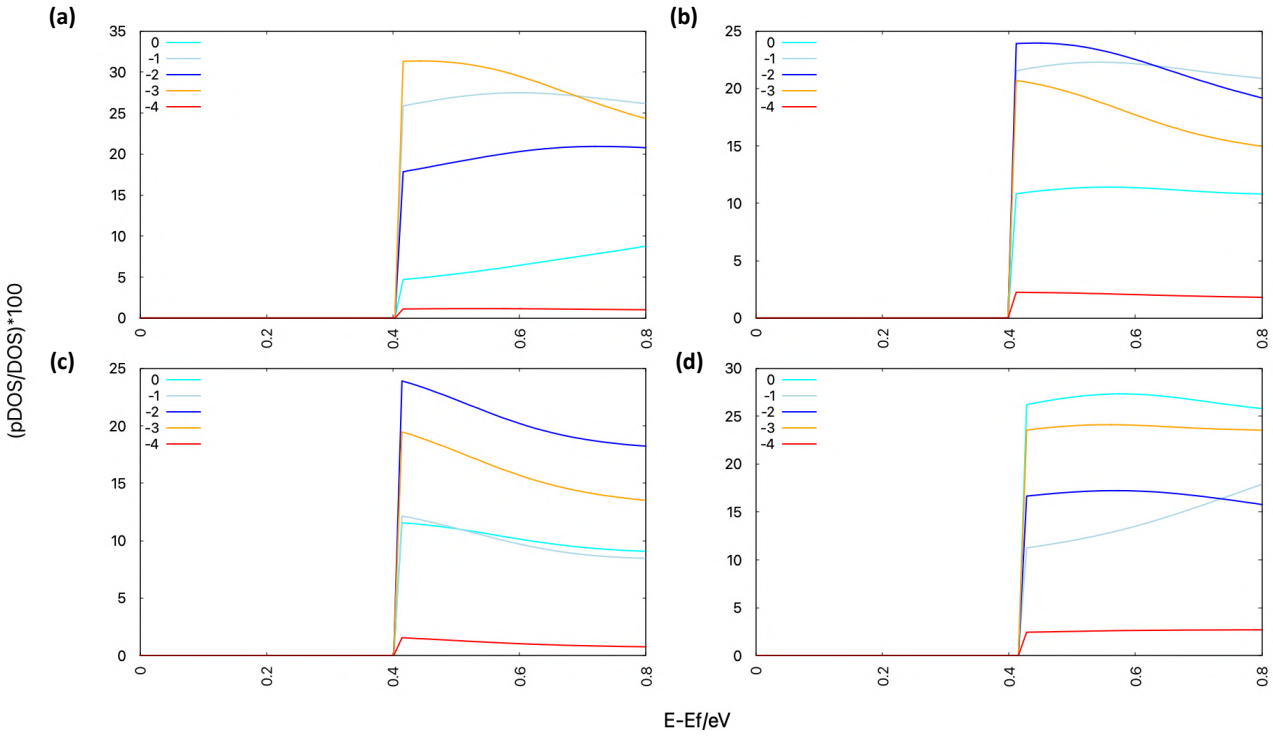


Figure 15: (a–d) Contribution of npDOS of each sublayer to the CBM for hs1, hs2, hs3 and hs5 respectively.

Next, we wanted to understand the effectiveness of the 2D layer in passivating defects. To do this, we considered the three most likely defects in bulk $Cs_2AgBiBr_6$ [166–168]: bismuth antisite and bismuth and bromide vacancies, denoted as $Ag''_{Bi}$, $V'''_{Bi}$, and

$V^{\bullet}_{Br}$, following the Kröger-Vink notation.

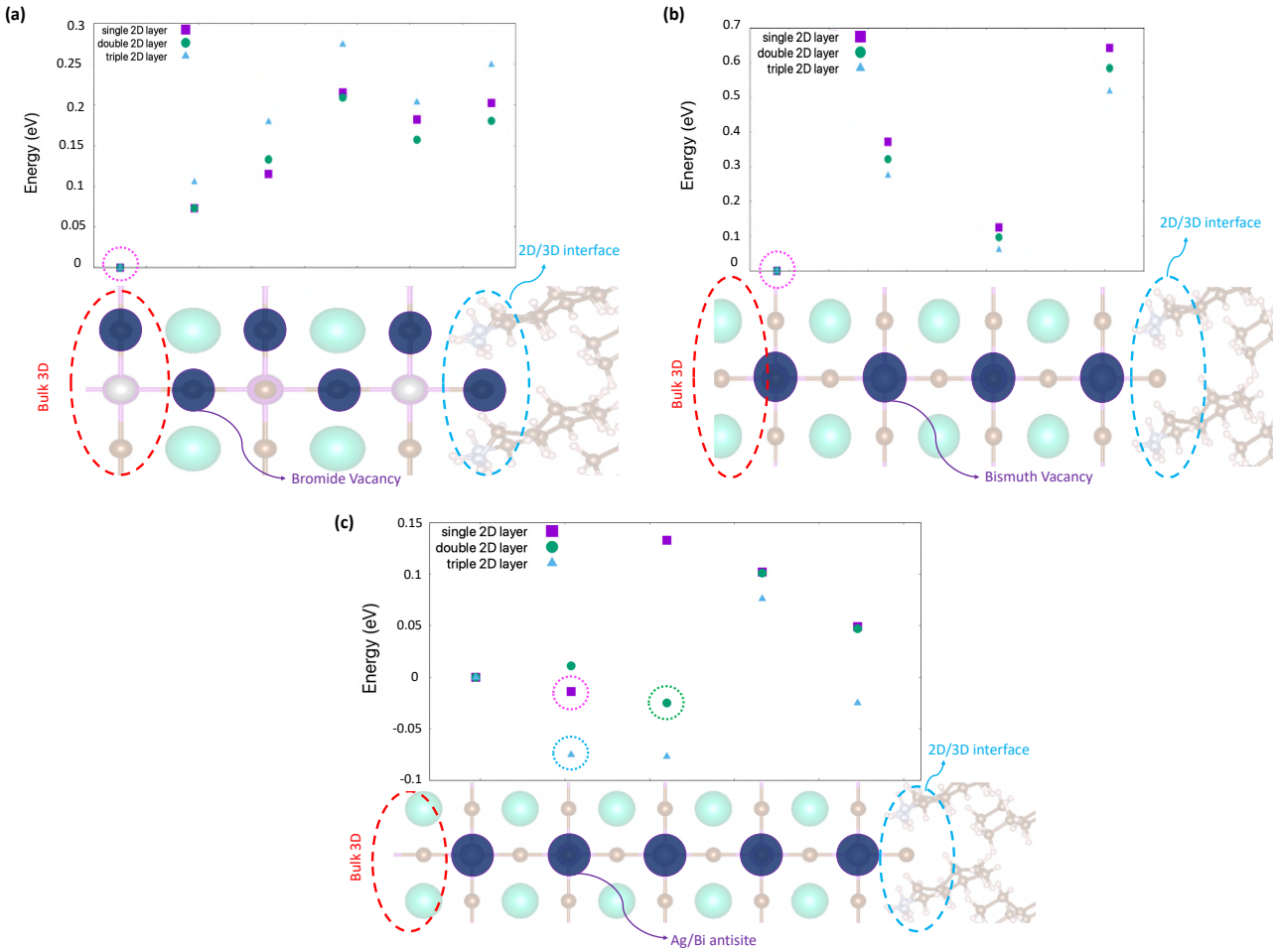


Figure 16: Energy versus position of a) bromide vacancy ($V^{\bullet}_{Br}$), b) bismuth vacancy ($V^{'''}_{Bi}$), and c) antisite ($Ag^{''}_{Bi}$) of hs1, hs2, and hs3. Dashed circles around symbols denote the state corresponding to the minimum energy defect position. Energies are arbitrarily shifted so that the value in the bulk position is zero. In each panel is reported a cartoon illustrating the portion of the computational sample illustrating the position of the corresponding defect.

We computed the relative energy of these defects as a function of their position along the slab (Figure 16) for the 2D capping at various thicknesses. First and foremost, we notice that all defects (encircled in pink) are more stable when moved away

from the interface layer. In other words, the effect of 2D capping is to prevent any accumulation of defects at the $Cs_2AgBiBr_6$ surface, where, as shown before, we observe an accumulation of holes and electrons, and defects can promote recombination. Our simulations suggest that the passivation effect of 2D capping is not passivation in the conventional sense: rather, the presence of 2D layers prevents the accumulation of defects at the 3D surface or interface. Regarding defect passivation, the thickness of the slab does not play a major role, since we observe similar defect energies as a function of position within the 3D slab for all heterostructures, regardless of the thickness of the 2D layer. Furthermore, we performed analogous calculations for a 3D/Spiro-OMeTAD interface model. We also computed the relative energetics of $V_{Br}^{\bullet}$ and $Ag_{Bi}^{''}$ defects as functions of position. In contrast to the 3D/2D system, we found that, with Spiro-OMeTAD, both defects are attracted toward the interface layer (see Figure 17). Even in the absence of any defect at the perovskite interface, a visual inspection of the minimum energy configuration reveals a more pronounced and extended lattice distortion in the perovskite region adjacent to the Spiro-OMeTAD interface compared to the 2D/3D sample (compare Figure 18(c,d) and Figure 18(e)). It is well known that tilting of $[AgBr_6]^{5-}$ and $[BiBr_6]^{3-}$ octahedra in double perovskites affects their electronic structure and, consequently, their electronic properties [139]. Indeed, the projected density of states (pDOS) of the interface layer in the defect-free 3D/Spiro-OMeTAD system (Figure 18 (a)) shows orbitals extending deeper into the bandgap relative to the 2D/3D case.

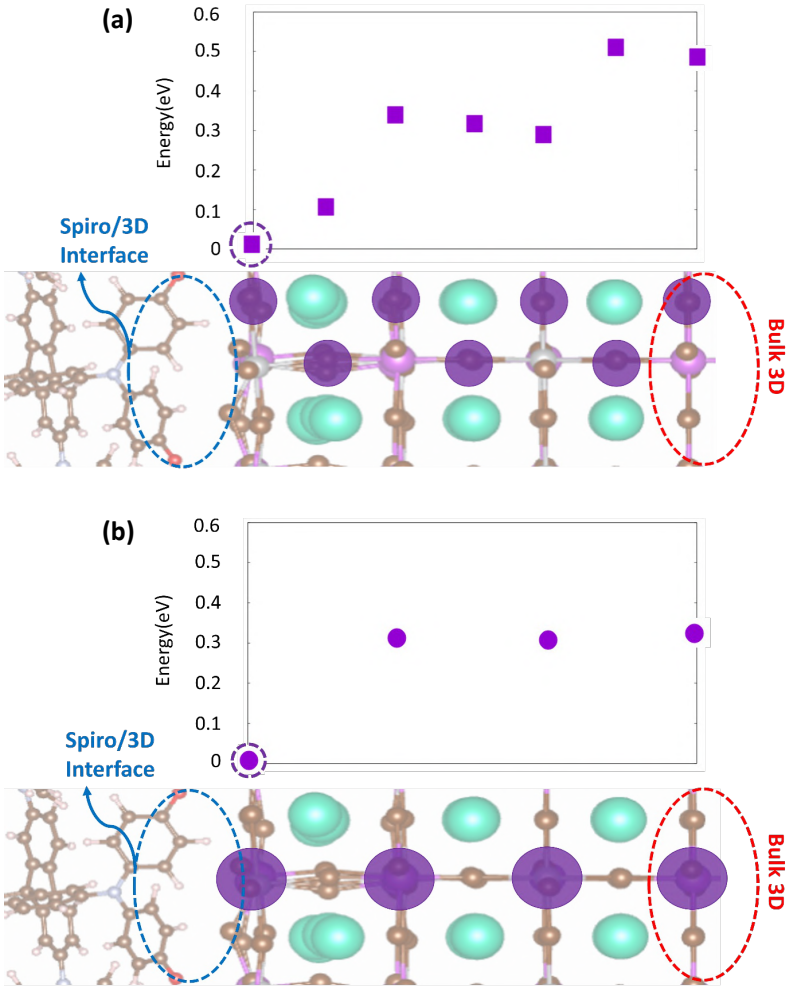


Figure 17: a) Defects energy vs position of a) bromide vacancy ($V^{\bullet}_{Br}$) ; b) Antisite ($Ag''_{Bi}$)in the case of 3D/Spiro interface system. Dashed circles indicate the lowest-energy defect configurations. Energies are referenced to the surface position (set to zero). Each panel also includes a schematic of the 3D/2D model highlighting the defect location.

These states can either result in trap-assisted recombination or simply slow down carrier dynamics. This effect is enhanced when $V^{\bullet}_{Br}$ and $Ag''_{Bi}$ defects are accumulated at the 3D/Spiro-OMeTAD interface, according to the driving force discussed above. This is illustrated by comparing the pDOS of the interface layer of the pristine and

defected 3D/Spiro-OMeTAD system (Figure 18 (b)), which shows additional states due to the defects appearing at the bottom of the CB for both types of defects.

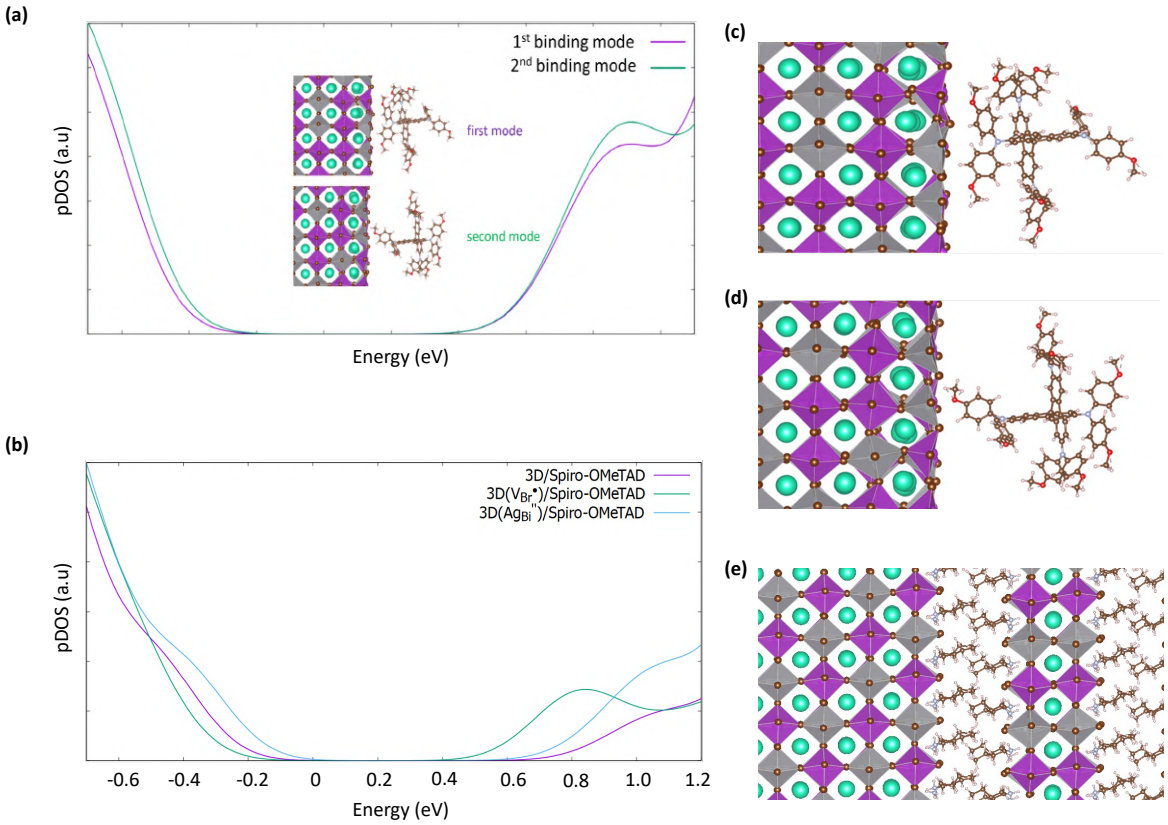


Figure 18: (a) pDOS of the 3D/Spiro-OMeTAD for the two binding modes;(b) pDOS calculated for Spiro-OMeTAD/3D interface for pristine and defected systems respectively.(c-d) 3D/Spiro-OMeTAD samples. The panel (c) and (d) show the binding modes 1 and 2, respectively;(e) 3D/2D interface.

## 4.3 Conclusion

This chapter presented the performance of a low-cost, HTM-free 2D/3D-modified double perovskite (DP) solar cell via treatment of $Cs_2AgBiBr_6$ thin films with *n*-butylammonium bromide (BABr) solution in isopropanol, followed by the deposition of electrodes consisting of carbon black derived from up-cycled biowaste. The presence of

the 2D/3D modification, improved valence band (VB) alignment between $Cs_2AgBiBr_6$ while significantly raising the conduction band minimum (CBM). This led to enhanced selectivity and improved the $J_{sc}$, $V_{oc}$, fill factor (FF), and power conversion efficiency (PCE) for HTM-free 2D/3D $Cs_2AgBiBr_6$ solar cells treated with 0.05 M BABr solution. Density functional theory (DFT) calculations, simulating various numbers of $(BA)_2CsAgBiBr_7$ bilayers capping 3D $Cs_2AgBiBr_6$, revealed that the presence of the 2D perovskite increases the density of states (DOS) for holes at the 2D/3D interface, thereby enhancing hole extraction probability. Moreover, we established that the 2D layers prevent defects from accumulating at the interface, as opposed to Spiro-OMetad. This work demonstrated that applying a 2D/3D modification enhances the PCE of HTM-free $Cs_2AgBiBr_6$ solar cells. The absence of an HTM and the substitution of the metal electrode not only significantly reduces device cost, but the use of a carbon electrode derived from up-cycled biowaste also represents a step toward "green" photovoltaics. Moreover, the drawbacks of low selectivity and weak band alignment commonly associated with HTM-free PVs are mitigated by the formation of a 2D/3D mixed perovskite phase. Although the solar cells presented here possess relatively low PCEs, a well-known limitation of this material [164, 169–172], there are promising reports of highly improved $Cs_2AgBiBr_6$ (e.g., via hydrogenation) that could further benefit from the approach demonstrated in this work [158] to boost such technology.

## 4.4 Film Preparation

The preparation of $Cs_2AgBiBr_6$ thin films as well as their 2D modification were entirely performed in an argon-filled glovebox. First, $Cs_2AgBiBr_6$ powder, synthesized as described in previous work [137], was dissolved in dimethyl sulfoxide (DMSO, $99.7 + \%$, Thermo Scientific) to create a 0.5 $\mathrm{mol\,L^{-1}}$ precursor solution. The solution was stirred until the powder was fully dissolved. To deposit the $(BA)_2CsAgBiBr_7$ thin film, a substrate was mounted onto a spin coater, the precursor solution (50 $\mu$L) was

evenly spread across the substrate, and the substrate was rotated at 4000 rpm for 40 s (3 s acceleration time). Immediately after the spin-coating process, the substrate was transferred to a preheated hot plate at 285 °C and annealed for 5 min. To prepare the 2D modification, we adapted the synthesis route from [164]. The room-temperature thin films were again mounted onto a spin coater, then an *n*-butylammonium bromide (BABr, Aldrich) solution (100 $\mu$L; 0.01, 0.05, or 0.1 mol $L^{-1}$ in isopropanol) was evenly spread across the thin films, and they were rotated at 4000 rpm for 40 s. Afterward, the thin films were left to dry in the glovebox overnight. Following film preparation, the hole transport material (HTM) and respective electrodes were deposited according to the protocol described in ([37]).

## 4.5 Computational setup and calculations

Three computational samples were considered; sample 1) an eight-layer thick slab of $Cs_2AgBiBr_6$ oriented along the (001) crystallographic direction was prepared, and its geometry was optimized. On this, we deposited slabs of $(BA)_2CsAgBiBr_7$ with various layers of the material. Simulations are performed within PBC and the 3D and 2D slabs are combined so that the two 3D/2D interfaces are symmetric and there is no induced dipole moment (see Figure 18 c); slabs 2 and 3) the thickness and the orientation of the $Cs_2AgBiBr_6$ slab along (001) direction were retained, however, the width was doubled along the (100) and (010) directions and its geometry was optimized. On this slab, we deposited the Spiro-OMeTAD molecule. While the $Cs_2AgBiBr_6$ slab is of the same dimensions for samples 2 and 3, the orientation of the HTM molecule differs. This approach is considered as no experimental data are available on the binding characteristics of Spiro-OMeTAD to DP surface. We refer to these different orientations as the different binding modes (18 (a-b)). Furthermore, one can have different surface/interface terminations in a crystallite in experimental samples. On the contrary, all our samples are symmetrically terminated. This is because computational samples

are much smaller than experimental ones (few nanometers vs hundreds of nanometers to micrometers) and systematic asymmetries associated with different terminations likely, possibly introducing a dipole moment in the slab, may induce large electric fields. This likely induces artifacts in the computational results. Density functional calculations were performed within the Perdew-Burke-Ernzerhof generalized gradient approximation [173]. Simulations were performed with the VASP code. Kohn-Sham orbitals were expanded on a plane wave basis set with an energy cutoff of 400 eV. The interaction between valence electron and nuclei plus core electron was described within the projector augmented-wave formalism.[174] For the computational sample 1, the Brillouin zone has been sampled with $4 \times 4 \times 1$ K-points, [78] the latter figure referring to the (001) direction. For the other two computational samples, because of their larger size in the surface plane necessary to accommodate Spiro-OMeTAD, we used $\Gamma$ - point sampling only (as discussed in the theoretical formalism section). The suitability of this setup was validated by checking the convergence of total energy, bandgap, and atomic forces with respect to the parameters listed above.

| Lattice constant (Ang) | hs1 | hs2 | hs3 | hs4 |
|---|---|---|---|---|
| a | 11.271 | 11.271 | 11.271 | 11.271 |
| b | 11.271 | 11.271 | 11.271 | 11.271 |
| c | 73.390 | 93.358 | 113.326 | 153.262 |

Figure 19: Geometry optimized lattice parameters.

# 5 Photoelectron extraction in BiOI:an atomistic perspective

In the previous investigation, we presented our outcomes regarding $Cs_2AgBiBr_6$, which is one of the many materials that showed potential as an absorber for indoor applications. Recently, other Bi based alternative like bismuth oxyiodide (BiOI), has also gained popularity due to its i) band gap of around 2 eV, which is ideal for indoor lighting, and; ii) high visible-light absorption coefficient of $10^4 cm^{-1}$[61]. Moreover, in BiOI carriers also remain delocalized large polarons over their lifetimes displaying band like transport [175, 176]. This is at odds with respect to the hypothesized self-trapping observed in other two-dimensional materials. Despite such characteristics [177, 178], it has shown only a limited efficiency of around 4-4.5 % under white LED. Intrinsic factors such as strong coupling between charge carriers and longitudinal optical (LO) phonons, leading to elevated Urbach energies and promoting non-radiative recombination, have been hypothesized to limit the efficiency of BiOI based solar cells [42, 179]. Apart from the intrinsic ones, the extrincisc factors also play a huge role in affecting a device's performance.

For instance, different crystal facets in BiOI can expose varying atomic terminations, leading to facet dependent electronic and transport (across the interface) properties. DFT calculations have predicted that among various BiOI (slab) facets, [001] offered the lowest electron-hole recombination rate due to effective charge separation [180]. This is attributed to an intrinsic field generated between the well separated $[Bi_2O_2]^{+2}$ and $I^-$ layers. A direct consequence of this is the improvement in the open circuit voltage $V_{oc}$ [181], that eventually leads to an increase of efficiency in devices based on [001] oriented BiOI films [182]. Indeed, experiments demonstrated that [001] oriented films with ZnO as ETL, exhibited a higher compared to the [110] counterparts. However, [001] oriented films posed a limitation on the $J_{sc}$, since the electrodes are not connected with high mobility planes like [110] or [102]. This is detrimental for

solar cell applications [62, 183, 184]. Therefore, it is evident that charge separation and extraction are sensitive to the facet exposed to electron transporting layer (ETL). Hence, optimizing the facets and their termination is key to enhance BiOI's efficiency as a solar photovoltaic cells.

Lastly, the choice of charge transport layers (focusing on the ETL), is another crucial parameter affecting efficiency, since extraction of the carrier depends on it. Typical choice of ETL's includes metal oxides, very often titanium oxide ($TiO_2$). However, it possesses low electron mobility ($\mu = 0.5 - 8cm^2V^{-1}s^{-1}$) and requires a high annealing temperature (500°C) [185]. This presents a strong drawback for BiOI, which begins to degrade beyond (350°C). Compared to $TiO_2$, materials such as zinc oxide ZnO has a low annealing temperature ($100 - 300$°C) and higher electron mobility mobility ($\mu = 5 - 30\text{cm}^2\text{V}^{-1}\text{s}^{-1}$), making it a better choice for BiOI's [186, 187].

Regardless of having identified an optimal ETL and facet, the transport of photoelectrons across the BiOI/ZnO heterostructure is delicate. This essentially means that transport is a strongly dependent on the detailed characteristics of the interface, the chemical binding between atoms of the two structures, polarization [33, 188]. In-fact, it has been hypothesized that control of BiOI surface chemical state when depositing the electron transport layer and increasing charge carrier collection (by increasing work function of the HTL) are key steps that can improve efficiency [62]. However, these conclusions were drawn based solely on experimental empirical characterization and provides no microscopic or detailed mechanism analysis that can suggest optimization strategies.

Therefore, in this chapter we present for the first time, atomistic insights into the electronic and the structural properties of the BiOI and ZnO interface. Our results suggest that the photoelectrons generated in the bulk BiOI are likely to become trapped at the BiOI/ZnO interface, due to the presence of an interfacial energy minimum, that originates from the the disruption of I-Bi and the subsequent formation of I-O (of ZnO) at the BiOI/ZnO interface. This can hinder electron extraction and

promote non radiative recombination, ultimately limiting device performance [189].

## 5.1 Atomistic Structure of the BiOI/ZnO interface

In figure 20 (a) we show the "sandwich" structure of the ZnO/BiOI/ZnO interface system. Here, we consider a (110) slab of BiOI and two (010) slabs of ZnO. The two surfaces of the slab are symmetrically O-terminated, preventing the presence of a dipole moment, which on the small scale affordable in DFT calculations may introduce artifacts. Slabs orientations were chosen because i) they are compatible with the flake-like structure of BiOI crystallites observed in experiments [62, 190, 191] and ii) they to maximize the atomistic matching between the subdomains, hence corresponding to the most likely structure of the buried interface. The optimal matching is obtained by a suitable rotation of ZnO around the [010] axis (see figure 20 (b)). In this configuration, the system is affected by a limited $\sim 1\%$ "theoretical strain" (see equation 39). Thanks to its layered structure, compressive or tensile stress has a limited effect on the electronic structure of BiOI. In particular, the literature data shows that strain values of $\sim 1\%$, like the one present in our computational sample, results in a negligible change in the band gap of the absorber [192]. Likely, this limited strain is at the basis of the (relatively) good PV characteristics of this system observed in the experiments.

The structure of the BiOI/ZnO system presents some major changes in the local coordination with respect to the bulk case due to the change of local chemical environment at the interface. Each terminal iodine atom of the BiOI layer bonds with two oxygen atoms from the adjacent ZnO layer, with a bond length of 1.9Å (Figure 20b). This extra bonding of iodine, absent in bulk BiOI, results in a weakening of Bi-I bonds, with a bond length increasing from $\sim 3.3$Å in the bulk to $\sim 3.6$Å at the interface. A $\sim 3.6$Å Bi-I bond length is at the upper extreme of the length distribution of this bond and it is typical of $\mu$-I bridging [193] or secondary bonding interactions/extended coordination [194]. In turn, the weakening of the Bi-I bond enables the bonding between

bismuth and oxygen of the ZnO layer, characterized by a bond length of $\sim 2.46$Å, slightly longer than the Bi-O distance in bulk Bi-O ($\sim 2.35$Å). At the same time, the distance between these oxygen atoms and zinc interface atoms is $\sim 2.03$Å, very close to the corresponding bond length in the bulk ($\sim 1.98$Å). These Bi-O-Zn "bridge" bonds are responsible for the binding between the light harvesting and the electron transport layers.

To better understand the nature of these interactions, we analyzed 2D maps of electron localization function (ELF). ELF is a dimensionless quantity that ranges from 0 to 1. The value of ELF between pairs of atoms provides insights into the nature of chemical bonds between atoms. For light elements - like C, O, H etc. ELF values in the domain between atoms in the range $\sim 0.8$-1 are a signature of covalent bonding, moderate values $\sim 0.6$-0.8 are indicative of polar covalent interaction and low to moderate values $\sim$ 0-0.6 implicate empty spaces and predominantly no bonding or ionic interaction. For bonds involving heavier atoms - like Bi, I and Zn forming our system- lower ELF maxima ($\sim 0.6$ ) are often observed and are considered to be representative of covalent character [195]. Figure 20 (c-g) reports 2D maps of ELF along relevant planes of the systems complementing our atomic level structural analysis. Consistent with prior reports, bulk Bi-O bonds are characterized by high (for bonds involving heavier atoms) ELF maxima, $\sim 0.5$, revealing covalent of slightly polarized bonds. The Bi-I bond is possibly more ionic, with ELF maxima $\sim 0.47$ and Zn-O is even more ionic, with ELF values $\sim 0.3$ [195–199]. At the interface, Bi-I ELF drops to near 0, signaling bond weakening, while the I-O bond exhibits an ELF of $\sim 0.4$ , consistent with formation of a strong, polarized covalent-like bond [200]. ELF values for Zn-O and Bi-O at the interface of the heterostructure are $\sim 0.25$ and $\sim 0.5$ respectively, revealing a mixed ionic and covalent character.

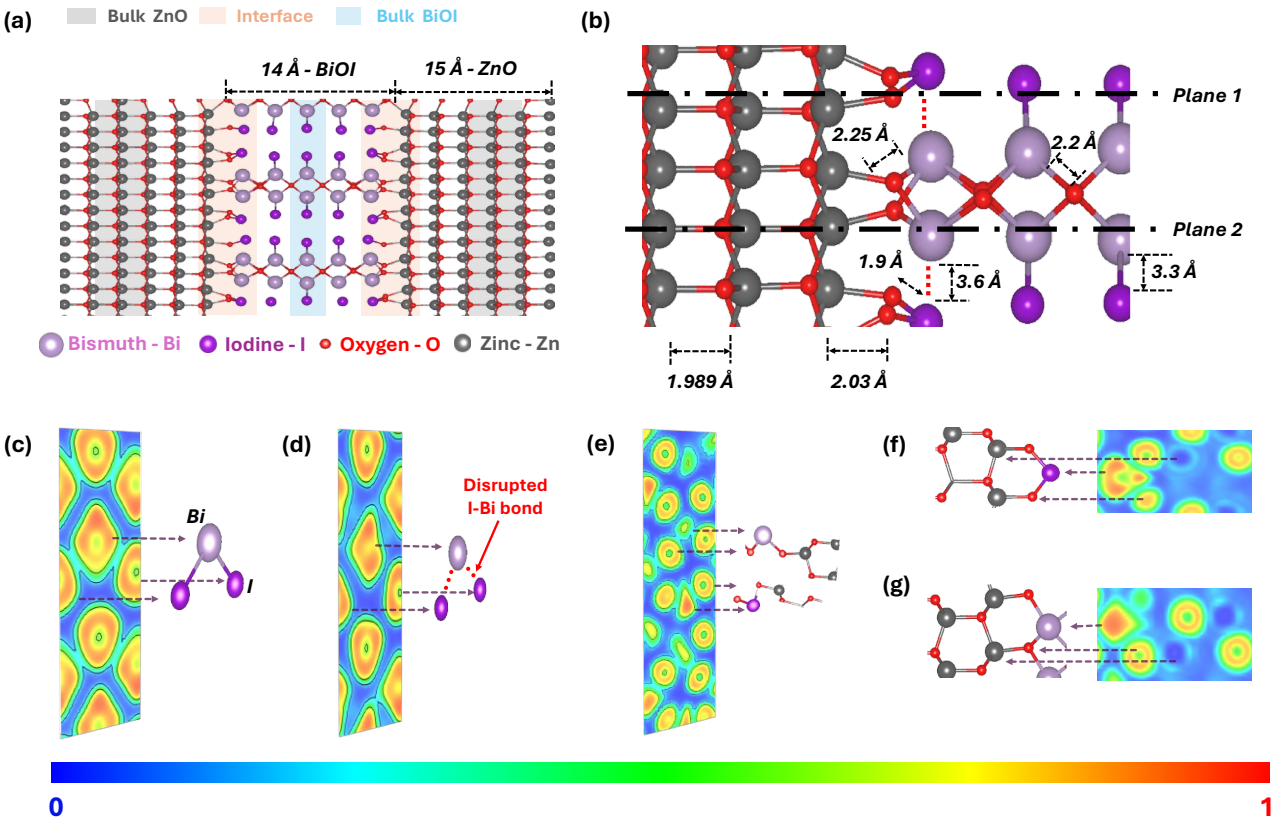


Figure 20: Heterostructure used for calculations; (a) Highlights the components and length of the lattice of the (110) BiOI and (010) ZnO structures, (b) Displays the interatomic distances, in the bulk and the interface,(c-d) ELF variation of the Bi-I bond from bulk to interface,(e) Highlights ELF distribution(green colour) between the Bi-O and the I-O bonds at the interface,(f-g) Top view (mirror images) of the Planes 1 (I-O-Zn binding) and 2(Bi-O-Zn binding) respectively. Notably, neither in the bulk nor at the interface does the Zn-O bond shows electron localization. This is evidenced by the colour contours dominant around atoms (orange/yellow are oxygen atoms) rather than between them and is indicative of an ionic bonding character.

Summarizing, both the structural and ELF analysis support the formation of a strong Bi-O and Zn-O bonding at the BiOI/ZnO interface, allowing a stable interface between the two materials. At the same time, a strong I-O bond is also formed,

accompanied by a sizable weakening of the Bi-I bond, which, as we shall discuss in the following, leads to the formation of defect states at the interface determining the electronic properties of the BiOI/ZnO heterostructure and its transport characteristics.

## 5.2 Projected Density of States (pDOS)

To gain insight into the microscopic origin of the charge transfer mechanism and the electronic properties near and at the interface, we now turn to an analysis of the DOS. We focus on the projected DOS (pDOS), measuring the contribution of specific (sets of) atoms to the total counterpart. Figure 21 compares pDOSes of the bulk domains of the ZnO and BiOI slabs against the corresponding data at the interface between the two materials. Firstly, bulk pDOSes of BiOI and ZnO slabs show a band alignment in qualitative agreement with experimental results. In particular, the VBM and CBM of BiOI lays $\sim 0.45$ eV and $\sim 0.6$ eV above and below the corresponding levels of ZnO, respectively, to be compared with 1.2 and 0.4 eV experimental bands offsets [62, 191]. Notice that, in our calculation as in the experiments, the CBM of ZnO is higher in energy of the corresponding orbital of BiOI. This is at odds with the usual energy alignment between light harvesting materials and ETM. In the literature, the fact that ZnO is able to extract photoelectrons from BiOI is attributed to the presence of high density of sub-band gap states, that electrons can use to tunnel across the interface[191]. Thus, though the quantitative mismatch, we consistently with experiments predict a type I heterojunction between BiOI and ZnO. The structural changes at the interface discussed above significantly affect the local electronic structure. In particular, pDOSes reveal significant changes in the electronic structure of ZnO at the interface with BiOI. While we observed only a minor shift in BiOI pDOS $\sim 0.24$ eV, pDOS of ZnO $\sim 0.67$ eV shows a major shift to higher energies. This is likely due to hybridization between BiOI and ZnO at the interface, as evidenced by their respective orbital contribution near the VBM in Figure 21b. Furthermore, the interface also in-

troduces states near the conduction band minimum (CBM), $\sim 1$ eV below the CBM; in this case, one observes sizable contributions to the pDOS from both ZnO and BiOI. This corresponds to significant hybridization between the ZnO and BiOI surface orbitals (see Figure 21c), with 21% and 79% , respectively. However, since these states are located deep in the band gap, they may facilitate trapping of photoelectron at the BiOI/ZnO interface, thus hindering charge extraction and promoting non-radiative recombination, which might ultimately undermine the efficiency of the device. We will further discuss this effect in the following.

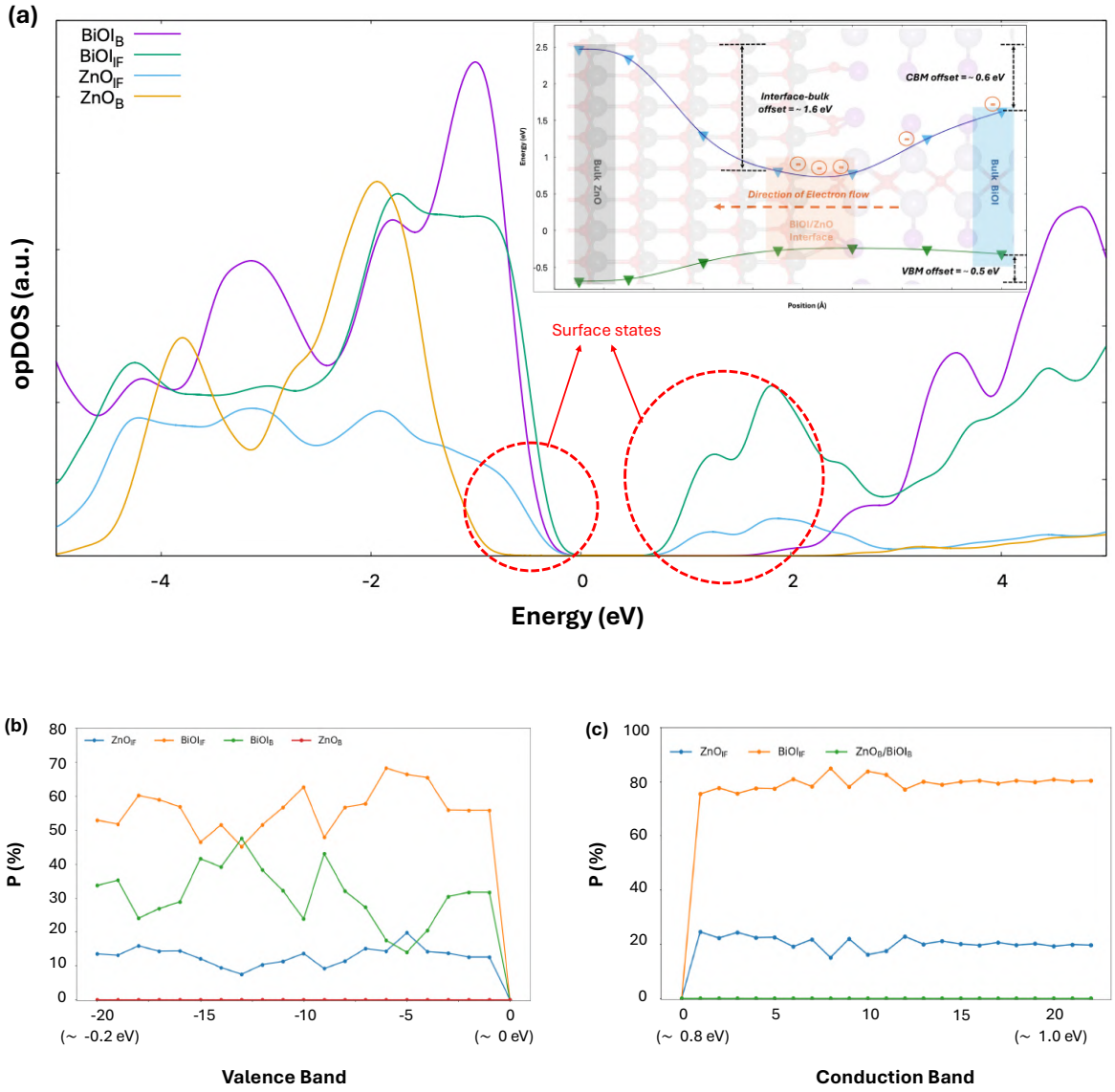


Figure 21: (a) Projected density of states comparison between bulk and interface. The inset shows the energy of the local frontier orbitals throughout the BiOI/ZnO heterostructure, (b-c) Quantitative analysis (in %) of the orbital contribution to VB and CB by interface and bulk atomic groups. Note that the CB is plotted starting at band index 0 for visualization. The actual bandgap is not 0, this is a relative shift. Start and end values of energies corresponding to the bands have also been indicated for clarity.

## 5.3 Orbital Projected Density of States(opDOS)

To better understand the origin of the surface states illustrated above, we computed orbital decomposed project density of states (opDOS), which measure the contribution to DOS arising from specific atomic orbitals (figure 22a).opDOSes reveal that the interface state due to ZnO near the VBM is dominated by O 2p orbital which hybridize with I 5p orbitals of BiOI to form the strong O-I bond at the interface. This bonding is promoted by the under-coordination of O from the metal oxide at the interface, which, in absence of binding to I, passed from 4, in the bulk, to 2 at BiOI/ZnO interface. O 2p/I 5p hybridization at the BiOI/ZnO interface is also at the basis of the gap states emerging from the CB. These indeed are mostly due to BiOI iodine ($\sim 75\%$) and ZnO oxygen ($\sim 22\%$), with some minor contribution from the other species (figure 22b). Similarly, the interface state near the VBM of BiOI is primarily derived from O 2p orbitals, which hybridize with Zn 3d orbitals to form O-Zn bonds at the interface. This is also facilitated by the change in oxygen coordination from 4 in the bulk BiOI to 2 at the interface, in absence of binding with Zn. To demonstrate the implications of these mid gap states on charge transfer, we traced the energy of local frontier orbitals. Focusing on photoelectron extraction, we follow the energy profile of an electron from the conduction band of BiOI to the conduction band of ZnO passing by the interface (inset of figure 21 ). The energy profile of photoelectrons presents a marked minimum at the BiOI/ZnO interface. This feature may play a double role: on the one hand, attract photoelectrons from the bulk, contributing to charge separation; on the other hand, trap electrons hinder extraction.

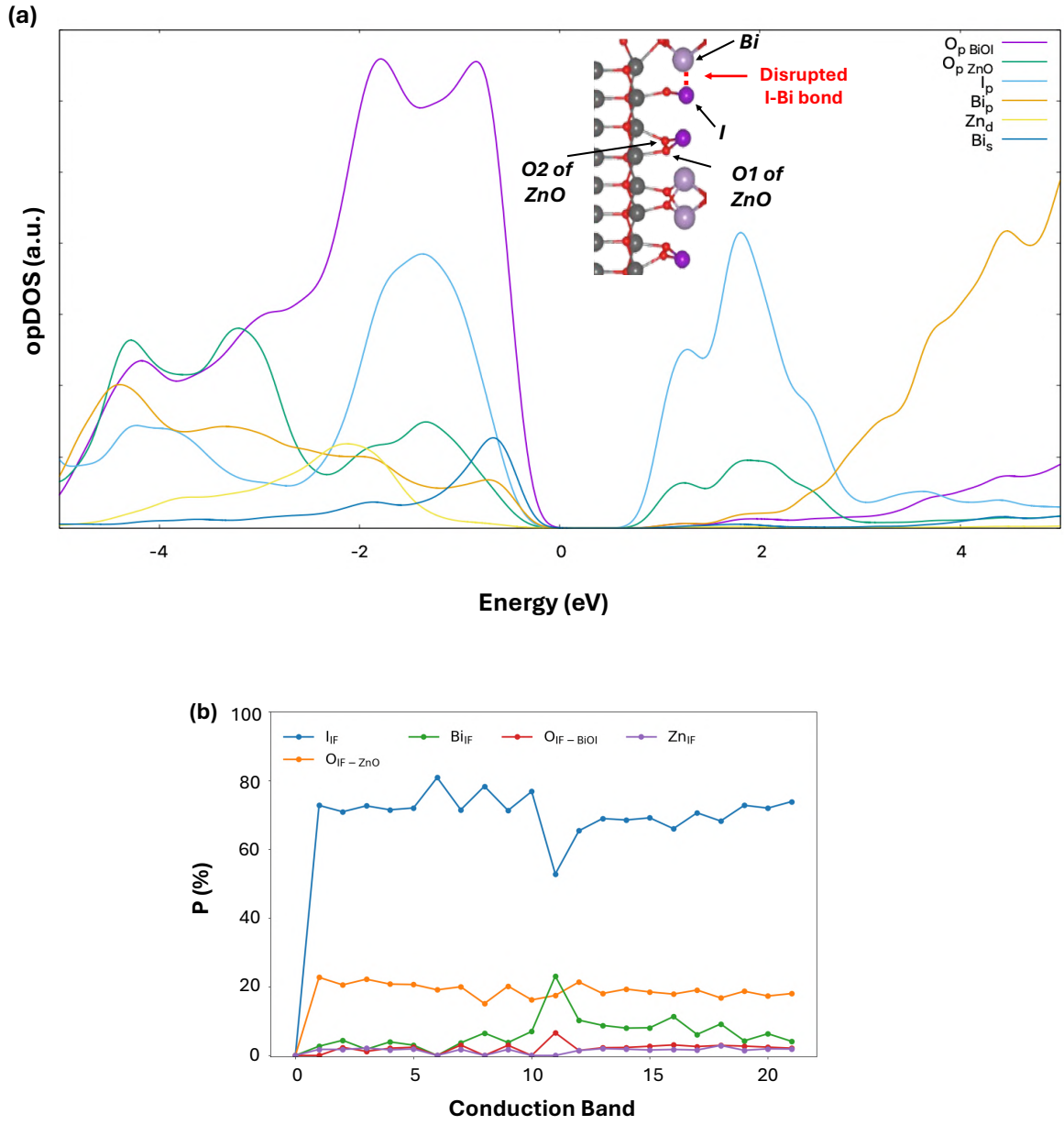


Figure 22: (a) Orbitals decomposed density of states projected on all atoms at the interface, (b) Quantitative analysis (in %) of the orbital contribution to mid gap states.

Moreover, following the electrostatic potential energy profile in Figure 23, from the bulk of BiOI to the bulk of ZnO, one notices a local minimum ($\Delta E^{\dagger}$= 0.44, corresponding to eV = 17.6$K_B$T confined to a limited region of space ($\sim$ 0.2 nm), in the

vicinity of the interface. This minimum, although confined to small regions of space, may hinder or slow down photoelectron extraction, preventing free diffusion of charge carriers across the interface between the absorbing material and the ETL layer. Slow extraction may result in non-radiative recombination, significantly limiting the PCE of the system.

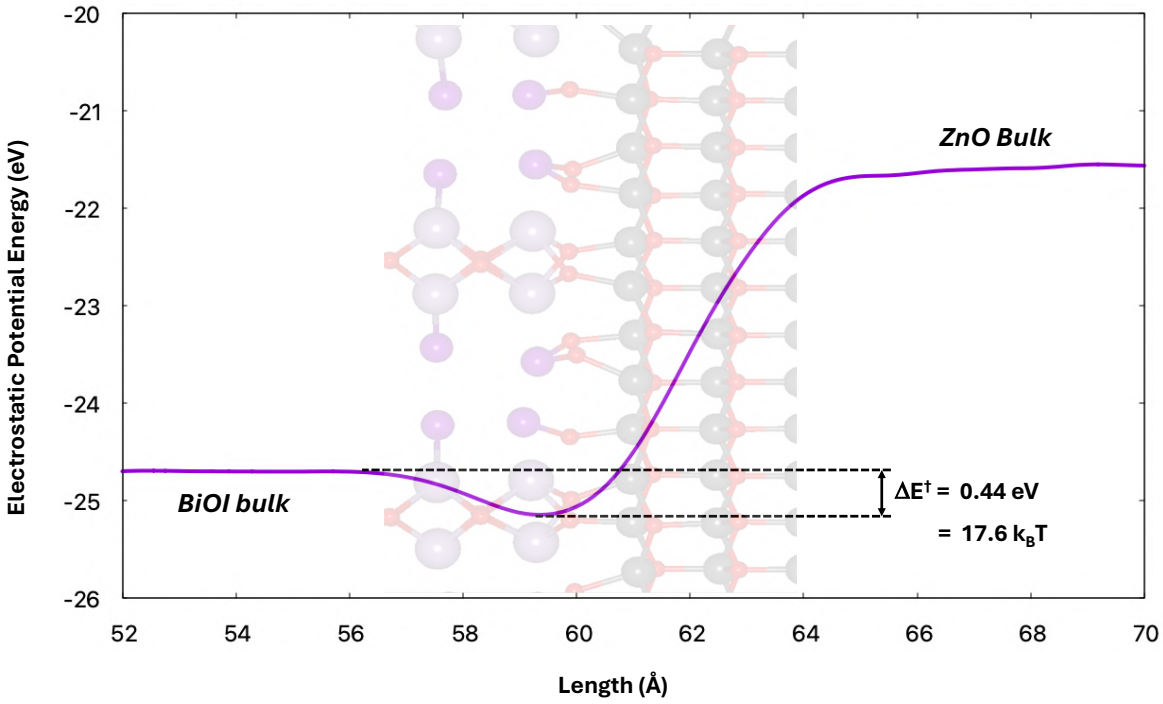


Figure 23: Electrostatic potential energy across the heterostructure.

## 5.4 Conclusion

In this work, we report for the first time, the atomic and the electronic structure of stable [110]BiOI/[010]ZnO heterojunction as obtained from DFT calculations. We show that BiOI and ZnO are bound by Bi-O-Zn bridge bonds of a mixed covalent and ionic nature. Atomic level structural analysis reveals that the formation of the interface leads to disruption of terminal Bi-I bond in BiOI, followed by a subsequent formation of the new bond between I and O from the metal oxide. While these struc-

tural modifications do not introduce deep gap states near the VBM, surface states with dominant contributions from I in BiOI and O in ZnO, were identified at $\sim 1$ eV below the CBM. Tracing the energy of the local frontier orbitals, we identified a minimum at the interface, a feature that may play a dual role; on the one hand it can attract the photo-generated electron from the bulk to BiOI, aiding charge separation, and on the other, it can trap electrons hindering extraction. Furthermore, the potential energy across the interface also highlights a spatially narrow barrier of 0.44 eV, that needs to be prevailed by electrons to move across the interface. Our atomistic level analysis lays the foundation for future rational interface engineering approaches aimed at optimizing charge transfer and minimizing recombination losses, ultimately advancing the development of high-performance BiOI/ZnO-based optoelectronic devices, including solar cells and photocatalysts.

## 5.5 Computational Methodology

DFT calculations were performed within the Perdew-Burke-Ernzerhof generalized gradient approximation (GGA)[173]. To accurately reproduce the experimental band gaps and the electronic properties of the interface system, Hubbard U corrections were applied. For ZnO, an on-site Coulomb correction was applied to the Zn3d ($U_d$= 7 eV) and O2p orbitals ($U_p$= 6 eV), with J = 0 due to the closed-shell nature of the involved atomic orbitals [201–203]. This choice yields band gaps in agreement with previous experimental and theoretical values [204] Dispersion corrections were also considered within the D3 Grimme scheme [205]. Calculations were performed using the Vienna ab Initio Simulation package (VASP). The Kohn-Sham orbitals were expanded in a plane-wave basis set with a cutoff energy of 400 eV, and interaction between valence electron and nuclei was described within the projector augmented-wave formalism [206].

The computational sample consisted of a $\sim 1.4$ nm [110] BiOI slab sandwiched between two $\sim 1.5$ nm [010] ZnO layers (ZnO/BiOI/ZnO). The thick layers allow for

recovering the bulk properties, e.g., the bulk density of states (DOSes) at their center. While this sandwich structure with generous layers requires more computational effort of a single BiOI/ZnO interface, it guarantees a zero electric dipole in the system, thus preventing artefacts associated to periodic boundary conditions (PBCs).The orientation of the BiOI slab was selected on the basis of experimental evidence [190] and, after a suitable plane rotations by 45° and 90°of the BiOI [001] and ZnO[100] respectively, we obtained an optimal matching between lattice parameters of the subsystems of the heterostructure, and a good chemical connectivity among the interface atoms (figure 20), as discussed.

The Brillouin zone of our slab system was sampled with $4 \times 1 \times 4$ K-points, where the direction sampled with the single K-point is the one along to the BiOI/ZnO interfaces [78]. All atomic positions were fully relaxed using a conjugate-gradient energy minimization algorithm. The ZnO/BiOI/ZnO composite system presents a "theoretical" strain arising from the lattice mismatch between the constituent materials. The theoretical strain is quantified as the percentage difference between the lattice constants of the isolated materials and those within the composite. This is given by the formula:

$$\text{Strain } (\%) = \frac{a_{\text{composite}} - a_{\text{BiOI}}}{a_{\text{BiOI}}} \times 100 \tag{39}$$

# 6 Interfacial behavior of Spiro-OMeTAD and T2 hole transport materials(HTMs) across crystallographic facets in hybrid lead halide perovskites

## 6.1 Introduction

Lead halide perovskites (LHP's) have emerged as leading candidates for cost-effective photovoltaic technologies owing to their excellent optoelectronic properties. However, the up-scaling of perovskite solar cells (PSCs) remains challenged by crystalline control, leading to a trade-off between device efficiency and active area. Solution-processed films often suffer from uncontrolled nucleation and growth, displaying disordered lattice orientation, non-ideal interfacial contact, severe defect accumulation and residual strain [175, 207–210]. This issue is particularly prominent in widely employed formamidinium lead iodide ($FAPbI_3$, FAPI) prepared with excess methylammonium chloride (MACl) in precursor, where crystallization preferentially follows a singular facet orientation, yielding uneven grain growth and microstrain in films. Consequently, the efficiency of even the best-performing PSCs still fall short of the Shockley-Queisser limit [211, 212].

Numerous approaches have been explored to improve device efficiencies. One of them involves replacing the original methylammonium lead iodide ($MAPbI_3$, MAPI) or FAPI with mixed-cation and mixed-halide compositions. Among these, the triple-cation/dual-halide perovskite $Cs_{0.05}(FA_{0.83}MA_{0.17})_{0.95}Pb(I_{0.83}Br_{0.17})_3$ ($MA = CH_3NH_3^+$, $FA = HC(NH_2)_2^+$) has become a benchmark owing to its excellent efficiency, improved stability, and reproducibility [6, 7, 112]. Another strategy focuses on controlling crystalline orientation to enhance charge transport [29, 211, 213, 214]. In particular, the (111) facet of $FAPbI_3$ has demonstrated a superior intrinsic moisture stability relative to (100), a higher carrier mobility than (110), and a lower work function compared to

both (100) and (110) [215–217].

Beyond this, the choice of hole-transporting material (HTM) interfaced with perovskite is also crucial, as it governs hole extraction. Among various HTMs, $2,2',7,7' - \text{tetrakis}(\text{N},\text{N} - \text{di} - \text{p} - \text{methoxyphenylamine}) - 9,9' - \text{spirobifluorene}$ (Spiro-OMetad), became the benchmark due to its efficient hole extraction, compatibility with dopants, and favorable valence band alignment with perovskites [218]. However, it suffers from several intrinsic drawbacks. Its synthesis is complex and costly, making it unsuitable for large-scale or industrial production[219]. Moreover, the dopants typically required to achieve high conductivity (e.g., lithium bis(trifluoromethanesulfonyl)imide, Li-TFSI) as well as metal atoms from the back electrode can migrate into the underlying perovskite layer, ultimately compromising long term device stability[220–222]. These limitations have motivated the search for low-cost HTMs that suppress ion migration, form stable coordination environments with adjacent layers, and retain high photovoltaic performance.

A promising candidate emerging from recent work by Zhou [218] is the T2 molecule, designed around a thiomethyl-substituted fluorene arm integrated into a $\text{spiro}[\text{fluorene} - 9,9' - \text{xanthene}]$ core. Experimental studies supported by theoretical analysis have demonstrated that T2 establishes stronger interactions at buried interface. Perovskite solar cells fabricated with T2 have achieved power conversion efficiencies of 26.21% (0.1 $\text{cm}^2$) and 24.88% (1.0 $\text{cm}^2$), underscoring its potential as a next-generation HTM.

Nevertheless, despite experimental evidence, atomistic level understanding of how these HTM's interact with specific perovskite surfaces like (100),(111) and (102) remains limited [111]. In this chapter, we investigate HTM/LHP interfaces, revealing how facet dependent surface chemistry affects or could affect charge extraction.

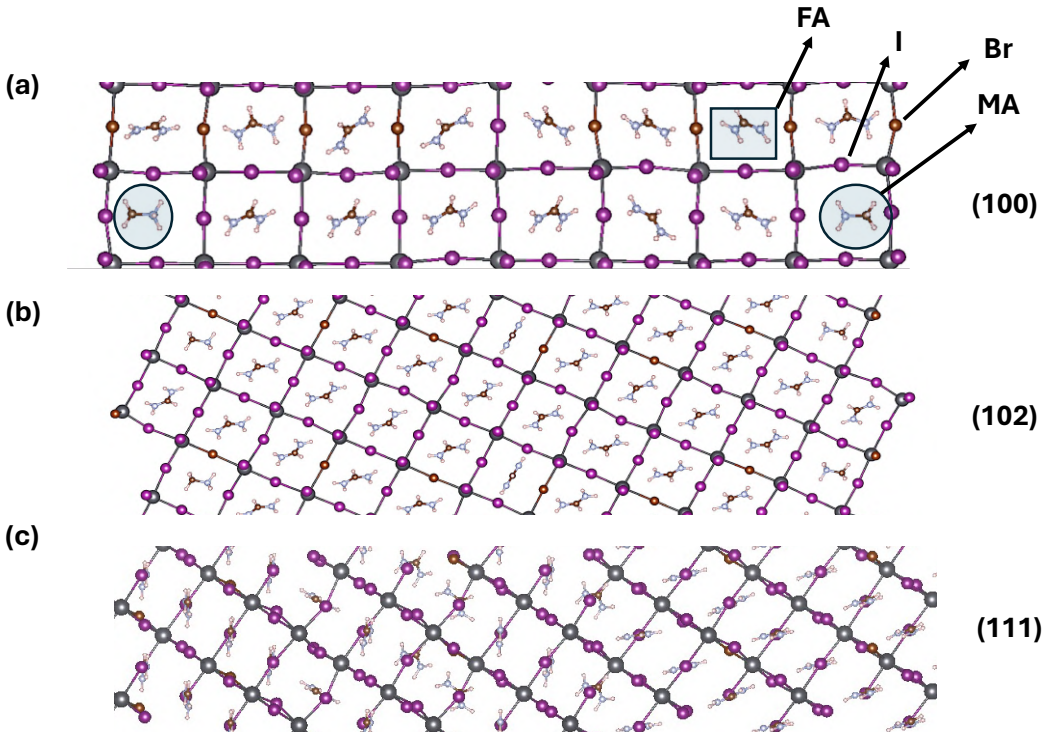


| Lattice constant (Å) | (100) | (102) | (111) |
|---|---|---|---|
| a | 53.305 | 99.570 | 85.01 |
| b | 18.896 | 6.36 | 14 |
| c | 6.33 | 14.22 | 12.66 |

Figure 24: Slab samples of $FA_{0.9}MA_{0.1}PbI_{2.7}Br_{0.3}$ perovskite and their respective lattice constants, considered for interface investigation. Note that these lattice constants are values excluding vacuum on either sides.

We begin by evaluating the work functions of the PbX terminated hybrid perovskite slabs in (100), (102), and (111) orientations (see figure 24 ). The trend in the values reported in table 25 for hybrid perovskite slabs follow the trend (100) > (102) > (111). This is in excellent agreement with experimental report ([217]), thereby validating the reliability of our computational slab setup. However, before studying

the interaction of these slabs with different HTM's, it is useful to establish how the intrinsic surface characteristics vary across these facets.

First, the coordination environment of surface Pb atoms, since in halide perovskites, this is a determinant of their ability to bind with HTM donor atoms [223–225]. Under-coordinated Pb centers are generally electron deficient and this is commonly associated with strong Lewis acidic character [225–229], especially because missing halides expose partially empty Pb 6p orbitals and can promote stronger binding with HTM [225, 230, 231]. Among the three surfaces, the (111) exposes predominantly three fold coordinated Pb atoms, which is halved with respect to six in the bulk. In contrast, the (102) surface contains a mixture of four and five fold, while the (100) surface exposes only five fold coordinated Pb atoms. Thus one would expect Pb atoms on (111) surface to be most electron deficient. To support this we performed Bader charge analysis on the bare slabs i.e. prior to HTM interaction, as they reflect the intrinsic electronic character of each facet without any induced perturbations. Although Bader charges do not provide a rigorous measure of Lewis acidic character, the increased positive charge density on Pb across the three surfaces (see table in figure 25) is at least qualitatively consistent with this coordination trend.

Based on coordination alone one would expect the (111) facet to exhibit a greater tendency to bind strongly with HTM donors like oxygen and sulfur, followed by (102) and (100). However, the picture is more complex since both oxygen and sulfur can each donate electron density, but sulfur is significantly more polarizable and possesses a tendency to behave as a softer base compared to oxygen [232]. Thus generally speaking, since surface Pb centers are borderline soft Lewis acids, Pb-S interactions are predicted to be more favorable than Pb-O [233]. The surfaces ability to bind with the two respective HTM's has been examined and discussed in the following subsections.

| Slab | Work Function (eV) for $FA_{0.9}MA_{0.1}PbI_{2.7}Br_{0.3}$ | Pb charge ($e/A^2$) |
|---|---|---|
| **100** | 6.13 | 0.035 |
| **102** | 5.63 | 0.047 |
| **111** | 5.41 | 0.055 |

Figure 25: Work function, surface and Pb charge density calculated for pure and hybrid perovskite slabs.

Therefore, next we studied the interaction of HTM's with these reliable bare slab samples. Note that, these are first of its kind results regarding the (102) and (111) orientation. Although the (111) has gained significant attention from experimental point of view due to the improved stability ([216, 217, 234]), both remain theoretically unexplored, especially for T2.

## 6.2 Structural response of (100), (111) and (102) surfaces to Spiro-OMeTAD

The various optimized Spiro/LHP interface structures can be seen in figure 26 (a-c). To rationalize the response of each surface on interface formation, we computed the adsorption distances of Spiro on perovskites surface, relevant atomic separations at the interface and the surface roughness ($\sigma$). The adsorption distances are defined as the distance between the centroid of the group of Spiro atoms (below plane P2) and the group of surface perovskite atoms (e.g., the highlighted region), as shown in figure 26 (a). The plane P2 is placed at a distance of $\sim 4$ Å from plane P1 for each surface. The position of P1 is set as the mean value of the surface Pb and halide atoms and is defined independently for each perovskite surface. Next, the surface roughness $\sigma$ represents the displacement of the perovskite surface atoms with respect to the reference plane P1, as illustrated in figure 26. To calculate the roughness, we consider atoms within a

window of ±1.0 Å from plane P1. Starting with the adsorption distance, among the studied orientations, the (100) facet demonstrates the shortest distance of 1.912Å compared to the longer (102) 2.12Å and longest (111) 2.8Å respectively (see table in figure 26). Because shorter adsorption distances generally reflect stronger molecule-surface interactions, the observed distances support the interaction strength hierarchy (100) > (102) > (111). A clear contradiction to the prior expectation, that was based solely on coordination of Pb atoms. However, adsorption distance is an averaged metric, meaning it cannot reliably capture the surface's response to Spiro, particularly because the binding can be asymmetric or it can anchor to multiple surface sites, thus missing out on local geometric changes. Hence it could incorrectly suggest interaction strength. To better understand how the surface accommodates Spiro, we subsequently evaluated the surface roughness $\sigma$ because it reflects local structural reorganization rather than an averaged height. While not a direct measure of interaction strength, surface roughness offers complementary insight into how strongly the surface geometry is perturbed by the HTM. Typically, $\sigma \sim 0.05 - 0.15$Å indicates lower roughness, $\sigma \sim 0.15 - 0.3$Å is moderate and beyond $\sim 0.3$Å considered to be quite rough [231, 235]. Indeed, one observes (table in figure 26 ) that surface roughness follows the trend-(100)>(111)≥(102). However, the relevant quantity for assessing Spiro induced structural changes is the increase in roughness, $\Delta\sigma$, rather than the absolute value. When examining $\Delta\sigma$ directly ( values in table of figure 26), the (111) facet shows only a negligible change upon interaction with Spiro, whereas both (100) and (102) exhibit appreciable increases. Consequently, the true trend of Spiro induced perturbation is (100) > (102) > (111). To complement this sequence, we quantified the $\Delta x$ (in Å) between the two oxygen atoms ($x_1$ encircled in black and $x_2$ in red) of Spiro, relative to P1, as shown in figure 26 (a). This provides a measure of molecular "tilt" i.e. how symmetric or asymmetric is the binding of Spiro on different surfaces. For example, higher tilt would correspond to $x_2$ being closer to P1 and $x_1$ being near to plane P2 as shown in figure 28. A smaller $\Delta x$ reflects a flatter configuration i.e. when both $x_1$ and $x_2$ being close to

P2. Multiple reports often associate higher tilt or asymmetric binding of an organic molecule on the perovskites surface to stronger bonding and enhanced electronic coupling [111, 236, 237]. The calculated $\Delta x$ values follow the order (111) $\sim 0.2 <$ (102) $\sim 0.78 <$ (100) $\sim 0.9$. This notably low $\Delta x$ for the (111) facet clearly agrees with the nearly flat (visually) geometry of Spiro on the surface and also complements the low ($\Delta\sigma \sim 0.02$) we observed. While the increased tilt as observed for (100) does complement the highest roughness and the suggested strongest interaction, the same cannot be said for (102). The high tilt (0.7 Å) in this case can be attributed to the intrinsic geometry of the surface i.e. absence of binding site, also evidenced by low $\Delta\sigma \sim 0.08$. More direct measures of interfacial interaction is provided by the number of anchoring sites and distances between relevant atoms at the interface. [111, 214].

Typically, Pb-O distances of 2.8-3.0 Å correspond to borderline strong interactions, values between 3.0-3.2 Å indicate weak to moderate interaction, and separations beyond 3.2 Å reflect non-bonded van der Waals contact [111, 238, 239]. On (100), the **two** Pb-O distances of 2.87Å and 3.004Å, suggests strong and direct coordination (see figure 26 (d)). In addition to Pb-O bonds that are the primary anchors at the interface, the hydrogen atoms on Spiro frequently engage in H-X(halide) interactions, that can influence both the geometry and the energetics of the interface [214, 240]. In hybrid lead-iodide perovskite (e.g methylammonium/formamidinium lead iodide), ab-initio molecular dynamic studies [241] define an H-acceptor distance cutoff for hydrogen bonding: d(H-I) $<$ 0.3 nm (i.e., 3.0 Å) for N-H donors. In the same work, for C-H donors, they used a less strict cutoff of d(H-I) $<$ 0.4 nm (4.0 Å ), but C-H-I hydrogen bonds are inherently weaker. More concretely, structural studies (crystal data) report H-I distances in the range $\sim$ 3.02–3.38 Å for C-H-I hydrogen bonds. Here, the minimum H-X distance (see figure 26 (g)) is $\sim$ 2.9 Å. Although this falls in the range of weak H-bonding [242], together with stronger Pb-O anchors, these could not only modestly enhance HTM's interaction with the perovskites surface, but also stabilize the interface. Moreover, it has been demonstrated to suppress halide motion near the

surface, a process associated with degradation in LHP's [242–244]. Nonetheless, (100) exhibiting the shortest H-X and Pb-O separations compared to the other two facets can be viewed as a further indication of the strong facet-spiro interaction.

In contrast, due to the intrinsic zig-zag geometry of (102) (see 26 (b)) facet supports only a **single** Pb-O bond, however of the same length 2.88Å (26 e) as observed on (100) surface. But the shortest H-X distance (26 (h)) increases substantially to 3.47Å, which diminishes the possibility of electrostatic stabilization of the interface. The (111) facet (figure 26 c) presents two Pb-O separations are 3.63Å and 3.74Å, which are too long to qualify as bonds and should be viewed as weak, non-covalent vdW contacts.

The geometric analysis reveals a distinct facet dependent interfacial behaviour between Spiro-OMeTAD and the perovskite surfaces. The (100) facet is dominated by five-fold coordinated Pb atoms, nevertheless forms two Pb-O contacts, one longer than the other but still within moderate coupling regime. This anchoring results in the largest surface roughness, which means that the (100) undergoes strongest perturbations due to Spiro. The (102) facet, in contrast, exposes a mix of four and five fold coordinated Pb sites but supports only a single Pb-O bond of $\sim 2.8$Å. Consistently, it displays the lower roughness w.r.t (100), marking it as less interactive facet. The (111) surface presents two much longer Pb-O distances (3.63 and 3.74 Å), despite the facts that the surface is dominated by under-coordinated three fold Pb atoms, falling into the weak interaction regime. This is also supported by the observed negligible ($\Delta\sigma$). Altogether, this point to the trend: (100) > (102) > (111), with (111) being least responsive to HTM, despite exposing the most under-coordinated Pb atoms.

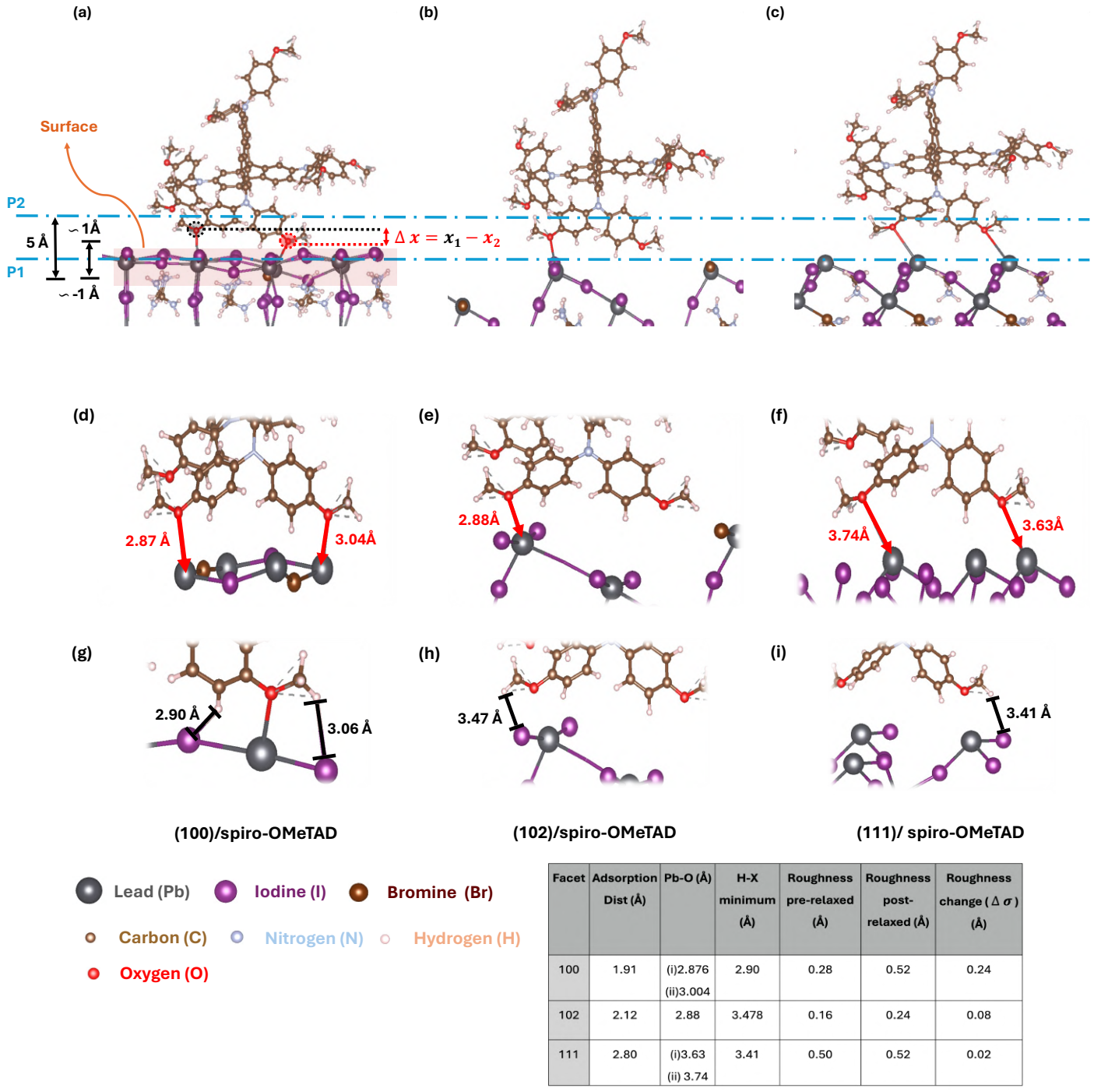


| Facet | Adsorption Dist (Å) | Pb-O (Å) | H-X minimum (Å) | Roughness pre-relaxed (Å) | Roughness post-relaxed (Å) | Roughness change ( $\Delta\sigma$ ) (Å) |
|---|---|---|---|---|---|---|
| 100 | 1.91 | (i)2.876 (ii)3.004 | 2.90 | 0.28 | 0.52 | 0.24 |
| 102 | 2.12 | 2.88 | 3.478 | 0.16 | 0.24 | 0.08 |
| 111 | 2.80 | (i)3.63 (ii) 3.74 | 3.41 | 0.50 | 0.52 | 0.02 |

Figure 26: Structural evolution post spiro's adsorption;(a,d,g) 100 surface; (b,e,h) 102 surface and (c,f,i) 111 surface. The planes P1 and P2 are displayed as a guide to understand how the adsorption distances, roughness and tilt were calculated (details in computational methodology). The table conatins all the evaluated parameters.

## 6.3 Structural response of (100), (111) and (102) surfaces to T2

We carried out a structural analysis for T2 analogous to spiro on different LHP surfaces. The Pb-coordination, adsorption distances, Pb-S separations, the shortest H-X distances, the extent of lattice roughness within the perovskite slabs and tilt of the HTM molecule, were evaluated (see interfaces in figure 28 (a-c)). As before, all descriptors referring to surface electronic structure namely Pb coordinations and Bader charges were obtained from the bare perovskite slabs, since these quantify the intrinsic reactivity of each facet prior to HTM interaction. Therefore, the prior analysis regarding the coordination or surface Pb atoms holds ie. based purely on coordination chemistry, one would anticipate the (111) facet with three fold under-coordinated Pb atoms to exhibit the strongest interactions.

The adsorption distances follow the sequence (102)<(100)<(111), with values of 2.90 Å, 3.10 Å and 3.26 Å, respectively. However, due to fact that adsorption height is a global descriptor that does not capture local geometry, this trend could incorrectly suggest interaction strength. Thus we computed surface roughness which interestingly reveals that all the surfaces responded identically, as indicated by the $\Delta\sigma$ values in table 28, to the presence of T2. This can be attributed to the **single** Pb-S coordination or only one anchoring site that T2 uses to interact with the three respective surfaces.

The (100) surface shows the shortest Pb-S distance (3.03 Å), followed by (111) with 3.15 Å and (102) at 3.25 Å. Computational studies on perovskite oxysulfides show that short Pb-S contacts of about 2.9 to 3.1 Å behave as true covalent bonds, whereas longer distances beyond 3.25Å correspond to much weaker, non-bonding interactions. Similar behavior is observed at thiol-passivated perovskite interfaces, where strong chemisorption and significant stabilization of $CsPbI_3$ appear only when Pb-S distances fall within the 3Å range. Thus, a clear trend emerges: Pb-S bond lengths around $\sim$ 3Å - 3.1Å indicate strong, stabilizing interactions, while longer distances signify weak or

secondary bonding [245–247]. Thus, these results suggest that with all the three surfaces, T2 likely forms a direct coordination. Based on the Pb-S lengths, the previously suggested trend of interaction strength now changes to (100)<(111)<(102). Next, we also evaluated the $\Delta x$ or what we called "tilt" (refer discussion on Spiro/LHP surface) values. While (100) and (111) showed equal and negligible tilt ($\Delta x \sim 0.03$), the (102) exhibited a significantly higher $\Delta x \sim 0.3$. This high tilt can be attributed again to the zig-zag configuration as discussed in the case of Spiro. We further examined H-X distances. The (100) facet exhibits the shortest H-X separation (3.07 Å), followed by (102) (3.445 Å), whereas (111) shows the weakest H-X interaction at 3.9 Å. Thus, the (100) facet benefits from both a relatively short Pb-S bond and H-X seperation, suggesting the strongest interaction with T2 as well. Notably, irrespective of the HTM i.e. Spiro or T2, both the (111) and the (102) surface are unlikely to benefit from H-X interactions, since both the surfaces exhibit separations beyond 3.4 Å. This appears to be an intrinsic limitation of these surfaces.

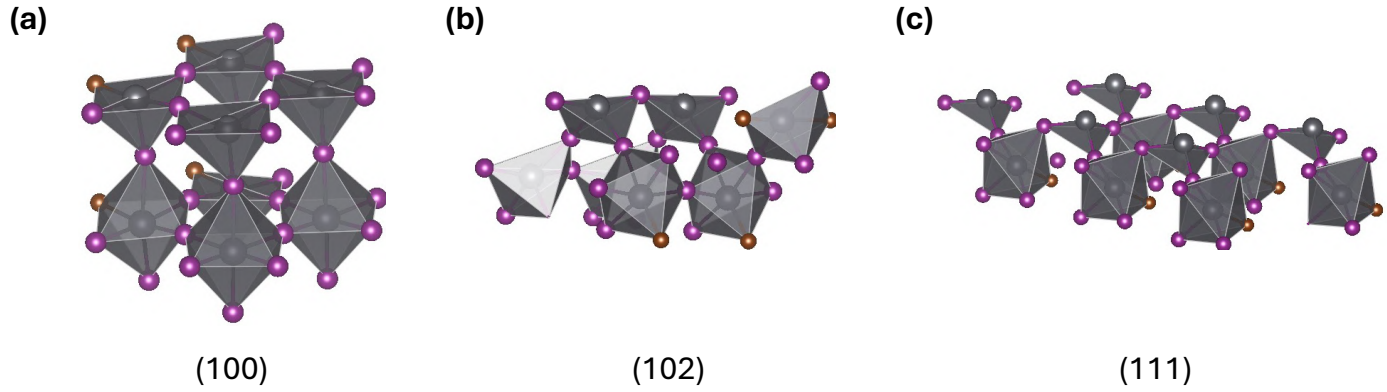


Figure 27: (a-c) Visual of bonding environment of Pb on (100), (102) and (111) surfaces. The slabs have been rotated for better view of the arrangement of surface Pb and I atoms.

It is observed that unlike Spiro, T2 interacts with the (111) surface through a Pb-

S interaction. We ***speculate*** that this is related to the local bonding environment of Pb on the (111) surface, which is highly constrained (see Figure 27 (c)). On this facet, Pb appears as an exposed "apex" above a compact triangular arrangement of three I atoms, with short Pb-I bond lengths of $\sim$ 3.03 Å, in contrast to the longer $\sim$ 3.10 Å and $\sim$ 3.09 Å observed on the (100) and (102) surfaces. This tighter triangular coordination likely reduces the ability of the Pb-I network to distort, and therefore the Pb center may not readily adjust its bonding direction. Here, "adjustment in bonding direction" refers to the capacity of Pb-I bonds and the associated hybridized Pb $6s^2/6p$ orbitals to reorient such that Pb can accommodate a donor like oxygen. This constraint matters for Spiro because Pb-O interactions typically require a specific approach orientation associated with coordination in Pb(II)-O complexes [248, 249]. In contrast, the (100) and (102) surfaces expose a larger and more complete portion of the $PbI_6$ octahedron (see Figure 27 (a–b)), offering greater flexibility for Pb-I distortions and orbital polarization, thus enabling the directional Pb-O interaction required for Spiro binding. Meanwhile, softer and more polarizable sulfur based ligands have demonstrated stronger binding to $Pb^{2+}$ at perovskite surfaces, often forming more favorable interactions than oxygen based donors [250, 251]. This supports the hypothesis that T2's Pb-S interactions can remain effective even on less favorable (111) surface. Furthermore, according to Hard-Soft-Acid-Base (HSAB) principles [233], sulfur functions as a soft donor capable of forming a more polarizable, partially covalent interaction with $Pb^{2+}$, which is classified as a borderline soft acid. This soft-soft affinity further rationalizes the robustness of Pb-S anchoring with different surface terminations. Interestingly, this hypothesis appears to align with our surface roughness calculations, where (111) shows negligible $\Delta\sigma$ for both HTM's (yet T2 bonds with the surface). The rigidity likely keeps Pb's electron cloud locked in a symmetric shape, preventing it from distorting to create the directional bonding region needed for Pb-O coordination, whereas the greater roughness of (100)/(102) reflects a more flexible surface that can accommodate the directional Pb-O coordination required for Spiro binding. We note

that this remains a hypothesis that needs to be tested.

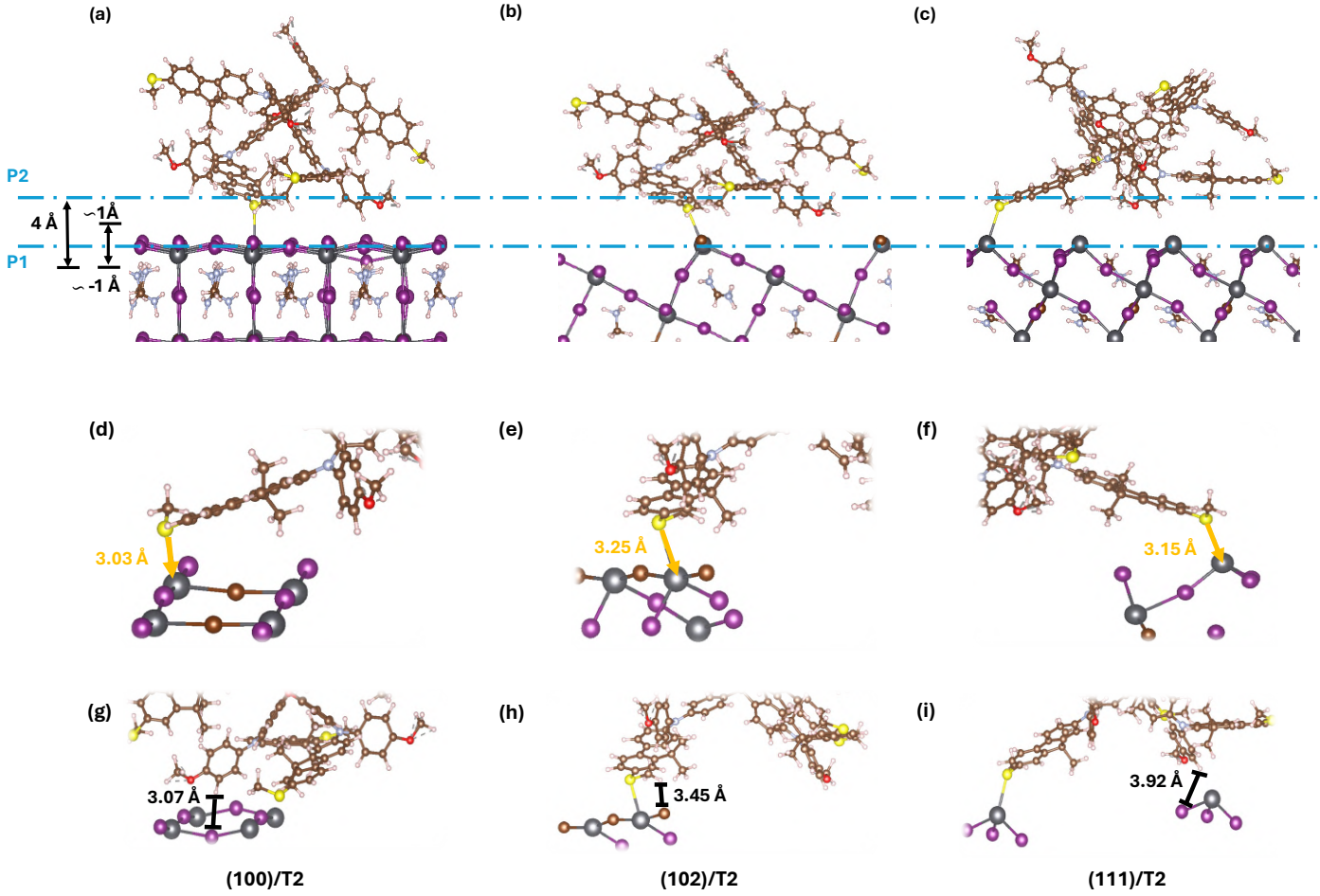


| Facet | Adsorption Dist (Å) | Pb-S (Å) | H-X minimum (Å) | Roughness pre-T2 (Å) | Roughness post-T2 (Å) | Roughness change ($\Delta\sigma$) (Å) |
|---|---|---|---|---|---|---|
| 100 | 3.102 | 3.033 | 3.073 | 0.28 | 0.310 | 0.03 |
| 102 | 2.899 | 3.251 | 3.445 | 0.16 | 0.181 | 0.02 |
| 111 | 3.262 | 3.151 | 3.93 | 0.41 | 0.447 | 0.03 |

Figure 28: Structural evolution post T2 adsorption;(a,d,g) 100 surface; (b,e,h) 102 surface and (c,f,i) 111 surface. The planes P1 and P2 are displayed as a guide to understand how the adsorption distances, roughness and tilt were calculated (details in computational methodology). The table contains all the evaluated parameters.

Having established the facet-dependent structural response to Spiro and T2, we next quantify the strength of these interfaces by evaluating the corresponding interaction energies ($E_{\text{int}}$) using the expression:

$$E_{\text{int}} = E^{\text{relaxed}}_{\text{interface}} - E^{\text{separated}}_{\text{LHP+HTM}}, \tag{40}$$

where $E^{\text{relaxed}}_{\text{LHP/HTM}}$ is the total energy of the fully relaxed LHP/HTM interface, and $E^{\text{sep}}_{\text{LHP+HTM}}$ denotes the single-point energy of the full LHP+HTM supercell with the geometry preserved but with the two subsystems translated such that their minimum separation is approximately 10 Å, so that no interactions occur between them. Negative values indicate an energetically favorable interface. For the (100) surface, strongly stabilizing interactions were obtained for both HTMs, with $E_{\text{int}} = -1.97$ eV for T2 and $-1.39$ eV for Spiro, indicating that (100) forms the most favorable interface and that T2 anchors more strongly than Spiro. The (102) facet exhibited weaker but still stabilizing interactions, yielding $E_{\text{int}} = -0.99$ eV for T2 and $-0.81$ eV for Spiro. In contrast, the (111) facet displayed unfavorability for both HTMs, with $E_{\text{int}} = +0.45$ eV for T2 and $+1.80$ eV for Spiro. These results show that, although T2 binds more favorably than Spiro on every surface, the (111) facet remains intrinsically the least compatible with either HTM. The overall energetic hierarchy is (100) > (102) > (111) for both HTMs. This aligns with the trends observed in the geometric analysis, underscoring the decisive influence of surface orientation and termination on HTM-perovskite interfacial behavior.

## 6.4 Electronic Coupling

Although the geometric descriptors have provided strong indications regarding the ability of each surface to accommodate the HTM's, charge transfer processes are ultimately dictated by the extent to which these structural interactions perturb the electronic environment. Therefore, to truly evaluate whether the observed geometric trends translate into meaningful electronic interactions, we now examine the density

of states projected on the perovskite surface, the bulk and the HTM (pDOS). Anticipating one detail, across all the studied facets, the bulk pDOS is nearly identical, indicating that the slabs are sufficiently thick to recover bulk-like electronic structure and that facet-dependent effects arise predominantly from the surface and interface regions. Note that, all the pDOSes were rigidly shifted such that the LHPs valence-band maximum (VBM) aligns with 0 eV.

Figure 29 (a and c) shows the projected density of staes (pDOS) for HTM/(100) interfaces. First and foremost, it is evident that the general characteristics of the pDOSes of the LHP is the same for both spiro and T2 ie. the surface layer dos shifts toward higher values with respect to the bulk pDOSes. This provides the generalized force driving holes form the bulk to the LHP/HTM interface. Moreover, the frontier orbitals of both HTM's lie higher in energy than LHP's valence band edge (VBE). Typically, a driving force of $\sim$0.2 eV or higher is sufficient for efficient extraction [111]. This is satisfied incase of both HTMs, nevertheless it can be clearly seen that the LHP's surface dos exhibits a larger shift with T2 as HTM. This indicates enhanced electronic coupling at the interface, which can promote a faster hole transfer. To clarify this we looked at the orbital contributions (in %) near the VBE of the perovskite slab (shown in figure 29 (b and d). In order to ensure a consistent comparison of the electronic coupling, we analyzed the state located $\sim$ 0.25 eV (highlighted region between bands -5 and 0) below the interfacial VBM. The contributions show that when interfaced with Spiro, the state is almost entirely composed of the Spiro orbitals (93%), with only a small mixture from perovskites surface (5.8%) and bulk (1.2%). This implies limited orbital overlap of Spiro with the surface. In contrast, it becomes significantly hybridized when interfaced with T2(57% T2, 39% perovskite surface, 4% bulk). According to the Marcus/Hush theory [252–254], the charge transport rate depends on the electronic coupling between initial ($i$) and final ($f$) states $H_{if} = \langle\psi_i|\hat{H}|\psi_f\rangle$. A larger coupling requires appreciable spatial overlap between frontier orbitals on the donor and acceptor, which in the present case corresponds to hybridization between

the HTM states and surface perovskite states. Since, T2 exhibits a higher overlap, one can expect it to be a better HTM than spiro. These results are qualitatively similar to the ones reported by Zhou et al. [218], with a distinction that this time there is some orbital mixing incase of spiro and perovskites surface near the valence band edge.

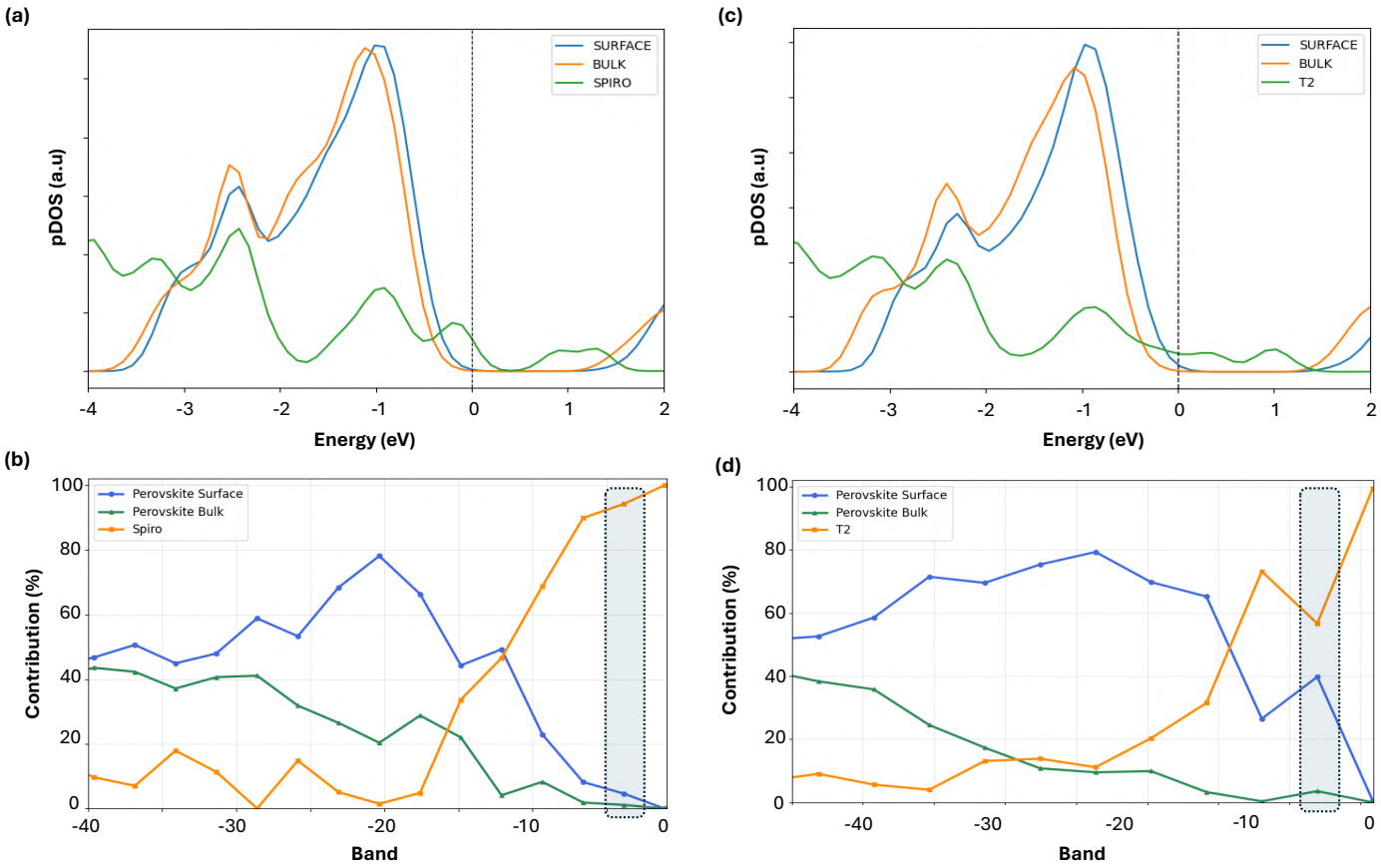


Figure 29: (a,c) Projected density of states comparison between bulk, interface and HTM's for (100);(b,d) Quantitative analysis (in %) of the orbital contribution upto 40 bands below slab valence band.

Next, we looked at the (102) facet with the two HTM's. In the figure 30 (a and c), the shift in surface pDOS with respect to the bulk ones is negligible irrespective of the HTM. This indicates the absence of the force driving holes from the bulk to the LHP/HTM interface. Nevertheless, again the frontier orbitals of both the HTM's lie

$\sim$ 0.2 eV above LHP. Looking at the highlighted state $\sim$ 0.28 eV below VBE (from bands -5 to 0) in figure 30 (b and d), it is evident that the Spiro orbitals dominate the state ($\sim$ 96%), with negligible contributions from the surface ($\sim$ 3%) and bulk ($\sim$ 1%). This indicates weak (even weaker than observed for (100)/Spiro) electronic coupling between Spiro and perovksite. In contrast, for T2 the same state exhibits substantially enhanced contributions from the perovskite, with 28% originating from T2, 41% from the perovskite surface, and 31% from the bulk, indicating stronger interfacial orbital overlap Following the argument presented previously, T2 again appears as a superior and effective HTM than spiro.

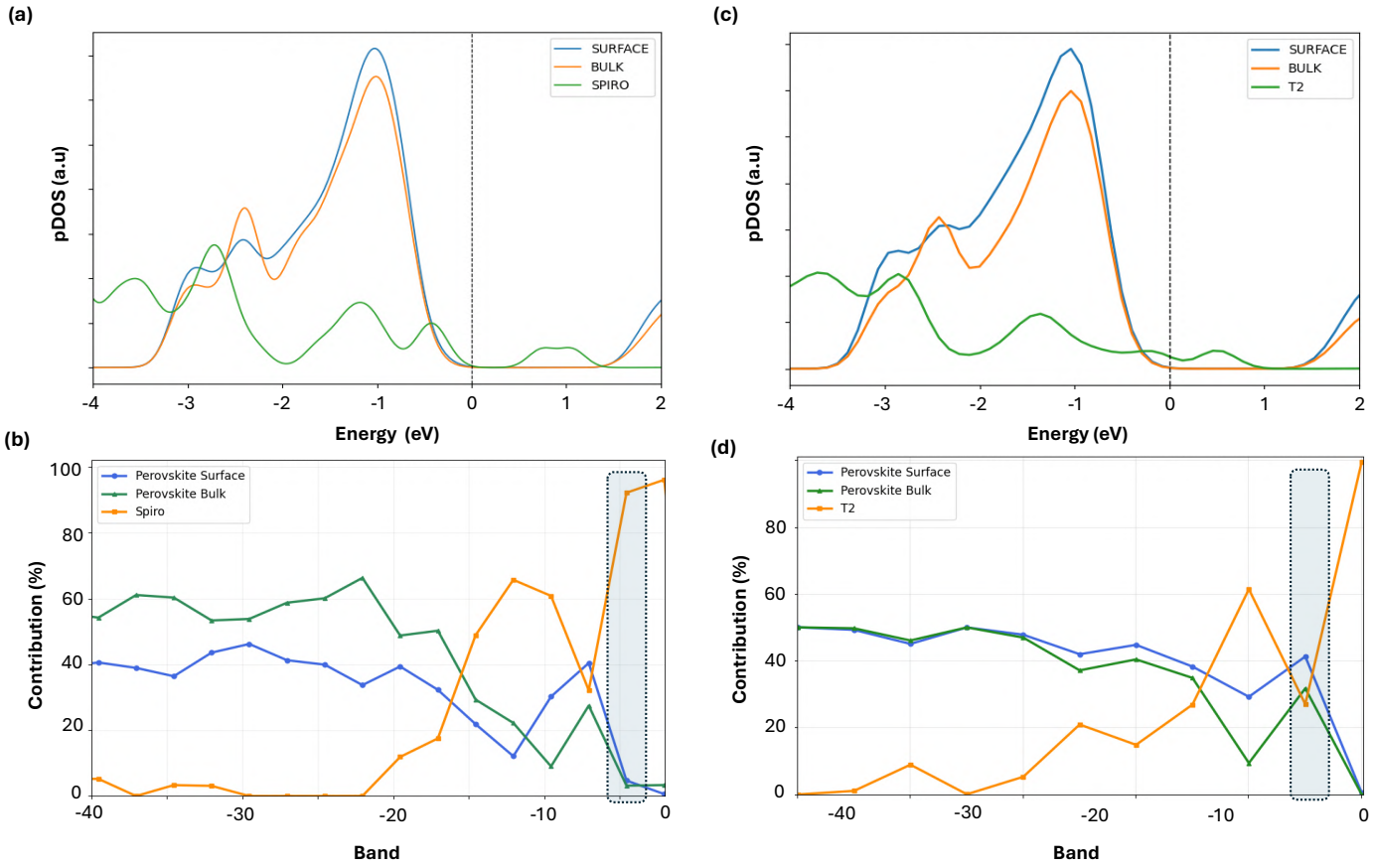


Figure 30: (a,c)Projected density of states comparison between bulk, interface and HTM's for (102);(b,d) Quantitative analysis (in %) of the orbital contribution upto 40 bands below valenece band of LHP.

For the (111) surface as well, we observe that the overall features of the of the pDOS remains consistent for both spiro and T2 interfaces. However, this time irrespective of the HTMs, the bulk pDOS is shifted to higher energies with respect to the surface. Such an energetic alignment implicates the presence of a "barrier" for hole extraction. Nevertheless, it is evident that this unconvenient upward shift of bulk frontier orbitals is significantly smaller ( $\sim$ 0.08 eV) for T2 on the surface as opposed to Spiro ($\sim$ 0.2 eV). An inspection of the orbital composition (31 (b-d)) roughly between the bands -3 to -7 (highlighted peak corresponding to the state 0.3 eV below the LHPs VBE) reveals that, while bulk contributions for both interfaces are similar ($\sim$ 22 %), the surface exhibits $\sim$ 5 % (for Spiro) and $\sim$ 2 % (for T2) respectively. Moreover, the contributions of both the HTM's are $>$ 70 %. What separates the two is that for Spiro, significant mixing with the perovskite is only observed upto $-0.3$ eV below the perovskites valence band, whereas in the case of T2, hybridization persists up to $-0.2$ eV (encircled), where we still see $\sim$ 3 % contribution from the surface. This proximity of hybridized states to the slabs band edge suggests a stronger electronic coupling at the T2 interface, enabling more efficient hole transfer. Thus, T2 is likely to extract holes more efficiently than spiro, provided the photo-generated charge carriers somehow diffuse to the interface.

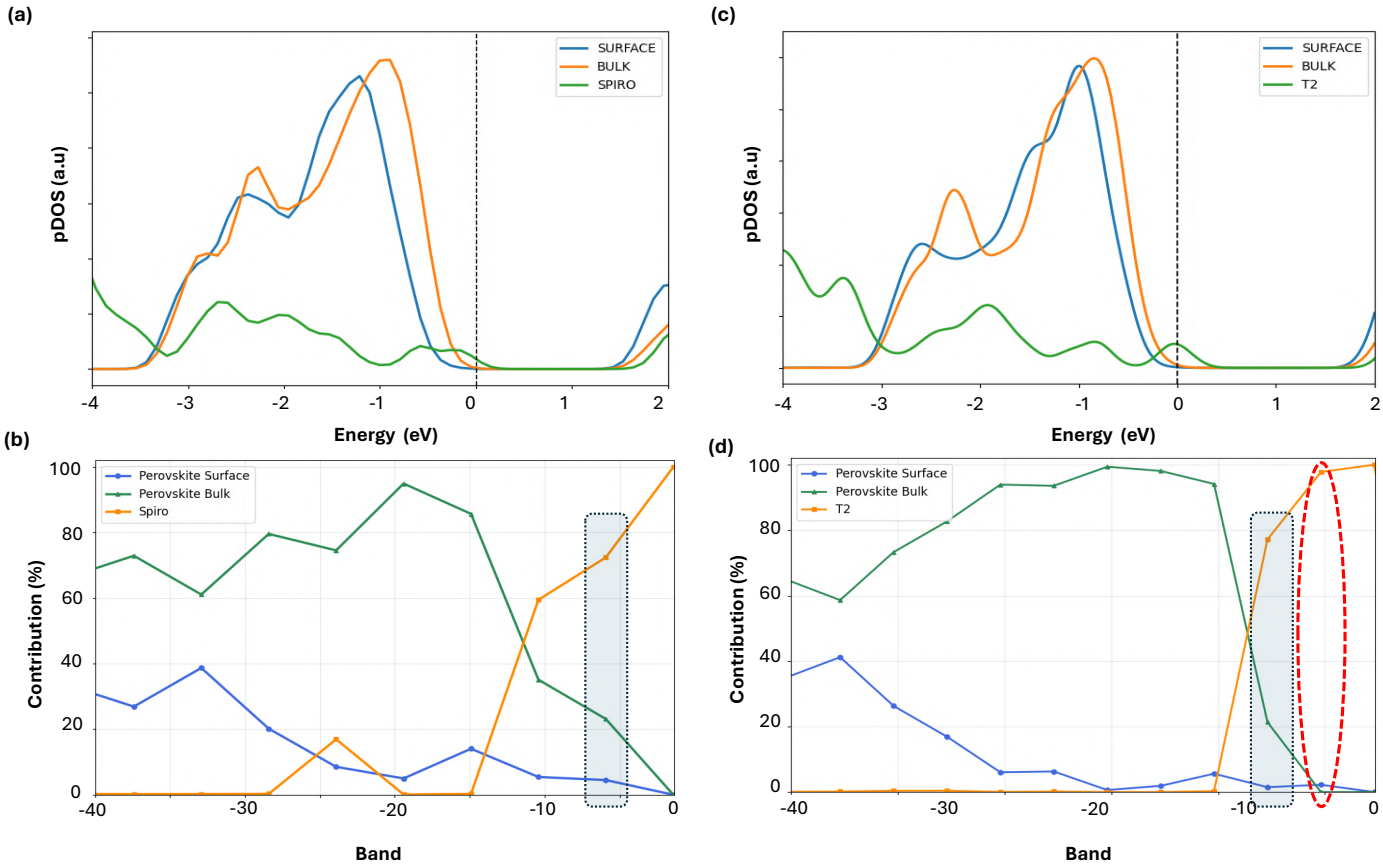


Figure 31: (a,c)Projected density of states comparison between bulk, interface and HTM's for (111);(b,d) Quantitative analysis (in %) of the orbital contribution upto 40 bands below LHPs valence band.

Across all three facets, a consistent relationship emerges between structural interaction strength and electronic hybridization at the valence band edge. T2 couples more strongly to the perovskite lattice than Spiro, particularly through the softer and more polarizable S donor that maintains bonded or borderline bonded Pb-S interactions on every facet. This produces a correspondingly stronger electronic response in the pDOS and orbital analysis, where we observe that T2 exhibits significantly greater hybridization at the VBM on all facets compared to Spiro.

Considering every evaluated metric, a clear facet hierarchy emerges. The (100)

surface is the most favorable for hole extraction as it shows: i) the largest pDOS shifts for perovskite's surface states exhibit a larger driving force to extract holes from the bulk;ii) the strongest orbital hybridization near the valence band edge with both HTM's (larger for T2), iii) the most robust structural anchoring for both HTMs and iv) largest energetic favorability. The (102) facet is consistently the weaker across structural and electronic descriptors with small pDOS shifts, reduced hybridization with HTM's, making it the less favorable facet compared to (100) for hole extraction with these HTM's. The (111) surface exhibits a rather diverse behaviour: i) despite being less favorable for Spiro due to the nature of Pb-O, it interacts appreciably with T2 via Pb-S bonding; ii) photo generated hole will be obstructed by an energetic "barrier" to go from bulk to the surface irrespective of the HTM's, although the "barrier" is halved when the surface is interfaced with T2 as opposed to Spiro ($\sim$ 0.2 eV); iii) lastly it yields a much better coupling with T2 as significant orbital overlap is observed near the valence band edge. Nevertheless, (111) remains the most unfavorable surface for hole extraction.

Overall, T2 is without doubt a superior HTM across all facets, and the (100) facet is the most favorable for hole extraction, followed by (102), with (111) being the least effective.

## 6.5 Conclusion

With this work we clearly highlight an interplay between interfacial bonding and electronic hybridization at the valence band edge of the perovskite slab. T2 consistently appears superior HTM than spiro as it couples more strongly to the lattice due to the higher polarizability and softer donor character of sulfur, which enables Pb-S bonding. This interaction translates directly into an enhanced hybridization of T2 states with the perovskite valence edge. When comparing facets, the (100) surface proves to be the most favorable for hole extraction, followed by (102), while (111).

## 6.6 Computational Methodology

Three hybrid perovskite slabs with the composition $FA_{0.90}MA_{0.10}Pb(I_{0.90}Br_{0.10})_3$ were constructed along the (100), (102) and (111) crystallographic directions. The slabs were generated by uniformly introducing MA (encircled in black) and Br ions throughout an initial $FAPbI_3$ lattice, as illustrated in figure 24. Each slab contained 8-9 atomic layers and included a vacuum spacing of $\sim$ 15 Å to avoid spurious interactions between periodic cells. The thickness of each slab was enough to recover bulk like behaviour for the central layer. All atomic positions were first fully relaxed. Subsequently, two different HTM molecules viz. spiro and T2, were placed at an initial separation of $\sim$ 3 Å above each slab surface and optimized again to yield six relaxed LHP/HTM interfaces. Due to the size of the molecules, the dimensions of each slab were adjusted to balance numerical accuracy and computational cost. Figure 32 (a-f) represents the six relaxed interfaces along with their dimensions. In this work, only $PbX_2$ terminated surfaces were considered since the strong electronic coupling with HTM's typically occurs through Pb (Pb-O, Pb-S etc). Electronic structure calculations were performed within the Perdew-Burke-Ernzerhof (PBE) generalized gradient approximation, using VASP. Kohn-Sham states were expanded in a plane-wave basis with a kinetic energy cutoff of 400 eV. Core-valence interactions were treated with the projector-augmented wave method [77]. The Brillouin zone has been sampled with $1 \times 4 \times 4$ K-points [78]. The following procedure describes how the adsorption distance and surface roughness have been calculated.

### 6.6.1 Adsorption Distance

The adsorption distance between HTM atoms (between plane P2 and above the perovskites surface) and the perovskite surface atoms (within $\pm$ 1 Å of plane P1) is evaluated from their centroids. For each group of $N$ atoms with coordinates $\vec{r}_i$, the

centroid is defined as:

$$\vec{R} = \frac{1}{N} \sum_{i=1}^{N} \vec{r}_i, \tag{41}$$

where $\vec{R}_S$ and $\vec{R}_T$ denote the centroids of the perovskite surface atoms and the HTM atoms, respectively. The adsorption distance is then calculated as:

$$d_{\text{ads}} = |R_{T,x} - R_{S,x}| \tag{42}$$

### 6.6.2 Surface Roughness

For each facet, we isolate the interfacial perovskite layer by selecting only the inorganic atoms (Pb and halides, X=I,Br) whose coordinates fall inside a window of

$$x_{\min} \leq x_i \leq x_{\max} \tag{43}$$

Within the window, we define a local reference position $x_{\text{ref}}$ as the mean of all Pb and halide coordinates:

$$x_{\text{ref}} = \frac{1}{N_{\text{Pb}} + N_{\text{X}}} \left( \sum_{i \in \text{Pb}} x_i + \sum_{j \in X} x_j \right), \tag{44}$$

where $N_{Pb}$ and $N_X$ are number of lead atoms and halide atoms respectively. The plane P1 as illustrated in figures 26 and 28 represents the $x_{\text{ref}}$. The displacement of each atom $k$ is then calculated relative to this reference as:

$$\Delta x_k = x_k - x_{\text{ref}}. \tag{45}$$

Finally, the geometric roughness (in Å) is the root-mean-square spread of Pb+X about the reference:

$$\sigma = \sqrt{\frac{1}{N_{\text{Pb}} + N_{\text{X}}} \sum_{k \in \text{Pb} \cup X} (x_k - x_{\text{ref}})^2}. \tag{46}$$

Larger $\sigma$ implies a more corrugated interface.

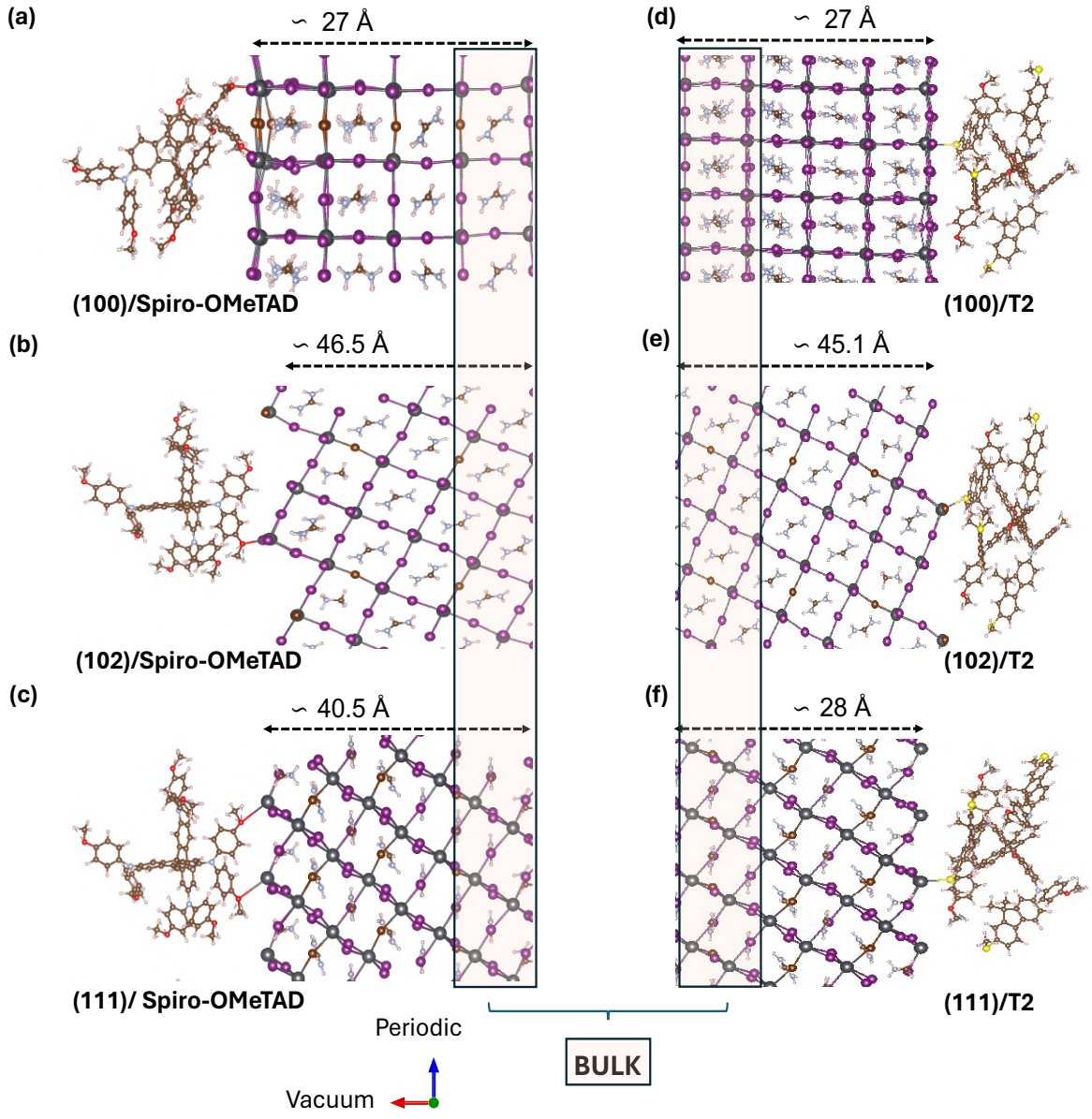


| Lattice constant (Å) | 100 / Spiro | 102 / Spiro | 111 / Spiro | 100 / T2 | 102 / T2 | 111 / T2 |
|---|---|---|---|---|---|---|
| a | 75.872 | 99.570 | 104.472 | 25.35 | 28.44 | 35.98 |
| b | 18.896 | 19.083 | 26.988 | 37.79 | 31.80 | 31.16 |
| c | 25.350 | 28.448 | 23.372 | 85.25 | 110.57 | 97.47 |

Figure 32: Interfaces considered for calculations. Note that these lattice constants are values including vacuum on either sides. Highlighted region represents the bulk.

# 7 Comparative Study of Passivants for Improved Hole Transport in Hybrid Lead Halide Perovskite Solar Cells

In the preceding chapter, the interaction mechanisms between Spiro and T2 hole transport materials were explored from an atomistic perspective, providing crucial insights into the interfacial atomic and electronic structures, with possible implications for charge transfer properties. Building on these computational findings, this chapter shifts focus to the experimental outcomes resulting from the introduction of various passivant materials at the interface between the absorber and the hole transport material (HTM). Before discussing the results, I would like to mention that these experiments were performed in collaboration with the University of Porto as part of a mandatory research period (3 months in this case) during my doctoral studies. This investigation is still ongoing; however, I will present the results that have been processed so far.

## 7.1 Introduction

Perovskite solar cells (PSCs) operate through a sequence of light absorption, charge generation, separation, and transport processes, as summarized in Figure 33. Upon absorption of photons with energies greater than the perovskite bandgap ($h\nu > E_g$), electrons transition from the valence band (VB) to the conduction band (CB), leaving behind holes. The low exciton binding energy in perovskite materials ($\sim$ 26 meV, comparable to room temperature $k_BT$) enables rapid dissociation of excitons into free charge carriers, which subsequently diffuse toward the electron transport layer (ETL) and hole transport material (HTL) [255],[256]. Efficient carrier extraction depends on these charge carriers successfully reaching the electrodes before recombina-

tion, thus making extended carrier lifetime an essential aspect for maximizing efficiency. Therefore, one can generalize that a PSC's performance is determined by a combination of efficient light absorption, effective charge separation, long carrier diffusion lengths, and minimal recombination losses.

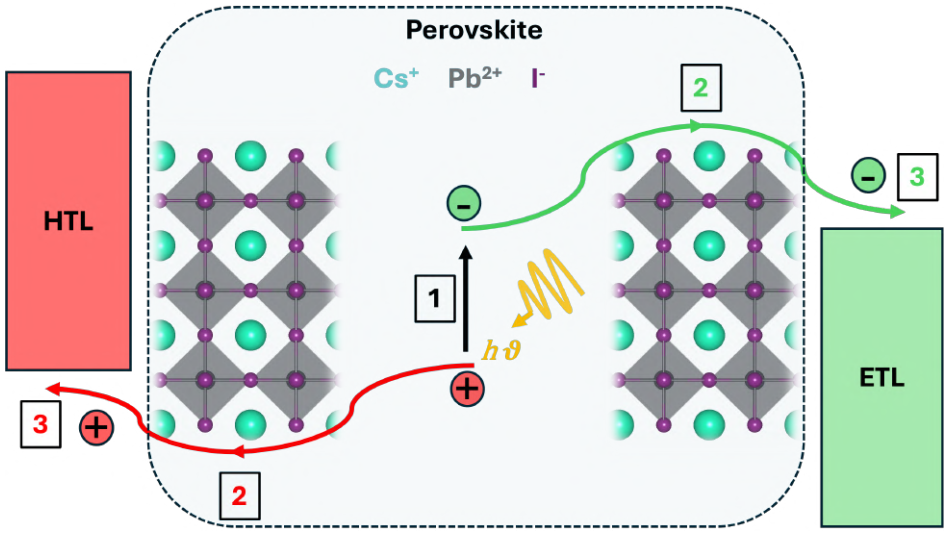


Figure 33: Schematic of operation sequence of charge carriers.

Typically, perovskite cells are fabricated with solution-based methods, which often introduce defects. Extensive literature has shown that bulk defects are shallow, owed to the peculiar electronic structure of the light absorbing material. This led to the introduction of the concept of defect tolerance. Defects at surfaces and interfaces, on the contrary may be detrimental. Surface defects may act as carrier trap centers and accelerate non-radiative recombination losses [175, 207–210]. Additionally, thermal annealing, that is a crucial step in fabrication process, can also lead to the partial loss of cations, producing non-stoichiometric surfaces enriched with ionic defects that can act as highly active non-radiative recombination sites [257–259]. Beyond this, the layered configuration of PSCs inherently generates numerous heterointerfaces that also serve as non-radiative recombination centers for photogenerated charge carriers.

Interfacial defects, predominantly located at the perovskite surface and at junctions with charge transport layers, are thermodynamically favorable to form owing to their low formation energies[260, 261]. These defect states perturb the interfacial electronic structure, inducing deep trap levels that hamper interfacial charge transfer dynamics and consequently limit carrier extraction efficiency [2, 262, 263]. Therefore, effective defect passivation, particularly at surfaces and interfaces, is critical for suppressing losses and improving device efficiency[256]. Passivation can also mitigate the intrinsic instability of perovskite absorbers by neutralizing defects that would otherwise trigger degradation. Thus, suitable passivation agents such as Lewis bases, halide or ammonium salts, polymers, and low-dimensional perovskite layers can coordinate with under-coordinated $Pb^{2+}$ sites or compensate halide vacancies, thereby suppressing defect assisted ion migration and the associated instability [264, 265].

Incorporating alkylammonium organic cation has emerged as a highly effective passivation strategy for 3D perovskite solar cells due to their hydrophobic nature and the fact that its incorporation allows tuning of optoelectronic properties. Generally speaking, integrating these organic moieties can either lead to the formation of a low-dimensional perovskite phase (also referred to as the 2D phase), resulting in a 2D/3D configuration (see illustration in 34), or can simply interact without froming a 2D phase over the 3D absorber surface [30, 266]. Both approaches can passivate the surface of the 3D perovskite absorber. However, when formed, the low-dimensional 2D phase/layer offers numerous advantages [267–269]: (1) it enhances the stability against humidity; (2) by optimizing the energy-level structure, it promotes carrier transport from the perovskite layer to the transport layer, thereby reducing leakage current losses and reverse electron transfer; (3) it reduces the defect-state density and inhibits ion migration, which helps mitigate photocurrent hysteresis etc. In-fact, state of the art devices employing 2D/3D configuration, have now achieved a power conversion efficiencies exceeding 24% [269, 270] while maintaining over 90% of their initial performance after 1000 h under humid or thermal stress conditions. These advances establish low-

dimensional perovskite passivation as a key pathway toward stable, high-performing perovskite cells.

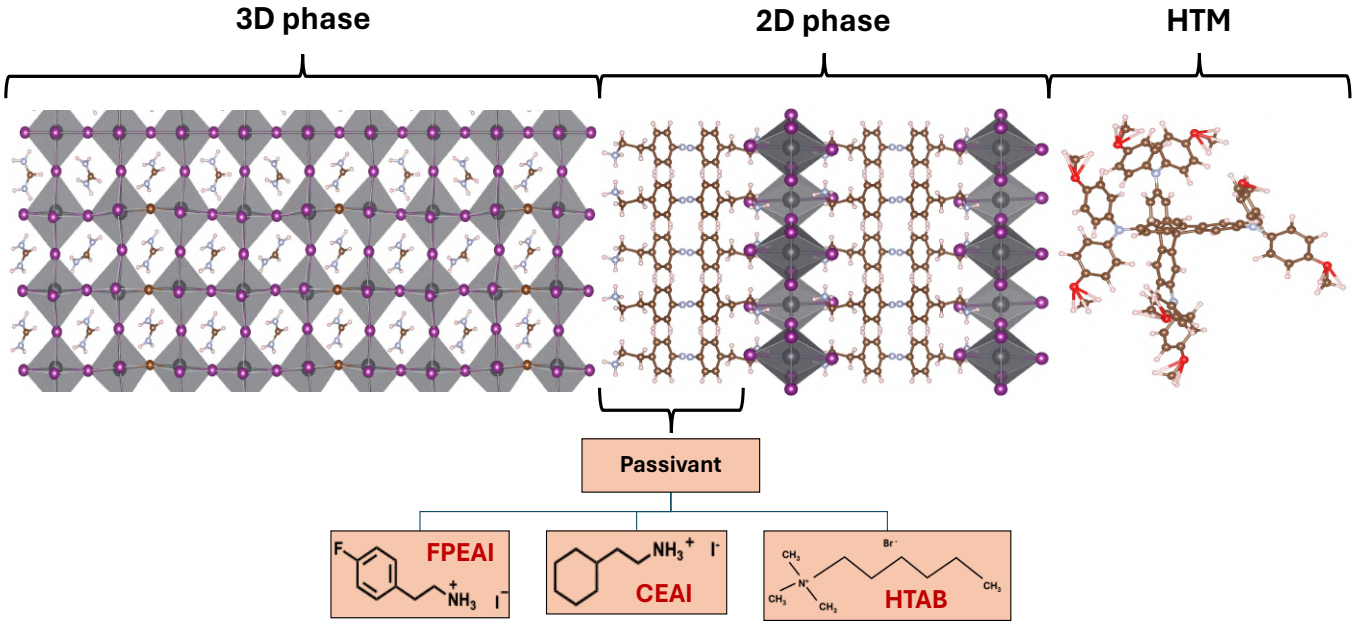


Figure 34: A cartoon illustration of passivation molecule introduced between the perovskite absorber and Spiro-OMetad. In this study, we introduced molecules (details are discussed later in the chapter) that are displayed in the chart below, in similar fashion. Note that this is just an illustration and formation of 2D phase is subject to a variety of control parameters.

Extensive works on 2D/3D interface engineering, such as the use of phenethylammonium iodide (PEAI) to form stable Ruddlesden-Popper (RP) 2D phases for enhanced surface protection [271]; guanidinium-based cations to improve interfacial energetics and stability [272]; and fluorinated organic cations that impart hydrophobicity and suppress trap-mediated recombination [213], consistently report gains in power conversion efficiency, open-circuit voltage, and stability. However, in the literature, reports typically emphasize only on the maximum performance achieved with

a specific passivant and frequently present it as the most effective strategy. Since device architectures, fabrication methods, and testing protocols vary significantly across reports, discrepancies remain as to whether performance improvements arise from the intrinsic chemistry of the passivant or from process-dependent optimizations. Indeed, direct comparisons between different passivants under identical processing conditions are scarce, and comprehensive, systematic evaluations of films fabricated with diverse passivants within the same environment are still lacking.

Inspired by this, in this chapter we investigate the impact of surface passivation on the performance of perovskite solar cells (PSCs) with an n-i-p architecture by employing halide-based passivators, namely 2-cyclohexylethylammonium iodide (CEAI), 2-(4-fluorophenylethyl)ammonium iodide (p-FPEAI), and hexyltrimethylammonium bromide (HTAB). Henceforth, the thin-film device without any passivant will be referred to as the reference. Correspondingly, the passivated films, samples, and devices are denoted as CEAI-, FPEAI-, and HTAB-passivated, respectively, as shown in the figure 34, along with the chemical structures of the passivating molecules. The device configuration employed for measurements, consists of fluorine-doped tin oxide (FTO)/compact-$TiO_2$/$SnO_2$/3D/2D/Spiro-OMeTAD (HTL)/gold(Au), where the 3D absorber comprises of an optimized $Cs_{0.05}FA_{0.85}MA_{0.10}Pb(I_{0.95}Br_{0.05})_3$ formulation fabricated according to the procedure described in the thin-film fabrication subsection. After perovskite deposition and annealing, the passivating solutions of CEAI, FPEAI, and HTAB were dispensed onto the perovskite films (sequential deposition) under identical spin conditions, i.e., at 5000 rpm with an acceleration of 2000 rpm.s$^{-1}$ for 60 s. Table 35 provides an overview of (i) the concentrations investigated; (ii) the annealing temperatures and iii) annealing time, of the passivants studied. It is important to note that, given the numerous parameters requiring optimization, the annealing time for FPEAI (when annealed) and CEAI was set to 10 min (to maintain uniformity), which falls within a typical range of 5-30 min based on previous literature reports ([266, 273, 274]). In the case of HTAB, we obtained an optimized time of 1 minute

because increasing the time further destroyed the cells efficiency.

| PSC | Concentration (solvent-IPA) ($mg.mL^{-1}$) | Annealing time (min) | Annealing Temperature (°C) |
|---|---|---|---|
| CEAI | 2 | 10 | 100 |
| CEAI | 2.5 | 10 | 100 |
| HTAB | 0.7 | 1 | 100 |
| HTAB | 1.6 | 1 | 100 |
| HTAB | 2.5 | 1 | 100 |
| FPEAI | 2.5 | No Annealing | |
| FPEAI | 4 | | |
| FPEAI | 2.5 | 10 | 100 |
| FPEAI | 4 | 10 | 100 |

Figure 35: Details of the cases studied for the three passivants CEAI,FPEAI and HTAB. The cases highlighted in black belong to the first batch of fabricated cells, while the cases in red were an addition to the second batch we fabricated (discussed in detail in the main text). To maintain consistency, we did fabricate and test all the cells again for the second batch as well.

## 7.2 Experimental Outcomes

As a first step, we wanted to optimize the concentration of each passivant. Thus, we fabricated and evaluated the J-V characteristics (figure 36 (a-c) of the first batch (inked in black in the table 35) of our cells. The photovoltaic parameters including open circuit voltage ($V_{oc}$), short circuit current density ($J_{sc}$), fill factor (FF), and power conversion efficiency (PCE) were extracted for all the films and were monitored every-day for the first three days after fabrication. Measurements were performed according to the protocol explained in the characterization section of this chapter.

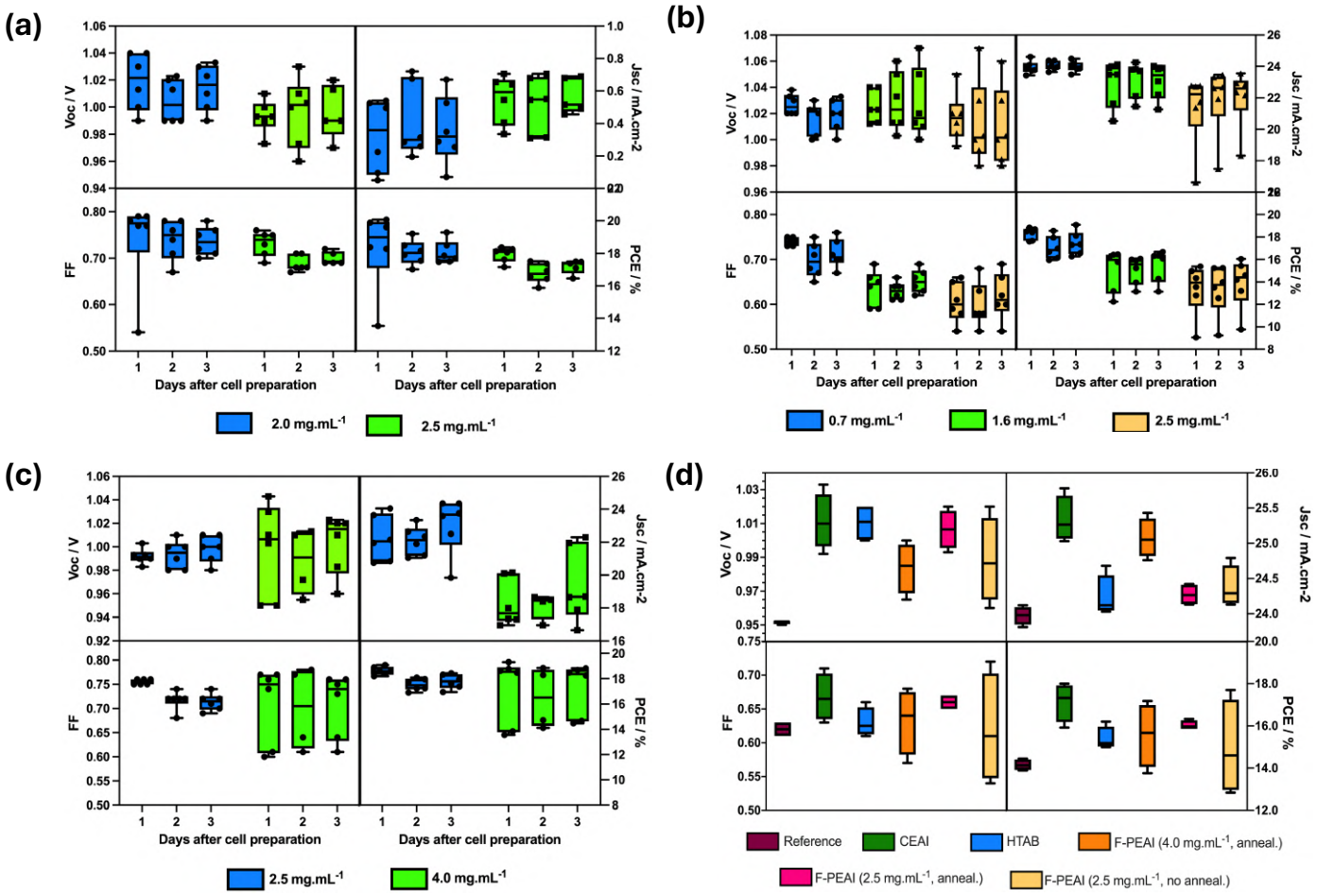


Figure 36: J-V characteristics of all the studies configuration; (a-c) represent the characteristics of CEAI-, HTAB- and FPEAI- passivated films from the first batch and (d) from of the second batch of cells. Note that in (d) there are two additional cases considered. This has been discussed in the latter text.

In Figures 36 (a–c), we report the performance of devices fabricated with the same perovskite absorber but passivated using different molecules, all of which exhibited notable enhancement compared to the reference device. The Ref (indicated in figure 37) showed an efficiency of approximately 14%, with $J_{sc}$, $V_{oc}$, and FF values of $\sim$21 mA.cm$^{-2}$, $\sim$0.94 V, and $\sim$0.69, respectively. Comparing these Ref values to passivated samples, it is evident that irrespective of the concentration considered here,

the efficiency consistently improves upon passivation, although the magnitude of improvement varies across different passivants. The improvement in the passivated cells primarily stems from a significant increase in the $J_{sc}$ and $V_{oc}$, which directly contributed to the overall efficiency gains. Diving into the details, for CEAI and HTAB, the champion efficiencies of ∼20% and ∼18.5% are obtained for concentrations of 2 mg.mL$^{-1}$ and 0.7 mg.mL$^{-1}$, respectively. Although at higher concentration (2.5 mg.mL$^{-1}$) of CEAI, the PCE shows an expected but not obvious minor drop by ∼0.8%, the effects for HTAB are far more drastic. Across the three HTAB concentrations (see figure 36 (b)), the 0.7 mg.mL$^{-1}$ and 2.5 mg.mL$^{-1}$, consistently (over the days) exhibit the highest and lowest values of the measured parameters, while intermediate values are noted for 1.5 mg.mL$^{-1}$. The $V_{\mathrm{oc}}$ and $J_{\mathrm{sc}}$ are only moderately affected; however, the FF drops by nearly 20%. At the highest HTAB and CEAI concentrations, the surface is likely over-passivated, resulting in a thick insulating alkylammonium layer that hinders charge extraction. Such over-passivation can increase the series resistance of the device, consistent with previous reports on excessive long-chain alkylammonium treatments[37, 275–277]. As for FPEAI, we observed that for both concentrations, the FF remains largely unchanged, while $J_{\mathrm{sc}}$ decreases (similar to HTAB) and $V_{\mathrm{oc}}$ increases likely due to reduced recombination, for the higher concentration (4 mg.mL$^{-1}$). Despite these variations, the PCE values remain relatively close, around ∼19% for both concentrations. It is interesting to note that with HTAB, at higher concentrations, the $V_{\mathrm{oc}}$ and $J_{\mathrm{sc}}$ both decrease as opposed to FPEAI (4 mg.mL$^{-1}$), where only the $J_{\mathrm{sc}}$ decreases.

Next, the evolution of their photovoltaic parameters was monitored over an extended period of +1000 hours in the dark(see figure 37), to gain insight into the temporal degradation behavior of the passivated devices. Tracking the variation in parameters allowed us to identify the most effective passivant among the monitored ones. These are CEAI (2 mg.mL$^{-1}$), HTAB (0.7 mg.mL$^{-1}$) and both 2.5 mg.mL$^{-1}$ and 4 mg.mL$^{-1}$ for FPEAI, as they displayed similar characteristics and require additional analysis.

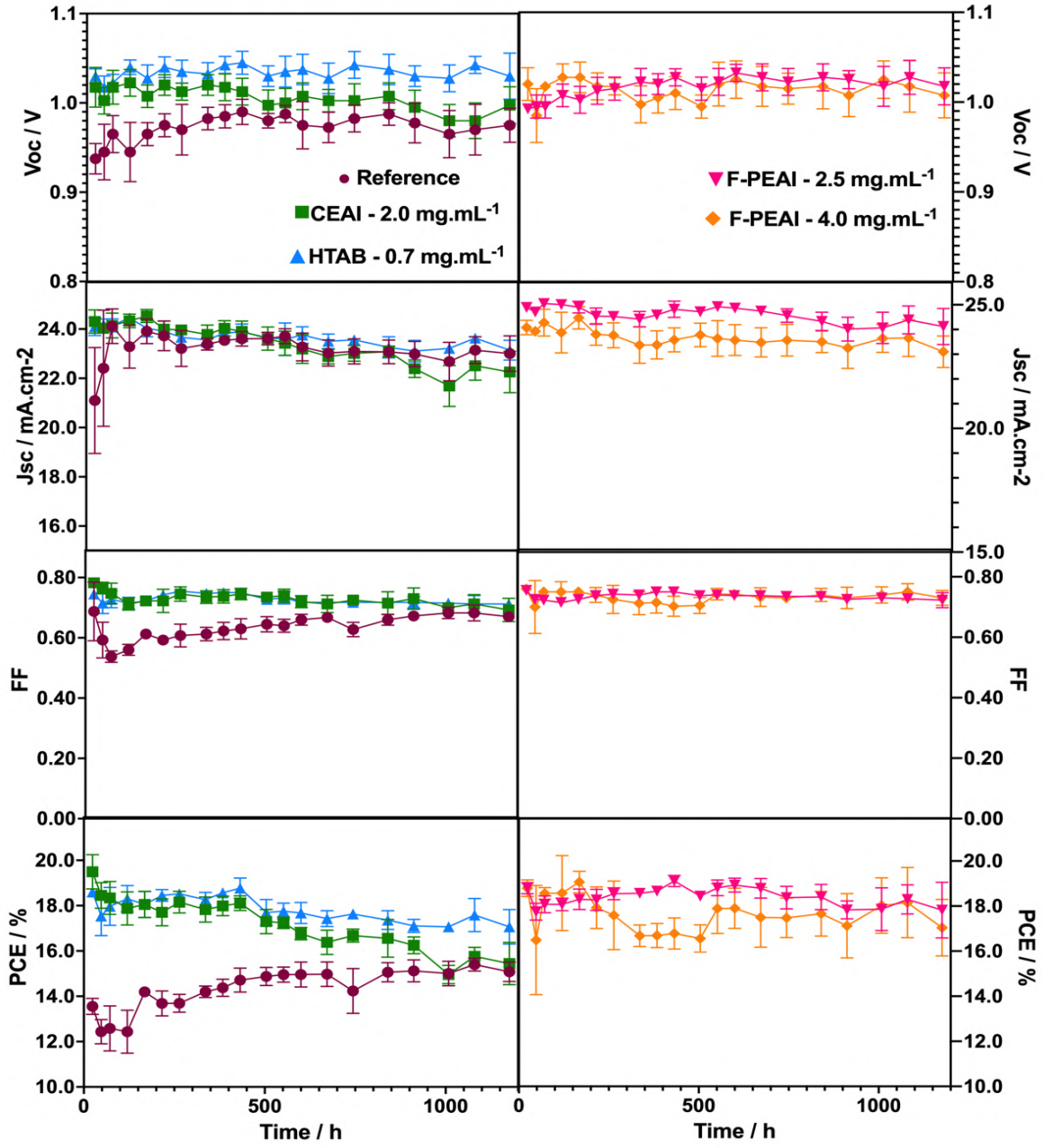


Figure 37: J-V characteristics tracked over 1000 hours for the passivated films with optimal concentration.

Across 1000 h, all passivated devices exhibit a better performance with respect to the reference. On the left panel in Figure 37, HTAB holds the highest $V_{oc}$ throughout ($\sim$1.02-1.04 V) with minimal deviations; CEAI intially at $\sim$1.02 V decreases over time to $\sim$0.99 V; the reference starts lowest ($\sim$0.93-0.97 V) and moves up initially but remains well below the passivated films. $J_{sc}$ for HTAB shows only a mild downward trend (initial- $\sim$24 mA.cm$^{-2}$ and final- $\sim$23.5 mA.cm$^{-2}$ over 1000 h's), however for CEAI the $J_{sc}$ drops by almost 2 mA.cm$^{-2}$ with respect to the starting point ($\sim$24.2 mA.cm$^{-2}$). The reference $J_{sc}$ exhibits a noisy behaviour, as it abruptly and significantly increases by $\sim$3 mA.cm$^{-2}$ initially and then creeps down gradually to $\sim$23.5 mA.cm$^{-2}$. Interestingly, this is equal to HTAB and higher than CEAI films. FF is consistently high for CEAI and HTAB ($\sim$0.72-0.76) and essentially remains invariant in time; the reference begins lower ($\sim$0.68), drops initially and improves with time to $\sim$0.7, which is close to passivated film but never exceeds their levels. Consequently, PCE for CEAI and HTAB starts around 20 and 18.7%, with CEAI being the champion among all the passivated cases, and settles near 15.4% and 17%, respectively with $\approx$80 and 92% retention, whereas the reference rises from $\sim$12-13% to $\sim$14%, then moves up to $\sim$15.2%, still remains inferior to the passivated devices. It is interesting to note that after 1000 hours, CEAI's downfall brings it almost to the Ref level. This drop can be primarily attributed to the reduction in $J_{sc}$ over time. These conclusions regarding CEAI are a direct contradiction to the findings presented in [266], where the authors have demonstrated CEAI passivated films to be efficient and operationally stable over long hours. In fact, here we see that HTAB passivated films significantly outperform CEAI films, both in efficiency and operational stability. Other research works [278] related to HTAB-passivated hybrid perovskite films with P3HT as HTM suggest that modification by HTAB molecule is an effective way to passivate the perovskite defects and facilitate the carrier transport at the perovskite/HTL interface. Although our results do point us in the same direction, at this stage in our research, we cannot provide a conclusive argument.

On the right panel, both FPEAI concentrations are notably stable. The $V_{oc}$ remains ∼1.00-1.03 V with tiny fluctuations. $J_{sc}$ is higher for 2.5 mg.mL$^{-1}$ (initial- ∼25 mA.cm$^{-2}$; champion ∼25.21 mA.cm$^{-2}$ ) than for 4.0 mg.mL$^{-1}$ (∼23-23.5 mA.cm$^{-2}$), clearly validating that higher passivant concentration increases resistance. It is noteworthy that, to the best of our knowledge this is the **highest ever** $J_{sc}$ obtained for FPEAI as passivant on $Cs_{0.05}FA_{0.85}MA_{0.10}Pb(I_{0.95}Br_{0.05})_3$ perovskite cell. FF for both sits ∼0.72-0.75 and is essentially time invariant. As a result, PCE is the most stable and highest for FPEAI 2.5 mg.mL$^{-1}$ (∼18-19% throughout the testing period), with FPEAI 4.0 mg.mL$^{-1}$ tracking just under between the range of (∼17-18%). Additional experiments and tests are being conducted to justify the trends we are observing.

In summary, FPEAI at 2.5 mg.mL$^{-1}$ is the best passivant as it delivers the highest and most stable PCE over 1000 h. It preserves the $V_{oc}$ and FF while maintaining the highest $J_{sc}$ among all the passivated devices. This is strong evidence of efficient defect passivation without introduction of a significant extraction barrier. FPEAI at 4.0 mg.mL$^{-1}$ is close but shows a small $J_{sc}$ penalty, consistent with higher thickness. HTAB achieves the highest $V_{oc}$ (for reasons still unknown to us, but based on [279] can be attributed to the improved hole extraction due to the formation of the interfacial electric dipole layer) and very steady FF (similar to FPEAI), but its long alkyl chain can hamper transport, limiting its PCE to below FPEAI. CEAI provides solid, balanced stability (good $V_{oc}$ and FF retention) but does not match FPEAI's (2.5) combination of efficiency and stability. Thus, after 1000 hours, it is evident that films with FPEAI (2.5) > FPEAI (4.0) ≥ HTAB > CEAI > Reference, for developing efficient and stable cells.

Having established the optimal concentrations for each passivant, we then fabricated a fresh batch using only the optimized compositions. In addition, cases highlighted in red in figure 35 were also included this time. For this batch, alongside the J-V characterization (recorded only on the day of fabrication), Scanning Electron Microscopy (SEM) and X-ray Diffraction (XRD) measurements were performed to analyze the morphology

and crystal structure of the prepared films. As shown in Figure 36 (d), it is evident that the overall efficiencies are lower compared to the last batch. This is primarily due to low FF, because $V_{oc}$ still remains within ∼0.98-1.01 V across the passivated samples, while the $J_{sc}$ shows either no changes or it improves. However, the general performance trend remains consistent with the previous batch, ie. the champion passivated films clearly outperform the Ref and follow the order (without FPEAI post annealing): CEAI (2.0 mg.mL$^{-1}$, 17.7%) ≥ FPEAI (2.5 mg.mL$^{-1}$, 17.67%) > HTAB (0.7 mg.mL$^{-1}$, 16.2%) > Ref (14.4%). Interestingly, upon annealing, the champion device with FPEAI 4 mg.mL$^{-1}$ (17.18%) surpassed the 2.5 mg·mL$^{-1}$ (16.33%), which is opposite to the trend observed in the un-annealed films. This suggests that annealing might have stronger impact at higher concentrations, enhancing the film quality and compensating for potential carrier transport limitations. According to [273], annealing reduces the overall performance. However, they evaluated post-annealing effects for only the best concentration. Thus with different concentrations, this behavior, remains an open question and is being further investigated.

The first step is to understand the morphology of the passivated and bare film. Figure 38 (a-f) presents the SEM top view images of the analyzed samples, allowing a direct comparison between the passivated films and the reference. The reference exhibits smaller grains with visible voids, pin-holes and low compactness, consistent with other reports [280–284]. In contrast, the FPEAI (both concentrations, annealed) and CEAI-passivated films display a more smoother and uniform surface with reduced intergrain voids, as evident in figure 38 (b,e and f). This improvement reflects the ability of the passivation molecules to modify the surface morphology by filling surface defects and improving intergrain connectivity, rather than altering the underlying perovskite bulk growth. This is also supported by the XRD patterns in Figure 38 (h, j-l). While the overall bulk diffraction features remain unchanged, enhanced diffraction peak intensities suggest improved crystallinity at or near the surface. Furthermore, additional low-angle reflections (shaded regions) are visible only in the annealed FPEAI films,

suggesting the formation of 2D phases [273]. Despite annealing, CEAI-passivated films do not exhibit such peaks, which may or may not be due to the limited resolution of the XRD setup. This is because in another study, the fabrication of CEAI based films with the same constraint on annealing time and temperature yielded a 2D phase [278].

A closer examination of the FPEAI- annealed samples (Figure 38 (d-f)) reveals subtle differences in grain uniformity, with the 4 mg.mL$^{-1}$ film appearing more homogeneous than the 2.5 mg.mL$^{-1}$ counterpart. This structural uniformity likely contributes to the slightly higher champion efficiency observed for the FPEAI (4-annealed) device. Furthermore, based on literature reports of strong interaction between the FPEAI cation and the perovskite surface, that enhances structural ordering and improves surface energy matching [285], the superior performance of FPEAI passivated films (both concentrations) can be attributed to the uniform coverage and possibly suppression of defects at the grain boundaries. For the unannealed FPEAI sample, a surface coating that possibly bridges grain boundaries appears to have been formed, creating a smoother and more continuous surface. By reducing the exposure of boundary defects, this coating is likely to suppress surface recombination, which is consistent with the higher efficiency and enhanced long-term stability observed in the first batch.

Although CEAI-passivated films show improved compactness compared to the Ref sample, small number of pinholes and voids remain visible. In contrast, the HTAB-treated films exhibit a rather distinct morphology, characterized by heterogeneity in grain size and surface coverage. Closer inspection reveals part elongated, needle [286] or flake [287]-like domains and part fused grains. The flake like domains indicate formation of low-dimensional phases, however, the XRD pattern in Figure 38 (i) shows no discernible low-angle peaks. We are investigating this further. Despite a heterogeneous morphology, HTAB passivated films exhibit a good performance overall.

In summary, all passivated films exhibit noticeable improvements in surface coverage and compactness compared to the reference sample. Additionally, small bright particulates are more prominent on the reference surface, which are likely associated

with $PbI_2$ segregations, a common feature reported in perovskite films with incomplete surface conversion [30, 272]. In contrast, FPEAI-, CEAI-, and HTAB-passivated films show a significant reduction of such features. The remaining bright contrast regions may correspond to localized crystallization or aggregation of passivant molecules. Given the semiconducting and partially insulating nature of these surface layers, local charging effects under the electron beam may further enhance contrast in SEM images [288].

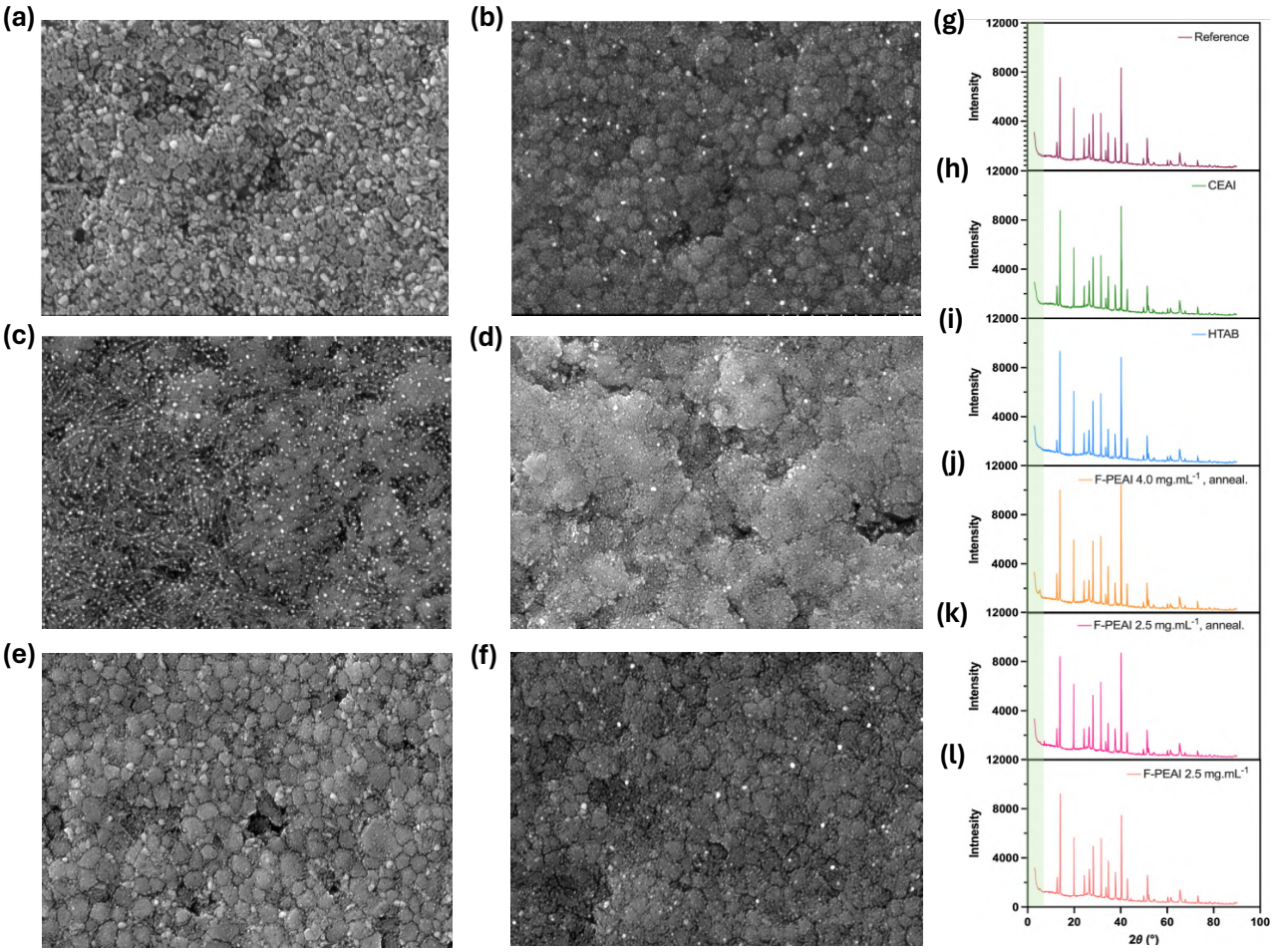


Figure 38: SEM images along with their XRD of PVK samples with different passivation layers on glass/ITO/SnO2 substrates;(a,g) Ref; (b,h) CEAI 2 mg.mL$^{-1}$; (c,i) HTAB 0.7 mg.mL$^{-1}$; (d,l) FPEAI 2.5 mmg.mL$^{-1}$; (e,k) FPEAI 2.5 mg.mL$^{-1}$ annealed and (f,j) FPEAI 4 mg.mL$^{-1}$ annealed. Scale bar in all images is equal to 300 nm.

In chapter 4, we presented our results regarding the modification of $Cs_2AgBiBr_6$ with n-butylammonium (BA) to form a 2D capping layer and its application in HTM-free perovskite solar cells with carbon electrodes. Inspired by this, using FPEAI (2.5 $mg.mL^{-1}$) as passivant on the hybrid perovskite film, instead of using spiro and gold we directly applied a carbon paste. This yielded a perovskite/passivant/Carbon configuration as opposed to perovskite/passivant/Spiro/gold. In this case also, we evaluated and tracked the performance of our carbon based cells as can be seen in figure (39) below.

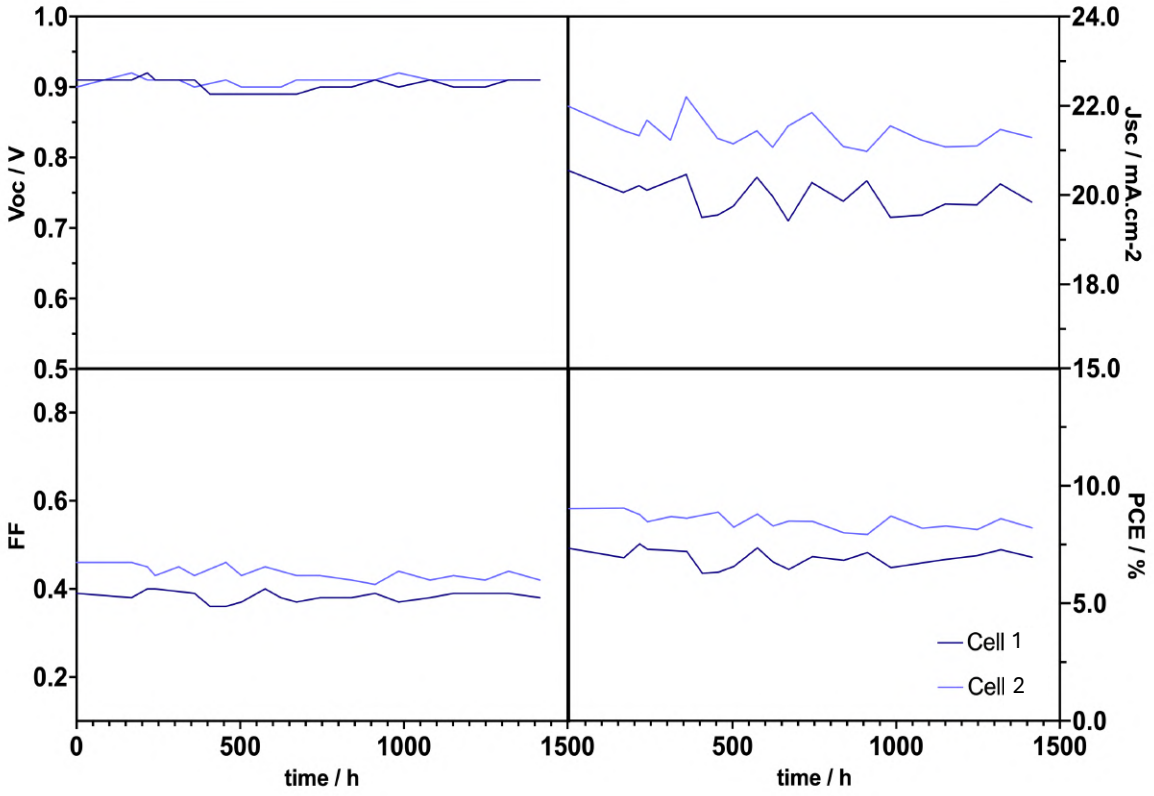


Figure 39: J-V characteristics of carbon electrode based HTM-Free cells.

It is evident that both cells exhibit remarkable operational stability over the 1500 h monitoring period, with all parameters maintaining near steady values and showing only minor fluctuations. The open-circuit voltage ($V_{oc}$) remains essentially

constant at approximately 0.90–0.92 V throughout the test duration. The short-circuit current density ($J_{sc}$) displays a moderate downward trend of less than 10%. The fill factor (FF) values remain relatively low (around 0.40–0.45) suggesting high series and low shunt resistance, but are highly stable. Overall, throughout +1000 h, $V_{oc}$ and FF remain essentially unchanged, indicating stable interfacial energetics and charge-extraction pathways in the FPEAI-passivated carbon devices. In contrast, a gradual reduction in $J_{sc}$ is observed, which points to onset long-term degradation pathways like ion accumulation at the interface, trap-state growth, and contact-related losses. All of these can lead to weaker light absorption and quenching of photogenerated carriers. As a result, of the generated carrier, fewer would be subsequently collected, contributing to the long-term loss in photocurrent. These aspects are being further investigated. Consequently, the overall power conversion efficiency (PCE) remains nearly constant in the range of 7-9 % over 1500 h, confirming robustness of the devices. The slight offset between Cell 1 and Cell 2 can be attributed to minor variations in active layer thickness or interfacial uniformity during fabrication, yet both follow nearly identical stability trends, underscoring the intrinsic stability under ambient measurement conditions.

In light of these performances, for our next steps we will dig deeper into HTM and gold free cells, not only for FPEAI but also for other passivants. Moreover all the results discussed so far are being validated by the colleagues in Porto, along with additional measurements like PL, UV-Vis, XPS etc. to better understand the interactions at the the interface. Furthermore, once these results are validated, I will perform DFT calcualtions to understand the electronic structure various interfaces.

## 7.3 Conclusion

This investigation clearly highlights the effectiveness of various passivants on governing the device performance in n-i-p structured perovskite solar cells. Among the halide based passivants explored, each of the CEAI, HTAB, and FPEAI based

films demonstrated distinct advantages and limitations. CEAI provided moderate performance enhancement and smooth morphology but exhibited long term instability. HTAB, on the other hand, induced high open-circuit voltages and effective defect suppression; however, its long alkyl chain led to reduced carrier extraction efficiency at higher concentrations, resulting in a trade-off between passivation and transport. FPEAI emerged as the most effective passivant overall, producing compact, highly crystalline films with minimal defect density and probably robust energetics, which translated into superior efficiency and operational stability. The results suggest that, it enables efficient charge transfer while suppressing recombination and by extension maybe even moisture induced degradation. The excellent performance retention of FPEAI passivated devices in the perovskite/FPEAI/carbon configuration where the conventional Spiro-OMeTAD and gold electrode were eliminated-demonstrates its potential as a multifunctional passivant for realizing HTM-free and Au-free perovskite solar cells. These findings not only highlight the critical role of interfacial passivation in achieving balanced optoelectronic and stability characteristics but also open new avenues toward scalable, cost-effective, and durable perovskite photovoltaics suited for real-world applications.

## 7.4 Thin Film Fabrication

FTO substrates (2.2 mm thick) were first brushed using a detergent aqueous solution. Subsequently, the substrates were subjected to an ultrasonic cleaning process for 15 minutes each in detergent, distilled water, acetone, and isopropanol. After drying the surface, the substrates were exposed to a UV/$O_3$ treatment for 20 minutes. First, the 35 $\times$ 45 $mm^2$ FTO substrates were preheated at 450 °C, and the $TiO_2$ blocking layer was deposited by spray pyrolysis of a precursor solution consisting of 0.4 mL of acetylacetone and 0.6 mL of titanium diisopropoxide bis(acetylacetonate) in 7 mL of anhydrous isopropanol, which was sufficient to coat an FTO surface of

about 18 × 18 $cm^2$. This layer was sintered for 45 minutes at 450 °C. A commercial $SnO_2$ dispersion in water (15 wt.%) from Solaveni was diluted with deionized water in a 1:5 ratio to achieve a 2.5 wt.% $SnO_2$ dispersion. After UV-ozone treatment of the substrates for 15 minutes, 200 $\mu$L of $SnO_2$ were deposited via spin coating at 4000 rpm for 40 s, followed by annealing at 150 °C for 30 minutes under ambient atmosphere. Next, the triple-cation perovskite precursor solution of $Cs_{0.05}FA_{0.85}MA_{0.10}Pb(I_{2.9}Br_{0.1})_3$ was prepared by mixing $PbI_2$, MABr, FAI, and CsI in a solvent mixture of DMF:DMSO in a 4:1 volume ratio. The perovskite layer was fabricated using 80 $\mu$L of the precursor solution and a two-step spin-coating procedure at 2000 rpm for 10 s and 6000 rpm for 14 s. During the second step, 200 $\mu$L of the antisolvent chlorobenzene were dropped onto the substrates, and spinning continued at 6000 rpm for an additional 6 s. The substrates were then annealed at 100 °C for 30 minutes.

Subsequently, 80 $\mu$L of the passivating agents were spin-coated at 5000 rpm for 60 s, followed by post-annealing at 100 °C in a glovebox. Next, 80 $\mu$L of a commercial Spiro-OMeTAD solution were spin-coated at 3000 rpm for 30 s in the glovebox under a nitrogen atmosphere. After cooling to room temperature, a 102 $mg\,mL^{-1}$ PTAA solution in chlorobenzene, doped with 10 $\mu$L FK-209 (40 $mg\,mL^{-1}$ in acetonitrile), 23 $\mu$L Li-TFSI (520 $mg\,mL^{-1}$ in acetonitrile), and 40 $\mu$L of t-BP, was spin-coated onto the perovskite layer at 4000 rpm for 20 s with a ramp rate of 2000 $rpm\,s^{-1}$. Finally, the substrates were completed by thermally evaporating a 60 nm Au electrode. Incase of carbon based cells, instead of spiro and gold the paste was directly applied on the passivated film. Figure 40 shows a sample of the fabricated films.

## 7.5 Film Characterization

The J-V characteristic curves of the PSCs were obtained by applying an external potential load and measuring the generated photocurrent using a Zennium workstation (Zahner Elektrik, Germany) controlled by the Thales software package (Thales

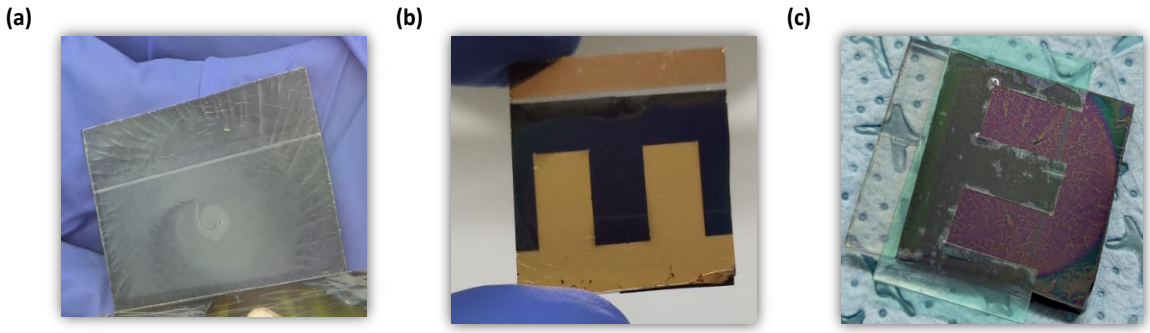


Figure 40: (a)Front side of fabricated perovskite cells with FPEAI (2.5);(b) Au electrode deposited on FPEAI (2.5) passivated cells;(c) Carbon paste applied on FPEAI (2.5) passivated cells.

XT 5.1.4). The measurements were performed under AM 1.5 G irradiation at (100) mW $cm^{-2}$ (1 sun), supplied by a solar simulator (Oriel class ABA LED simulator-MiniSol LSH 732 from Newport). The simulator was calibrated using a single-crystal Si photodiode (Newport, USA). The scan speed and voltage step used were 10 $mV\,s^{-1}$ and 20 mV, respectively. The devices were characterized immediately after their preparation, at room temperature and in ambient air. The active area of the solar cells was defined by a shadowing black mask with an aperture area of 0.126 $cm^2$. All the devices were measured with a reverse scan rate (from $V_{oc}$ to $J_{sc}$).

## 7.6 XRD and SEM analysis

Scanning electron microscopy (SEM) was performed on a SU-70 microscope (Hitachi, Japan) operated at 20 kV. Energy Dispersive X-ray Spectroscopy (EDS) using a Quantax 400 detector (Bruker, USA) coupled to the microscope was employed for chemical characterization and element mapping. X-ray diffraction (XRD) was conducted using CuK$\alpha$ radiation on an Empyrean diffractometer (Malvern Panalytical, UK). The crystalline phases were determined by performing a $2\theta$ scan in the range of 3°-90°, with a step size of 0.04° ($2\theta$) and a scan time of 195 s per step.

These measurements were performed within the scope of the project CICECO-Aveiro Institute of Materials, financed by national funds through the FCT/MCTES (PIDDAC).

# 8 Conclusions and Future

This thesis has examined how perovskite and perovskite-inspired materials behave at their interfaces with different charge transport layers, using a combination of density functional theory (DFT) and experiments. Although the systems studied vary in composition and structure, the results clearly highlight the important role of atomic scale properties of interfaces in governing charge extraction, recombination, and long term stability etc. and therefore play a decisive role in the overall performance of perovskite photovoltaic devices.

In Chapter 4, we investigated $Cs_2AgBiBr_6$ double perovskites modified by n-butylammonium bromide (BABr), forming a 2D/3D heterostructure. Experimental outcomes of this modification yielded improved $J_{sc}$, $V_{oc}$, fill factor, and efficiency for BABr concentrations up to 0.05 M, due to more favorable valence-band alignment with the perovskite. Our DFT calculations clarified why an optimal concentration exists. We understood that a very thin 2D layer does not contribute enough to the VBM to facilitate hole extraction, whereas thicker layers attract both holes and electrons to the same region, promoting recombination and lowering $J_{sc}$. Furthermore, defect calculations showed that the 2D capping layer acts less like a traditional passivant i.e. it prevents defects from accumulating at the interface rather than neutralizing them. In contrast, the conventional Spiro-OMeTAD drew these defects toward the interface. Together, these results underlined the importance of controlling 2D layer thickness in double-perovskite devices and demonstrate the viability of low-cost, HTM-free, carbon based architectures.

Building on this foundation, we extended our investigation to another promising lead-free material: bismuth oxyiodide (BiOI), in chapter 5. Our atomistic level analysis of the stable [110]BiOI/[010]ZnO heterojunction revealed that interface formation leads to: i)the breaking of terminal Bi-I bonds that aids ii) Bi-O-Zn bonding and iii) the formation of I-O bond. Such atomic rearrangements introduced trap like states

dominated by I and O, roughly 1 eV below the CBM. With focus on photo-electron in the CB, tracking of the local frontier-orbital energies showed an energy minimum at the interface that can both assist electron transfer from bulk of the absorber to the interface and trap electrons. Moreover, the potential energy profile also revealed that there exists a 0.44 eV barrier, although it is spatially limited to only $\sim$ 0.2 nm. This adds another level of difficulty for electron extraction, to the pre-existing type 1 band alignment where BiOI's band gap is fully contained within ZnOs' band gap. These insights likely explain the persistent efficiency bottlenecks in BiOI/ZnO devices and identify the atomistic origins of their limited charge extraction behaviour.

In chapter 6, we examined how different surface orientations of hybrid perovskites interact with the widely used hole transport material (HTM), Spiro-OMeTAD and a recently developed T2. The results established a clear connection between structural bonding and electronic coupling: T2 consistently formed stronger Pb-S interactions and showed greater hybridization near the VBM than Spiro for all the surfaces. Among the studied cases, the (100) facet supported the most favourable hole-extraction characteristics, followed by (102), while the (111) surface exhibited intrinsically weak interactions with both HTMs. These results emphasised that facet orientation plays a central role in determining charge transfer efficiency in mixed-halide perovskites.

Finally, chapter 7 compared three halide-based passivants i.e. CEAI, HTAB, and FPEAI in hybrid perovskite solar cells. Each passivant offered different strengths: CEAI exhibited high effciency but lacked stability, HTAB delivered high $V_{\mathrm{oc}}$ but limited charge extraction at high concentration, and FPEAI showed the best overall balance of surface coverage, possible alignment and defect passivation, highest long term efficiency and stability. Notably, perovskite/FPEAI/carbon devices maintained high performance even without Spiro-OMeTAD or gold electrodes, highlighting FPEAI's potential as a versatile passivant for low-cost, HTM-free and Au-free devices.

Overall, the work presented in this thesis demonstrates how interfacial structure, defect behaviour, facet orientation, and passivation chemistry collectively determine

the performance of perovskite based photovoltaic systems. The insights gained here provide practical guidelines and conceptual tools for designing more efficient, stable, and sustainable perovskite solar cells.

## 8.1 Future Outlook

Looking ahead, the outcomes of this thesis highlight several promising pathways for advancing perovskite and perovskite-inspired photovoltaics through targeted interfacial engineering. In the case of $Cs_2AgBiBr_6$ double perovskite, our results show that 3D/2D architectures can substantially improve hole selectivity and suppress defect accumulation; however, these advantages must be balanced against the slower charge extraction that emerges once the 2D capping layer exceeds a critical thickness. This suggests that future efforts should focus on designing 2D layers that provide strong defect suppression while preserving fast carrier transport. Moreover, in contrast to traditional lead-halide perovskites, where facet engineering is well established as a strategy for enhancing stability and efficiency, such approaches remain largely unexplored for $Cs_2AgBiBr_6$ and offer an important direction for further study.

For BiOI based photovoltaic systems, the discovery of interfacial bond rearrangements and deep electron trap states at the BiOI/ZnO heterojunction underscores the need for more controlled facet engineering and interlayer chemistry. Experimental efforts could therefore prioritize facet selective crystallization and explore alternative ETLs that can form intimate contact with the flake like morphology of BiOI while supporting higher photoconversion efficiencies.

For lead-halide perovskites, the strong dependence of hole extraction on both the exposed surface and the identity of the HTM indicates that future HTMs should be co-designed with the perovskite's surface in mind. Especially, since the experiments suggest that (111) oriented perovskite films can exhibit superior stability compared

to conventional (100) surfaces, while our DFT results show that (111) is intrinsically unfavorable for rapid and efficient hole extraction, regardless of the HTM involved. This highlights the opportunity for developing facet aware HTMs tailored to specific surface terminations.

Finally, the strong performance of FPEAI passivated perovskite devices employing carbon paste, as demonstrated in this thesis, indicates a broader opportunity for sustainable and low cost device architectures. Given that only a single passivant-carbon combination was explored here, future studies should investigate a wider range of passivants (including those evaluated earlier) alongside systematic improvements in carbon based electrodes, particularly their contact with passivation layers. Progress in both interfacial passivation and carbon electrode engineering could pave the way for stable, efficient, and truly low-cost perovskite photovoltaics. In addition to chemical passivation, controlling the crystallographic orientation of the perovskite film, can further influence interfacial energetics, defect exposure, and charge-transport pathways, offering an additional lever for optimizing HTM-free and Au-free device performance.

Together, these research directions reflect a growing shift toward an interface aware approach to photovoltaic design, in which performance, stability, and sustainability are governed not only by bulk materials but by the precise control of atomic scale interactions at buried junctions. Advancing this vision will accelerate the deployment of perovskite technologies in cost sensitive and emerging markets, especially for indoor and low illumination energy harvesting applications.

# References


[1] M. A. Green, E. D. Dunlop, D. H. Levi, J. Hohl-Ebinger, M. Yoshita, and A. W. Y. Ho-Baillie. Solar cell efficiency tables (version 60). *Progress in Photovoltaics: Research and Applications*, 30(1):3–12, 2022.

[2] Sang-Won Lee, Seongtak Kim, Soohyun Bae, Kyungjin Cho, Taewon Chung, Jae-Keun Hwang, Inseol Song, Wonkyu Lee, Sungeun Park, Jaebong Jung, Jihun Chun, Yoon Jung Lee, Yeon Ji Moon, Hae-Seok Lee, Donghwan Kim, Chan Bin Mo, and Yoonmook Kang. Enhanced uv stability of perovskite solar cells with a sro interlayer. *Organic Electronics*, 63:343 – 348, 2018. Cited by: 33.

[3] National Renewable Energy Laboratory (NREL). Best research-cell efficiency chart, 2024. `https://www.nrel.gov/pv/cell-efficiency.html`.

[4] Akihiro Kojima, Kenjiro Teshima, Yasuo Shirai, and Tsutomu Miyasaka. Organometal halide perovskites as visible-light sensitizers for photovoltaic cells. *Journal of the American Chemical Society*, 131(17):6050–6051, 2009.

[5] Henry J. Snaith. Present status and future prospects of perovskite photovoltaics. *Nature Materials*, 17:372–376, 2018.

[6] A review on perovskite materials for photovoltaic applications. *Next Materials*, 7:100494, 2025.

[7] G. Niu, X. Guo, and L. Wang. Review of recent progress in chemical stability of perovskite solar cells. *Journal of Materials Chemistry A*, 3(17):8970–8980, 2015.

[8] K. Domanski, J. P. Correa-Baena, N. Mine, M. K. Nazeeruddin, M. Grätzel, W. Tress, and A. Hagfeldt. Migration of cations induces reversible performance losses over day/night cycling in perovskite solar cells. *Energy & Environmental Science*, 10(2):604–613, 2017.

[9] N. J. Jeon, J. H. Noh, W. S. Yang, Y. C. Kim, S. Ryu, J. Seo, and S. I. Seok. Compositional engineering of perovskite materials for high-performance solar cells. *Nature*, 517(7535):476–480, 2015.

[10] M. Saliba, T. Matsui, K. Domanski, J. Y. Seo, A. Ummadisingu, S. M. Zakeeruddin, J. P. Correa-Baena, W. Tress, A. Abate, A. Hagfeldt, and M. Grätzel. Incorporation of rubidium cations into perovskite solar cells improves photovoltaic performance. *Science*, 354(6309):206–209, 2016.

[11] Z. Zheng, G. Wu, Y. Duan, H. Li, Q. Wang, Y. Tang, and Y. Liu. Development of formamidinium lead iodide-based perovskite solar cells:efficiency and stability. *Chemical Science*, 13(12):3565–3576, 2022.

[12] M. Hu S.-U. Lee S. I. Seok L. Chen, J. W. Yoo. Intrinsic phase stability and inherent bandgap of formamidinium lead triiodide (fapbi) perovskites. *Angewandte Chemie International Edition*, page e202212700, 2022.

[13] Qingbo Wei, Wei Zi, Zhou Yang, and Dong Yang. Photoelectric performance and stability comparison of mapbi3 and fapbi3 perovskite solar cells. *Solar Energy*, 174:933–939, 2018.

[14] Constantinos C. Stoumpos and Mercouri G. Kanatzidis. The renaissance of halide perovskites and their evolution as emerging semiconductors. *Accounts of Chemical Research*, 48(10):2791–2802, 2015.

[15] A. Poglitsch and D. Weber. Dynamic disorder in methylammoniumtrihalogenoplumbates (ii) observed by millimeter-wave spectroscopy. *The Journal of Chemical Physics*, 87(11):6373–6378, 1987.

[16] Fusheng Ma, Jiangwei Li, Wenzhe Li, Na Lin, Liduo Wang, and Juan Qiao. Stable / phase junction of formamidinium lead iodide perovskites for enhanced near-infrared emission. *Chemical Science*, 8(1):800–805, 2017.

[17] T. Chen et al. Inhibition of defect-induced -to- phase transition for efficient and stable formamidinium perovskite solar cells. *Nature Communications*, 14, 2023.

[18] Chenyi Yi, Jingshan Luo, Simone Meloni, Ariadni Boziki, Negar Ashari-Astani, Carole Grätzel, Shaik M. Zakeeruddin, Ursula Röthlisberger, and Michael Grätzel. Entropic stabilization of mixed a-cation abx3 metal halide perovskites for high performance perovskite solar cells. *Energy Environ. Sci.*, 9:656–662, 2016.

[19] W. S. Yang, B. W. Park, E. H. Jung, N. J. Jeon, Y. C. Kim, D. U. Lee, S. S. Shin, J. Seo, E. K. Kim, J. H. Noh, and S. I. Seok. Iodide management in formamidinium-lead-halide–based perovskite layers for efficient solar cells. *Science*, 356(6345):1376–1379, 2017.

[20] A review on perovskite solar cells: Evolution of architecture, fabrication techniques, commercialization issues and status. *Solar Energy*, 198:665–688, 2020.

[21] Xianyuan Li, Feng Zhang, Hui He, Jonathan J. Berry, Kai Zhu, and Tielong Xu. Guanine-assisted defect passivation for high-efficiency n–i–p planar perovskite solar cells. *Polymers Flexible Electronics*, 4(2):123–130, 2025. Reports a certified PCE of 26.21 % for n–i–p single-junction PSCs.

[22] Zheng et al. Towards 26% efficiency in inverted perovskite solar cells via interfacial flipped band bending and suppressed deep-level traps. *Energy Environmental Science*, 17(5):3304–3312, 2024.

[23] Hui Zhang and Nam-Gyu Park. Progress and issues in p-i-n type perovskite solar cells. *DeCarbon*, 3:100025, 2024.

[24] Sawanta S. Mali and Chang Kook Hong. p-i-n/n-i-p type planar hybrid structure of highly efficient perovskite solar cells towards improved air stability: synthetic strategies and the role of p-type hole transport layer (htl) and n-type electron transport layer (etl) metal oxides. *Nanoscale*, 8:10528–10540, 2016.

[25] Martin Stolterfoht, Pietro Caprioglio, Christian M. Wolff, José A. Márquez, Joleik Nordmann, Shanshan Zhang, Daniel Rothhardt, Ulrich Hörmann, Yohai Amir, Alex Redinger, Lukas Kegelmann, Fengshuo Zu, Steve Albrecht, Norbert Koch, Thomas Kirchartz, Michael Saliba, Thomas Unold, and Dieter Neher. The impact of energy alignment and interfacial recombination on the internal and external open-circuit voltage of perovskite solar cells. *Energy amp; Environmental Science*, 12(9):2778–2788, 2019.

[26] Tanzi Ahmed Chowdhury, Md. Arafat Bin Zafar, Md. Sajjad-Ul Islam, M. Shahinuzzaman, Mohammad Aminul Islam, and Mayeen Uddin Khandaker. Stability of perovskite solar cells: issues and prospects. *RSC Adv.*, 13:1787–1810, 2023.

[27] Faouzia Tayari, Silvia Soreto Teixeira, Manuel Pedro F. Graca, and Kais Iben Nassar. A comprehensive review of recent advances in perovskite materials: Electrical, dielectric, and magnetic properties. *Inorganics*, 13(3), 2025.

[28] Han-Song Wu, Bayu Tri Murti, Jitendra Singh, Po-Kang Yang, and Meng-Lin Tsai. Prospects of metal-free perovskites for piezoelectric applications. *Advanced Science*, 9(12):2104703, 2022.

[29] Wolfgang Tress. Metal halide perovskites as mixed electronic–ionic conductors: Challenges and opportunities—from hysteresis to memristivity. *Journal of Physical Chemistry Letters*, 8(13):3106–3114, 2017.

[30] Giulia Grancini and Mohammad Khaja Nazeeruddin. Dimensional tailoring of hybrid perovskites for photovoltaics. *Nature Reviews Materials*, 4:4–22, 2019.

[31] Juan-Pablo Correa-Baena, Antonio Abate, Michael Saliba, Wolfgang Tress, Timothy J. Jesper Jacobsson, Michael Grätzel, and Anders Hagfeldt. The rapid evolution of highly efficient perovskite solar cells. *Energy  Environmental Science*, 10(3):710–727, 2017.

[32] Kim and Nam-Gyu Park. High-efficiency perovskite solar cells. *Chemical Reviews*, 120(15):7867–7918, 2020.

[33] George G. Njema, Joshua K. Kibet, and Silas M. Ngari. A review of interface engineering characteristics for high performance perovskite solar cells. *Measurement: Energy*, 2:100005, 2024.

[34] S. Mazumdar et al. Stability of perovskite solar cells: degradation mechanism and mitigation strategies. *Electronics*, 10, 2021.

[35] Martin Stolterfoht, Pietro Caprioglio, Christian M. Wolff, José A. Márquez, Joleik Nordmann, Shanshan Zhang, Daniel Rothhardt, Ulrich Hörmann, Alex Redinger, Lukas Kegelmann, Steve Albrecht, Thomas Kirchartz, Michael Saliba, Thomas Unold, and Dieter Neher. The perovskite/transport layer interfaces dominate non-radiative recombination in efficient perovskite solar cells. *Energy Environmental Science*, 11(10):3380–3393, 2018.

[36] Kevin A. Bush, Axel F. Palmstrom, Zhenhua J. Yu, Mathieu Boccard, Ratul Cheacharoen, Jonathan P. Mailoa, Daniel P. McMeekin, Robert L. Z. Hoye, Colin D. Bailie, Tomas Leijtens, Stacey F. Bent, and Michael D. McGehee. 23.6%-efficient monolithic perovskite/silicon tandem solar cells with improved stability. *Nature Energy*, 3:847–854, 2018.

[37] Fabian Schmitz, Ribhu Bhatia, Julian Burkhart, Pascal Schweitzer, Marco Allione, Jaime Gallego, Piotr Piotrowski, Jakub Cajzl, Piotr Paszke, Gour Mohan Das, Dorota A. Pawlak, Federico Bella, Derck Schlettwein, Francesco Lamberti, Simone Meloni, and Teresa Gatti. Improved hole extraction and band alignment via interface modification in hole transport material-free ag/bi double perovskite solar cells. *Solar RRL*, 8(6):2300965.

[38] Jiandong Dou, Zheng Wang, and et al. Interfacial engineering for improved

stability of flexible perovskite solar cells. *Energy Materials Advances*, 2022:0002, 2022.

[39] DoHoon Kim et al. Advanced interface engineering for perovskite solar cells:the way to ensure efficiency and stability. *Accounts of Materials Research*, 6(1):56–68, 2025.

[40] Chufeng Qiu, Yan Wu, Jiaxing Song, Wentao Wang, and Zaifang Li. Efficient planar perovskite solar cells with zno electron transport layer. *Coatings*, 12(12), 2022.

[41] Aslihan Babayigit, Anitha Ethirajan, Michael Muller, and Bert Conings. Toxicity of organometal halide perovskite solar cells. *Nature Materials*, 15(3):247–251, 2016.

[42] Fabian Schmitz, Ribhu Bhatia, Francesco Lamberti, Simone Meloni, and Teresa Gatti. Heavy pnictogens-based perovskite-inspired materials: Sustainable light-harvesters for indoor photovoltaics. *APL Energy*, 1(2):021502, 08 2023.

[43] V. K. Ravi, B. Phuyal, M. Chhetri, P. Sharma, J. Shakya, R. Koju, S. Karki, A. Dunbar, J. M. Kadro, M. K. Nazeeruddin, M. Grätzel, and E. Alarousu. Don't let the lead out: New material chemistry approaches for toward lead-free perovskite solar cells. *ACS Omega*, 5(32):20796–20827, 2020.

[44] P. Wu, Y. Cheng, J. Zhang, R. Zhang, and J. Wang. Preventing lead leakage for perovskite solar cells: Strategies and outlook. *Solar Energy Materials  Solar Cells*, 250:112114, 2022.

[45] Joseph J. Berry. Perovskite photovoltaics: The path to a printable terawatt-scale thin-film solar technology. *ACS Energy Letters*, 2(7):1660–1662, 2017.

[46] Lucas Wagner, Vincent Goehaut, Michael MacDonald, Jürgen Feldmann, Stefan Bögner, and et al. The resource demands of multi-terawatt-scale perovskite photovoltaics. *Joule*, 8(5):1005–1022, 2024.

[47] Peng Zhu, Zhiwei Chen, Kang Yu, and et al. Toward the commercialization of perovskite solar modules. *Advanced Materials*, 36(2):2307357, 2024.

[48] Samuel D. Stranks, Giles E. Eperon, Giulia Grancini, Christiana Menelaou, Marcelo J. P. Alcocer, Thomas Leijtens, Laura M. Herz, Annamaria Petrozza, and Henry J. Snaith. Electron-hole diffusion lengths exceeding 1 micrometer in an organometal trihalide perovskite absorber. *Science*, 342(6156):341–344, 2013.

[49] M. A. Green. Solar cell fill factors: General graph and empirical expressions. *Solid-State Electronics*, 24(8):788–789, 1982.

[50] Nakita K. Noel, Samuel D. Stranks, Antonio Abate, Christian Wehrenfennig, Salvatore Guarnera, Amir A. Haghighirad, Aditya Sadhanala, Giles E. Eperon, Shrayesh K. Pathak, Michael B. Johnston, Alessia Petrozza, Laura M. Herz, and Henry J. Snaith. Lead-free organic–inorganic tin halide perovskites for photovoltaic applications. *Energy  Environmental Science*, 7(9):3061–3068, 2014.

[51] Singh. A et al. Photovoltaic performance of vapor-assisted solution-processed layer polymorph of cs3sb2i9. *ACS Applied Materials  Interfaces*, 2018.

[52] Marina R. Filip and Feliciano Giustino. Computational screening of homovalent lead substitution in organic–inorganic halide perovskites. *The Journal of Physical Chemistry C*, 120(1):166–173, 2016.

[53] Liqun Ye, Lihong Tian, Tianyou Peng, and Ling Zan. Synthesis of highly symmetrical bioi single-crystal nanosheets and their 001 facet-dependent photoactivity. *J. Mater. Chem.*, 21:12479–12484, 2011.

[54] Tomas Leijtens, Rohit Prasanna, Aryeh Gold-Parker, Michael F. Toney, and Michael D. McGehee. Mechanism of tin oxidation and stabilization by lead substitution in tin halide perovskites. *ACS Energy Letters*, 2(9):2159–2165, 2017.

[55] Adam H. Slavney, Tin Hu, Aaron M. Lindenberg, and Hemamala I. Karunadasa. A bismuth-halide double perovskite with long carrier recombination lifetime for photovoltaic applications. *Journal of the American Chemical Society*, 138(7):2138–2141, 2016.

[56] Jorge Pascual, Giuseppe Nasti, Mahmoud H. Aldamasy, Joel A. Smith, Marion Flatken, Silver-Hamill Turren-Cruz, Meng Li, André Dallmann, Roberto Avolio, and Antonio Abate. Origin of sn(ii) oxidation in tin halide perovskites. *Materials Advances*, 1:1066–1070, 2020.

[57] Aryeh Gold-Parker Michael F. Toney Tomas Leijtens, Rohit Prasanna and Michael D. McGehee. Mechanism of tin oxidation and stabilization by lead substitution in tin halide perovskites. *ACS Energy Letters*, 2(9):2159–2165, 2017.

[58] W. Tang, E. Sanville, and G. Henkelman. A grid-based bader analysis algorithm without lattice bias. *Journal of Physics: Condensed Matter*, 21(8):084204, 2009.

[59] Feng Gao Hongwei Lei, David Hardy. Lead-free halide double perovskites: Fundamentals, applications adn perspectives. *Advanced Functional Materials*, 2021.

[60] Georgios Volonakis, Amir-Amir Haghighirad, Rebecca L. Milot, Henry J. Snaith, Michael B. Johnston, Laura M. Herz, and Feliciano Giustino. Cs2inagcl6: A lead-free halide double perovskite with direct band gap. *The Journal of Physical Chemistry Letters*, 8(4):772–778, 2017.

[61] Yi-Teng Huang, Seán R Kavanagh, David O Scanlon, Aron Walsh, and Robert L Z Hoye. Perovskite-inspired materials for photovoltaics and beyond—from design to devices. *Nanotechnology*, 32(13):132004, jan 2021.

[62] Robert L. Z. Hoye, Lana C. Lee, Rachel C. Kurchin, Tahmida N. Huq, Kelvin H. L. Zhang, Melany Sponseller, Lea Nienhaus, Riley E. Brandt, Joel Jean, James Alexander Polizzotti, Ahmed Kursumović, Moungi G. Bawendi, Vladimir Bulović, Vladan Stevanović, Tonio Buonassisi, and Judith L. MacManus-Driscoll.

Strongly enhanced photovoltaic performance and defect physics of air-stable bismuth oxyiodide (bioi). *Advanced Materials*, 29(36):1702176, 2017.

[63] David J. Griffiths and Darrell F. Schroeter. *Introduction to Quantum Mechanics*. Cambridge University Press, 3rd edition, 2018.

[64] P. A. M. Dirac. Quantum mechanics of many-electron systems. *Proceedings of the Royal Society A*, 123(792):714–733, 1929.

[65] M. Born and J. R. Oppenheimer. Zur quantentheorie der molekeln. *Annalen der Physik*, 389(20):457–484, 1927.

[66] P. Hohenberg and W. Kohn. Inhomogeneous electron gas. *Physical Review*, 136(3B):B864–B871, 1964.

[67] W. Kohn and L. J. Sham. Self-consistent equations including exchange and correlation effects. *Physical Review*, 140(4A):A1133–A1138, 1965.

[68] R. O. Jones. Density functional theory: Its origins, rise to prominence, and future. *Reviews of Modern Physics*, 87(3):897–923, 2015.

[69] Robert G. Parr and Weitao Yang. *Density-Functional Theory of Atoms and Molecules*. Oxford University Press, 1995.

[70] Richard M. Martin. *Electronic Structure: Basic Theory and Practical Methods*. Cambridge University Press, Cambridge, 2004. Defines the electrostatic potential in DFT and methods for potential alignment.

[71] J. P. Perdew, K. Burke, and M. Ernzerhof. Generalized gradient approximation made simple. *Physical Review Letters*, 77(18):3865–3868, 1996.

[72] A. D. Becke. Density-functional exchange-energy approximation with correct asymptotic behavior. *Physical Review A*, 38(6):3098–3100, 1988.

[73] J. P. Perdew, A. Ruzsinszky, G. I. Csonka, O. A. Vydrov, G. E. Scuseria, L. A. Constantin, X. Zhou, and K. Burke. Restoring the density-gradient expansion for exchange in solids and surfaces. *Physical Review Letters*, 100(13):136406, 2008.

[74] B. Hammer, L. B. Hansen, and J. K. Nørskov. Improved adsorption energetics within density-functional theory using revised perdew-burke-ernzerhof functionals. *Physical Review B*, 59(11):7413–7421, 1999.

[75] J. Heyd, G. E. Scuseria, and M. Ernzerhof. Hybrid functionals based on a screened coulomb potential. *The Journal of Chemical Physics*, 118(18):8207–8215, 2003.

[76] J. Heyd, G. E. Scuseria, and M. Ernzerhof. Erratum: "hybrid functionals based on a screened coulomb potential" [j. chem. phys. 118, 8207 (2003)]. *The Journal of Chemical Physics*, 124(21):219906, 2006.

[77] Peter E. Blöchl. Projector augmented-wave method. *Physical Review B*, 50(24):17953–17979, 1994.

[78] Hendrik J. Monkhorst and James D. Pack. Special points for brillouin-zone integrations. *Phys. Rev. B*, 13:5188–5192, Jun 1976.

[79] V. Wang, N. Xu, J.-C. Liu, G. Tang, and W.-T. Geng. Vaspkit: A pre- and post-processing program for the VASP code. *Computer Physics Communications*, 267:108033, 2021.

[80] D. R. Hamann, M. Schlüter, and C. Chiang. Norm-conserving pseudopotentials. *Physical Review Letters*, 43(20):1494–1497, 1979.

[81] Georg Kresse and Daniel Joubert. From ultrasoft pseudopotentials to the projector augmented-wave method. *Physical Review B*, 59(3):1758–1775, 1999.

[82] David Vanderbilt. Soft self-consistent pseudopotentials in a generalized eigenvalue formalism. *Physical Review B*, 41(11):7892–7895, 1990.

[83] John P. Perdew and Alex Zunger. Self-interaction correction to density-functional approximations for many-electron systems. *Physical Review B*, 23(10):5048–5079, 1981.

[84] Aron J. Cohen, Paula Mori-Sánchez, and Weitao Yang. Insights into current limitations of density functional theory. *Science*, 321(5890):792–794, 2008.

[85] Paula Mori-Sánchez, Aron J. Cohen, and Weitao Yang. Localization and delocalization errors in density functional theory. *Physical Review Letters*, 100:146401, 2008.

[86] Max Dion, Henry Rydberg, Elsebeth Schröder, David C. Langreth, and Bengt I. Lundqvist. Van der waals density functional for general geometries. *Physical Review Letters*, 92(24):246401, 2004.

[87] E. Heifets and R. I. Eglitis. Semi-empirical simulations of surface relaxation for $abo_3$ perovskites: surface rumpling and induced dipole moments. *Surface Science*, 450:7–20, 2000.

[88] V. I. Anisimov, Jan Zaanen, and O. K. Andersen. Band theory and mott insulators: Hubbard u instead of stoner i. *Physical Review B*, 44(3):943–954, 1991.

[89] Stefan Grimme, Stephan Ehrlich, and Lars Goerigk. Effect of the damping function in dispersion corrected density functional theory. *Journal of Computational Chemistry*, 32(7):1456–1465, 2011.

[90] Alexandre Tkatchenko and Matthias Scheffler. Accurate molecular van der waals interactions from ground-state electron density and free-atom reference data. *Physical Review Letters*, 102(7):073005, 2009.

[91] Stefan Grimme, Jens Antony, Stephan Ehrlich, and Helge Krieg. A consistent and accurate *ab initio* parametrization of density functional dispersion correction

(dft-d) for the 94 elements h-pu. *Journal of Chemical Physics*, 132(15):154104, 2010.

[92] Jiří Klimeš, David R. Bowler, and Angelos Michaelides. Chemical accuracy for the van der waals density functional. *Journal of Physics: Condensed Matter*, 22(2):022201, 2010.

[93] Jiří Klimeš, David R. Bowler, and Angelos Michaelides. Van der waals density functionals applied to solids. *Physical Review B*, 83(19):195131, 2011.

[94] Jun Haruyama, Kenjiya Kato, Kenji Tanaka, Shohei Yamashita, and Shintaro Tsuneyuki. First-principles study of electronic structures and dielectric properties of organic–inorganic hybrid interfaces: Importance of van der waals interactions. *Journal of Physical Chemistry C*, 121(40):21530–21538, 2017.

[95] Stefan Grimme. Semiempirical gga-type density functional constructed with a long-range dispersion correction. *Journal of Computational Chemistry*, 27(15):1787–1799, 2006.

[96] VASP Software GmbH. Vasp wiki - vienna Ab initio simulation package. `https://www.vasp.at/wiki/`. Accessed: Month Year.

[97] S. L. Dudarev, G. A. Botton, S. Y. Savrasov, C. J. Humphreys, and A. P. Sutton. Electron-energy-loss spectra and the structural stability of nickel oxide: An lsda+u study. *Physical Review B*, 57(3):1505–1509, 1998.

[98] VASP Schemes. Vasp wiki - vienna Ab initio simulation package. `https://www.vasp.at/wiki/Structure_optimization#References`. Accessed: Month Year.

[99] C. G. Broyden. A class of methods for solving nonlinear simultaneous equations. *Mathematics of Computation*, 19:577–593, 1965.

[100] Péter Pulay. Convergence acceleration of iterative sequences. the case of scf iteration. *Chemical Physics Letters*, 73(2):393–398, 1980.

[101] R. Fletcher and C. M. Reeves. Function minimization by conjugate gradients. *The Computer Journal*, 7:149–154, 1964.

[102] G. Kresse and J. Furthmüller. Efficient iterative schemes for *ab initio* total-energy calculations using a plane-wave basis set. *Physical Review B*, 54:11169–11186, 1996.

[103] Augustin Cauchy. Méthode générale pour la résolution des systèmes d'équations simultanées. *Comp. Rend. Sci. Paris*, 25:536–538, 1847.

[104] Jorge Nocedal and Stephen J. Wright. *Numerical Optimization*. Springer, 2nd edition, 2006.

[105] E. Polak and G. Ribiere. Note sur la convergence de methodes de directions conjuguees. *ESAIM: Mathematical Modelling and Numerical Analysis*, 3:35–43, 1969.

[106] Ernest R. Davidson. The iterative calculation of a few of the lowest eigenvalues and corresponding eigenvectors of large real-symmetric matrices. *Journal of Computational Physics*, 17:87–94, 1975.

[107] A. D. Becke and K. E. Edgecombe. A simple measure of electron localization in atomic and molecular systems. *The Journal of Chemical Physics*, 92(9):5397–5403, 05 1990.

[108] Konstantinos Koumpouras and J Andreas Larsson. Distinguishing between chemical bonding and physical binding using electron localization function (elf). *Journal of Physics: Condensed Matter*, 32(31):315502, may 2020.

[109] M. Saghayezhian et al. Rumpling and enhanced covalency at the $srtio_3(001)$ surface. *Journal of Physical Chemistry C*, 122:25568–25574, 2018.

[110] H. J. Sung et al. Surface reconstruction and band alignment of nonmetallic perovskites: Role of tolerance-factor dependent surface rumpling. *Physical Review Materials*, 4:044606, 2020.

[111] Adriana Pecoraro, Francesca Fasulo, Michele Pavone, and Ana B. Muñoz-García. First-principles study of interfacial features and charge dynamics between spiromeotad and photoactive lead halide perovskites. *Chem. Commun.*, 59:5055–5058, 2023.

[112] Q. Li et al. Compositional effect on water adsorption on metal halide perovskites. *Journal of Materials Chemistry A*, 9:19820–19828, 2021. Reports adsorption distances and energies of water molecules on perovskite surfaces.

[113] M.P. Bahlke, M. Karolak, and C. Herrmann. The interplay between strong correlation and adsorption distances. *arXiv*, page 1710.07349, 2017. Examines how adsorption distances vary with correlation, including shifts of 0.08–0.12 Å.

[114] Luiz A. Ribeiro Júnior, Raphael M. Tromer, Ramiro M. dos Santos, and Douglas S. Galvão. On the adsorption mechanism of caffeine on mapbi$_3$ perovskite surfaces: A combined umc–dft study. *arXiv*, page arXiv:2008.02084, 2020. Adsorption distance  2.0 Å; adsorption energy –0.3 eV.

[115] Z. Wu et al. Highly efficient perovskite solar cells enabled by multiple-site binding passivators. *Advanced Energy Materials*, 10(19):1903696, 2020.

[116] L. Li et al. Fully chemical interface engineering for statically and dynamically stable perovskite solar cells. *Nature Communications*, 16, 2025.

[117] A. H. Proppe et al. Multication perovskite 2d/3d interfaces form via progressive evolution of binding energy at the interface. *Nature Communications*, 12, 2021.

[118] J. Hidalgo et al. Synergistic role of water and oxygen leads to degradation of halide perovskites. *Journal of the American Chemical Society*, 145:4298–4307, 2023.

[119] N. W. Ashcroft and N. D. Mermin. *Solid State Physics*. Holt, Rinehart and Winston, New York, 1976.

[120] Peter Y. Yu and Manuel Cardona. *Fundamentals of Semiconductors: Physics and Materials Properties*. Springer, Berlin, 4th edition, 2010.

[121] Georg Kresse and Jürgen Furthmüller. Efficient iterative schemes for ab initio total-energy calculations using a plane-wave basis set. *Physical Review B*, 54(16):11169–11186, 1996.

[122] M. C. Payne, M. P. Teter, D. C. Allan, T. A. Arias, and J. D. Joannopoulos. Iterative minimization techniques for ab initio total-energy calculations: Molecular dynamics and conjugate gradients. *Reviews of Modern Physics*, 64(4):1045–1097, 1992.

[123] Richard F. W. Bader. *Atoms in Molecules: A Quantum Theory*. Oxford University Press, Oxford, 1990. Defines the quantum theory of atoms in molecules (QTAIM) — the conceptual foundation of Bader charge analysis.

[124] G. Henkelman, A. Arnaldsson, and H. Jónsson. A fast and robust algorithm for bader decomposition of charge density. *Computational Materials Science*, 36(3):354–360, 2006.

[125] E. Sanville, S. D. Kenny, R. Smith, and G. Henkelman. Improved grid-based algorithm for bader charge allocation. *Journal of Computational Chemistry*, 28(5):899–908, 2007.

[126] H. B. Michaelson. *The Work Function of the Elements and its Periodicity*, volume 48. 1977.

[127] Y. Zhao and K. Zhu. Charge transport and recombination in perovskite (ch3nh3)pbi3 sensitized solar cells. *Journal of Physical Chemistry Letters*, 5(21):4175–4186, 2017.

[128] Hao Gu-Shiliang Mei Shengwen Li Nan Zhang Shi Chen Yongqing Cai Guichuan Xing Junmin Xia, Chao Liang. Surface passivation toward efficient and stable perovskite solar cells.

[129] D. H. Cao, C. C. Stoumpos, O. K. Farha, J. T. Hupp, and M. G. Kanatzidis. 2d homologous perovskites as light-absorbing materials for solar cell applications. *Journal of the American Chemical Society*, 137(25):7843–7850, 2018.

[130] D. R. Hartree. The wave mechanics of an atom with a non-coulomb central field. part i. theory and methods. *Mathematical Proceedings of the Cambridge Philosophical Society*, 24(1):89–110, 1928. Introduced the self-consistent field (SCF) method and the concept of the Hartree potential.

[131] M. Peressi, A. Baldereschi, S. Baroni, and R. Resta. Band engineering at interfaces: Theory and numerical experiments. *Journal of Physics D: Applied Physics*, 31(11):1273–1299, 1998.

[132] J. Neugebauer and M. Scheffler. Adsorbate-substrate and adsorbate–adsorbate interactions of na and k adlayers on al(111). *Physical Review B*, 46(24):16067–16080, 1992. Introduced planar-averaged electrostatic potential analysis for surfaces.

[133] S. De Wolf, J. Holovsky, S. J. Moon, L. Löfgren, K. Jäger, B. Niesen, M. Ledinsky, F. J. Haug, J. H. Yum, and C. Ballif. Organometallic halide perovskites: Sharp optical absorption edge and its relation to photovoltaic performance. *The Journal of Physical Chemistry Letters*, 5(6):1035–1039, 2014.

[134] Henry J. Snaith. Perovskites: The emergence of a new era for low-cost, high-efficiency solar cells. *The Journal of Physical Chemistry Letters*, 4(21):3623–3630, 2013.

[135] W. Shockley and H. J. Queisser. Detailed balance limit of efficiency of p–n junction solar cells. *Journal of Applied Physics*, 32(3):510–519, 1961.

[136] Christoph J. Brabec, Vladimir Dyakonov, and Ullrich Scherf. Organic photovoltaics: Materials, device physics, and manufacturing technologies. *Wiley-VCH*, 2008.

[137] Maximilian T. Sirtl, Firouzeh Ebadi, Bas T. van Gorkom, Patrick Ganswindt, René A. J. Janssen, Thomas Bein, and Wolfgang Tress. The bottlenecks of cs2agbibr6 solar cells: How contacts and slow transients limit the performance. *Advanced Optical Materials*, 9(14):2100202, 2021.

[138] Eric T. McClure, Molly R. Ball, Wolfgang Windl, and Patrick M. Woodward. Cs2agbix6 (x = br, cl): New visible light absorbing, lead-free halide perovskite semiconductors. *Chemistry of Materials*, 28(5):1348–1354, 2016.

[139] Hongwei Lei, David Hardy, and Feng Gao. Lead-free double perovskite cs2agbibr6: Fundamentals, applications, and perspectives. *Advanced Functional Materials*, 31(49):2105898, 2021.

[140] Enrico Greul, Michiel L. Petrus, Andreas Binek, Pablo Docampo, and Thomas Bein. Highly stable, phase pure cs2agbibr6 double perovskite thin films for optoelectronic applications. *J. Mater. Chem. A*, 5:19972–19981, 2017.

[141] Runming Wang, Hongyan Li, and Hongzhe Sun. Bismuth: Environmental pollution and health effects. In Jerome Nriagu, editor, *Encyclopedia of Environmental Health (Second Edition)*, pages 415–423. Elsevier, Oxford, second edition edition, 2019.

[142] Robert L. Z. Hoye, Lissa Eyre, Fengxia Wei, Federico Brivio, Aditya Sadhanala, Shijing Sun, Weiwei Li, Kelvin H. L. Zhang, Judith L. MacManus-Driscoll, Paul D. Bristowe, Richard H. Friend, Anthony K. Cheetham, and Felix Deschler. Fundamental carrier lifetime exceeding 1 µs in cs2agbibr6 double perovskite. *Advanced Materials Interfaces*, 5(15):1800464, 2018.

[143] Zewei Li, Satyaprasad P. Senanayak, Linjie Dai, Gunnar Kusch, Ravichandran Shivanna, Youcheng Zhang, Dipika Pradhan, Junzhi Ye, Yi-Teng Huang, Henning Sirringhaus, Rachel A. Oliver, Neil C. Greenham, Richard H. Friend, and Robert L. Z. Hoye. Understanding the role of grain boundaries on charge-carrier and ion transport in cs2agbibr6 thin films. *Advanced Functional Materials*, 31(49):2104981, 2021.

[144] Adam H. Slavney, Te Hu, Aaron M. Lindenberg, and Hemamala I. Karunadasa. A bismuth-halide double perovskite with long carrier recombination lifetime for photovoltaic applications. *Journal of the American Chemical Society*, 138(7):2138–2141, 2016.

[145] Fabian Schmitz, Raphael Neisius, Jonas Horn, Joachim Sann, Derck Schlettwein, Marina Gerhard, and Teresa Gatti. Tuning the optical properties of 2d monolayer silver-bismuth bromide double perovskite by halide substitution. *Nanotechnology*, 33(21):215706, mar 2022.

[146] Robin Kentsch, Mirko Scholz, Jonas Horn, Derck Schlettwein, Kawon Oum, and Thomas Lenzer. Exciton dynamics and electron–phonon coupling affect the photovoltaic performance of the cs2agbibr6 double perovskite. *The Journal of Physical Chemistry C*, 122(45):25940–25947, 2018.

[147] Femi Igbari, Rui Wang, Zhao-Kui Wang, Xing-Juan Ma, Qiang Wang, Kai-Li Wang, Yue Zhang, Liang-Sheng Liao, and Yang Yang. Composition stoichiometry of cs2agbibr6 films for highly efficient lead-free perovskite solar cells. *Nano Letters*, 19(3):2066–2073, 2019. PMID: 30803237.

[148] Zhenxing Li, Ping Wang, Chang Ma, Femi Igbari, Yikun Kang, Kai-Li Wang, Weiyu Song, Chong Dong, Yanjie Li, Jiasai Yao, Dong Meng, Zhao-Kui Wang, and Yang Yang. Single-layered mxene nanosheets doping tio2 for efficient and stable double perovskite solar cells. *Journal of the American Chemical Society*, 143(6):2593–2600, 2021. PMID: 33535753.

[149] Ke-zhao Du, Weiwei Meng, Xiaoming Wang, Yanfa Yan, and David B. Mitzi. Bandgap engineering of lead-free double perovskite cs2agbibr6 through trivalent metal alloying. *Angewandte Chemie International Edition*, 56(28):8158–8162, 2017.

[150] Julian A. Steele, Pascal Puech, Masoumeh Keshavarz, Ruoxi Yang, Subhasree Banerjee, Elke Debroye, Cheol Woong Kim, Haifeng Yuan, Nam Ho Heo, Johan Vanacken, Aron Walsh, Johan Hofkens, and Maarten B. J. Roeffaers. Giant electron–phonon coupling and deep conduction band resonance in metal halide double perovskite. *ACS Nano*, 12(8):8081–8090, 2018. PMID: 30086242.

[151] Joshua Leveillee, George Volonakis, and Feliciano Giustino. Phonon-limited mobility and electron–phonon coupling in lead-free halide double perovskites. *The Journal of Physical Chemistry Letters*, 12(18):4474–4482, 2021. PMID: 33956454.

[152] Giulia Longo, Suhas Mahesh, Leonardo R. V. Buizza, Adam D. Wright, Alexandra J. Ramadan, Mojtaba Abdi-Jalebi, Pabitra K. Nayak, Laura M. Herz, and Henry J. Snaith. Understanding the performance-limiting factors of cs2agbibr6 double-perovskite solar cells. *ACS Energy Letters*, 5(7):2200–2207, 2020.

[153] Dandan Zhao, Chao Liang, Bingzhe Wang, Tanghao Liu, Qi Wei, Kaiyang Wang, Hao Gu, Sisi Wang, Shiliang Mei, and Guichuan Xing. Overcoming the limitation of cs2agbibr6 double perovskite solar cells through using mesoporous tio2 electron extraction layer. *ENERGY & ENVIRONMENTAL MATERIALS*, 5(4):1317–1322, 2022.

[154] Naveen Kumar Tailor, Nishi Parikh, Pankaj Yadav, and Soumitra Satapathi. Dielectric relaxation and polaron hopping in cs2agbibr6 halide double perovskites. *The Journal of Physical Chemistry C*, 126(24):10199–10208, 2022.

[155] Naveen Kumar Tailor, Saurabh K. Saini, Pankaj Yadav, Mahesh Kumar, and Soumitra Satapathi. Elucidating polaron dynamics in cs2agbibr6 double per-

ovskite. *The Journal of Physical Chemistry Letters*, 14(3):730–736, 2023. PMID: 36649028.

[156] Maximilian T. Sirtl, Rik Hooijer, Melina Armer, Firouzeh G. Ebadi, Mahdi Mohammadi, Clément Maheu, Andreas Weis, Bas T. van Gorkom, Sebastian Häringer, René A. J. Janssen, Thomas Mayer, Vladimir Dyakonov, Wolfgang Tress, and Thomas Bein. 2d/3d hybrid cs2agbibr6 double perovskite solar cells: Improved energy level alignment for higher contact-selectivity and large open circuit voltage. *Advanced Energy Materials*, 12(7):2103215, 2022.

[157] Fang Chen, Hongwei Huang, Liqun Ye, Tierui Zhang, Yihe Zhang, Xiaopeng Han, and Tianyi Ma. Thickness-dependent facet junction control of layered bioio3 single crystals for highly efficient co2 photoreduction. *Advanced Functional Materials*, 28(46):1804284, 2018.

[158] Lun Zhang, Yinyan Xu, Pujun Niu, Mei Lyu, Hongbo Lu, and Jun Zhu. Regulating film crystallization kinetics with thiourea additive in cs2agbibr6 solar cells. *Journal of Physics D: Applied Physics*, 56(7):075501, jan 2023.

[159] Yan Hua, Yipeng Zhou, Daocheng Hong, Sushu Wan, Xixi Hu, Daiqian Xie, and Yuxi Tian. Identification of the band gap energy of two-dimensional (oa)2(ma)n1pbni3n+1 perovskite with up to 10 layers. *The Journal of Physical Chemistry Letters*, 10(22):7025–7030, 2019. PMID: 31660739.

[160] Jasmina A. Sichert, Yu Tong, Niklas Mutz, Mathias Vollmer, Stefan Fischer, Karolina Z. Milowska, Ramon García Cortadella, Bert Nickel, Carlos Cardenas-Daw, Jacek K. Stolarczyk, Alexander S. Urban, and Jochen Feldmann. Quantum size effect in organometal halide perovskite nanoplatelets. *Nano Letters*, 15(10):6521–6527, 2015. PMID: 26327242.

[161] Carmen Ortiz-Cervantes, Paulina Carmona-Monroy, and Diego Solis-Ibarra.

Two-dimensional halide perovskites in solar cells: 2d or not 2d? *ChemSusChem*, 12(8):1560–1575, 2019.

[162] Po-Cheng Huang, Shao-Ku Huang, Ting-Chun Lai, Min-Chuan Shih, Hung-Chang Hsu, Chun-Hsiang Chen, Cheng-Chieh Lin, Chun-Hao Chiang, Chi-Ying Lin, Kazuhito Tsukagoshi, Chun-Wei Chen, Ya-Ping Chiu, Shiow-Fon Tsay, and Ying-Chiao Wang. Visualizing band alignment across 2d/3d perovskite heterointerfaces of solar cells with light-modulated scanning tunneling microscopy. *Nano Energy*, 89:106362, 2021.

[163] Tiankai Zhang, Mingzhu Long, Minchao Qin, Xinhui Lu, Si Chen, Fangyan Xie, Li Gong, Jian Chen, Ming Chu, Qian Miao, Zefeng Chen, Wangying Xu, Pengyi Liu, Weiguang Xie, and Jian bin Xu. Stable and efficient 3d-2d perovskite-perovskite planar heterojunction solar cell without organic hole transport layer. *Joule*, 2(12):2706–2721, 2018.

[164] Maximilian T. Sirtl, Melina Armer, Lennart K. Reb, Rik Hooijer, Patrick Dörflinger, Manuel A. Scheel, Kristofer Tvingstedt, Philipp Rieder, Nadja Glück, Pallavi Pandit, Stephan V. Roth, Peter Müller-Buschbaum, Vladimir Dyakonov, and Thomas Bein. Optoelectronic properties of cs2agbibr6 thin films: The influence of precursor stoichiometry. *ACS Applied Energy Materials*, 3(12):11597–11609, 2020.

[165] Yunpeng Yao, Bo Kou, Yu Peng, Zhenyue Wu, Lina Li, Sasa Wang, Xinyuan Zhang, Xitao Liu, and Junhua Luo. (c3h9ni)4agbii8: a direct-bandgap layered double perovskite based on a short-chain spacer cation for light absorption. *Chem. Commun.*, 56:3206–3209, 2020.

[166] Dongyu Liu, Carlos Mora Perez, Andrey S. Vasenko, and Oleg V. Prezhdo. Ag–bi charge redistribution creates deep traps in defective cs2agbibr6: Machine learning analysis of density functional theory. *The Journal of Physical Chemistry Letters*, 13(16):3645–3651, 2022. PMID: 35435697.

[167] Yalan She, Zhufeng Hou, Oleg V. Prezhdo, and Wei Li. Identifying and passivating killer defects in pb-free double cs2agbibr6 perovskite. *The Journal of Physical Chemistry Letters*, 12(43):10581–10588, 2021. PMID: 34694808.

[168] Zhenglin He, Qingli Tang, Xing Liu, Xuan Yan, Kan Li, and Dongting Yue. Lead-free cs2agbibr6 perovskite with enriched surface defects for efficient photocatalytic hydrogen evolution. *Energy & Fuels*, 35(18):15005–15009, 2021.

[169] Mohammad Saeed Shadabroo, Hossein Abdizadeh, and Mohammad Reza Golobostanfard. Dimethyl sulfoxide vapor-assisted cs2agbibr6 homogenous film deposition for solar cell application. *ACS Applied Energy Materials*, 4(7):6797–6805, 2021.

[170] Nathan Daem, Jennifer Dewalque, Felix Lang, Anthony Maho, Gilles Spronck, Catherine Henrist, Pierre Colson, Samuel D. Stranks, and Rudi Cloots. Spray-coated lead-free cs2agbibr6 double perovskite solar cells with high open-circuit voltage. *Solar RRL*, 5(9):2100422, 2021.

[171] Ping Fan, Huan-Xin Peng, Zhuang-Hao Zheng, Zi-Hang Chen, Shi-Jie Tan, Xing-Ye Chen, Yan-Di Luo, Zheng-Hua Su, Jing-Ting Luo, and Guang-Xing Liang. Single-source vapor-deposited cs2agbibr6 thin films for lead-free perovskite solar cells. *Nanomaterials*, 9(12), 2019.

[172] Martina Pantaler, Kyung Taek Cho, Valentin I. E. Queloz, Inés García Benito, Christian Fettkenhauer, Irina Anusca, Mohammad Khaja Nazeeruddin, Doru C. Lupascu, and Giulia Grancini. Hysteresis-free lead-free double-perovskite solar cells by interface engineering. *ACS Energy Letters*, 3(8):1781–1786, 2018.

[173] John P. Perdew, Kieron Burke, and Matthias Ernzerhof. Generalized gradient approximation made simple. *Phys. Rev. Lett.*, 77:3865–3868, Oct 1996.

[174] G. Kresse and D. Joubert. From ultrasoft pseudopotentials to the projector augmented-wave method. *Phys. Rev. B*, 59:1758–1775, Jan 1999.

[175] Fei Zhang, Dongqin Bi, Norman Pellet, Chuanxiao Xiao, Zhen Li, Joseph J. Berry, Shaik Mohammed Zakeeruddin, Kai Zhu, and Michael Grätzel. Suppressing defects through the synergistic effect of a lewis base and a lewis acid for highly efficient and stable perovskite solar cells. *Energy and Environmental Science*, 11(12):3480 – 3490, 2018.

[176] Snigdha Lal, Marcello Righetto, Aleksander M. Ulatowski, Silvia G. Motti, Zhuotong Sun, Judith L. MacManus-Driscoll, Robert L. Z. Hoye, and Laura M. Herz. Bandlike transport and charge-carrier dynamics in bioi films. *The Journal of Physical Chemistry Letters*, 14(29):6620–6629, 2023. PMID: 37462354.

[177] Kyle M. McCall, Constantinos C. Stoumpos, Svetlana S. Kostina, Mercouri G. Kanatzidis, and Bruce W. Wessels. Strong electron–phonon coupling and self-trapped excitons in the defect halide perovskites a3m2i9 (a = cs, rb; m = bi, sb). *Chemistry of Materials*, 29(9):4129–4145, 2017.

[178] Leonardo R. V. Buizza, Adam D. Wright, Giulia Longo, Harry C. Sansom, Chelsea Q. Xia, Matthew J. Rosseinsky, Michael B. Johnston, Henry J. Snaith, and Laura M. Herz. Charge-carrier mobility and localization in semiconducting cu2agbii6 for photovoltaic applications. *ACS Energy Letters*, 6(5):1729–1739, 2021. PMID: 34056108.

[179] G. Krishnamurthy Grandhi. Promises and challenges of indoor photovoltaics. *Nature Reviews Clean Technology*, 2025.

[180] Zaichun Sun and Tahta Amrillah. Potential application of bismuth oxyiodide (bioi) when it meets light. *Nanoscale*, 16:5079–5106, 2024.

[181] Fabrication of bioi nanosheets with exposed (001) and (110) facets with different methods for photocatalytic oxidation elemental mercury. *Colloid and Interface Science Communications*, 40:100357, 2021.

[182] Xin Mai, Ran Gao, Yeheng Zhang, Junnan Chen, Wensong Lin, and Chengli Mai. (001)-tio2 nanosheets loaded on bioi improve carrier separation and enhance the photocatalytic activity. *New J. Chem.*, 47:16611–16620, 2023.

[183] Hsinhan Tsai. High-efficiency two-dimensional ruddlesden–popper perovskite solar cells. *Nature*, 2016.

[184] Haijun Zhang, Lu Liu, and Zhen Zhou. First-principles studies on facet-dependent photocatalytic properties of bismuth oxyhalides (bioxs). *RSC Adv.*, 2:9224–9229, 2012.

[185] Amol C. Badgujar, Brijesh Singh Yadav, Golu Kumar Jha, and Sanjay R. Dhage. Room temperature sputtered aluminum-doped zno thin film transparent electrode for application in solar cells and for low-band-gap optoelectronic devices. *ACS Omega*, 7(16):14203–14210, 2022.

[186] Darlington C. Ashiegbu, Nosipho Moloto, and Herman Potgieter. Improved photocatalytic activity of zno-[10 *Environ. Sci.: Adv.*, 2:325–338, 2023.

[187] Influence of annealing temperature on the properties of zno thin films grown by sputtering. *Energy Procedia*, 25:55–61, 2012. PV Asia Pacific Conference 2011.

[188] Shuyan Shao and Maria Antonietta Loi. The role of the interfaces in perovskite solar cells. *Advanced Materials Interfaces*, 7(1):1901469, 2020.

[189] Junpeng Wang, Zeyan Wang, Baibiao Huang, Yandong Ma, Yuanyuan Liu, Xiaoyan Qin, Xiaoyang Zhang, and Ying Dai. Oxygen vacancy induced band-gap narrowing and enhanced visible light photocatalytic activity of zno. *ACS Applied Materials & Interfaces*, 4(8):4024–4030, 2012. PMID: 22786575.

[190] Robert A. Jagt, Tahmida N. Huq, Katharina M. Börsig, Daniella Sauven, Lana C. Lee, Judith L. MacManus-Driscoll, and Robert L. Z. Hoye. Controlling the preferred orientation of layered bioi solar absorbers. *J. Mater. Chem. C*, 8:10791–10797, 2020.

[191] Yueheng Peng, Tahmida N. Huq, Jianjun Mei, Luis Portilla, Robert A. Jagt, Luigi G. Occhipinti, Judith L. MacManus-Driscoll, Robert L. Z. Hoye, and Vincenzo Pecunia. Lead-free perovskite-inspired absorbers for indoor photovoltaics. *Advanced Energy Materials*, 11(1):2002761, 2021.

[192] Yong Zhou, Beitong Cheng, Shuai Huang, Xingyong Huang, Ruomei Jiang, Xule Wang, Wei Zhang, Baonan Jia, Pengfei Lu, and Hai-Zhi Song. The tunable electronic and optical properties of two-dimensional bismuth oxyhalides. *Nanomaterials*, 13(20), 2023.

[193] Katherine S. Giunta, Shara N. McKee, Aaron D. Nicholas, and Robert D. Pike. Bicui4(pyridine)5 a neutral ligand-supported compound of bii3 and cui. *Inorganic Chemistry Communications*, 147:110245, 2023.

[194] A. N Usol'tsev. Bismuth(iii) iodide complexes with 1-ethyl-4-dimethylaminopyridinium: Structure, thermal stability, and optical properties. *Russian Journal of Inorganic Chemistry*, 2021.

[195] Andreas Savin. The electron localization function (elf) and its relatives: interpretations and difficulties. *Journal of Molecular Structure: THEOCHEM*, 727(1):127–131, 2005. Dedicated to Ramon Carbo´-Dorca on the Occasion of his 65th Birthday.

[196] Kelvin Dsouza and Daryoosh Vashaee. Cooperative pseudo jahn teller distortion derives phase transitions in bismuth oxide. *Materials Chemistry and Physics*, 299:127534, 2023.

[197] Jean-Yves Raty, Carlo Gatti, Carl-Friedrich Schön, and Matthias Wuttig. How to identify lone pairs, van der waals gaps, and metavalent bonding using charge and pair density methods: From elemental chalcogens to lead chalcogenides and phase-change materials. *physica status solidi (RRL) – Rapid Research Letters*, 15(11):2000534, 2021.

[198] Liam P. Griffin, Tim-Niclas Streit, Robin Sievers, Simon Aldridge, Rosa M. Gomila, Antonio Frontera, and Moritz Malischewski. Crystallographic evidence for bi(i) as the heaviest halogen bond acceptor. *Journal of the American Chemical Society*, 146(43):29877–29882, 2024. PMID: 39423030.

[199] Wakjira. Electronic, optical, phonon, and thermodynamic properties of bismuth oxyhalides for photocatalysis application using density functional theory. *Discover Materials*, 2024.

[200] Slawomir Berski, Zdzislaw Latajka, and Agnieszka J. Gordon. Oxygen bound iodine (o–i): The electron localization function (elf) study on bonding in cis- and trans-iono. *Chemical Physics Letters*, 506(1):15–21, 2011.

[201] V.N. Jafarova and G.S. Orudzhev. Structural and electronic properties of zno: A first-principles density-functional theory study within lda(gga) and lda(gga)+u methods. *Solid State Communications*, 325:114166, 2021.

[202] Kausar Harun, Norsakinah Mansor, Zainal Arifin Ahmad, and Ahmad Azmin Mohamad. Electronic properties of zno nanoparticles synthesized by sol-gel method: A lda+u calculation and experimental study. *Procedia Chemistry*, 19:125–132, 2016. 5th International Conference on Recent Advances in Materials, Minerals and Environment (RAMM) 2nd International Postgraduate Conference on Materials, Mineral and Polymer (MAMIP).

[203] Kausar Harun, Nor Azmira Salleh, Bahri Deghfel, Muhamad Kamil Yaakob, and Ahmad Azmin Mohamad. Dft + u calculations for electronic, structural, and optical properties of zno wurtzite structure: A review. *Results in Physics*, 16:102829, 2020.

[204] Slimane Haffad and Kiptiemoi Korir Kiprono. Interfacial structure and electronic properties of tio2/zno/tio2 for photocatalytic and photovoltaic applications: A theoretical study. *Surface Science*, 686:10–16, 2019.

[205] Stefan Grimme, Jens Antony, Stephan Ehrlich, and Helge Krieg. A consistent and accurate ab initio parametrization of density functional dispersion correction (dft-d) for the 94 elements h-pu. *The Journal of Chemical Physics*, 132(15):154104, 04 2010.

[206] G. Kresse and J. Hafner. Ab initio molecular dynamics for liquid metals. *Phys. Rev. B*, 47:558–561, Jan 1993.

[207] Bernard Wenger, Pabitra K. Nayak, Xiaoming Wen, Sameer V. Kesava, Nakita K. Noel, and Henry J. Snaith. Consolidation of the optoelectronic properties of ch3nh3pbbr3 perovskite single crystals. *Nature Communications*, 8(1), 2017.

[208] Hui Yu, Haipeng Lu, Fangyan Xie, Shuang Zhou, and Ni Zhao. Native defect-induced hysteresis behavior in organolead iodide perovskite solar cells. *Advanced Functional Materials*, 26(9):1411–1419.

[209] Giovanni Landi, Heinz Christoph Neitzert, Carlo Barone, Costantino Mauro, Felix Lang, Steve Albrecht, Bernd Rech, and Sergio Pagano. Correlation between electronic defect states distribution and device performance of perovskite solar cells. *Advanced Science*, 4(10), 2017.

[210] Dane W. DeQuilettes, Sarah M. Vorpahl, Samuel D. Stranks, Hirokazu Nagaoka, Giles E. Eperon, Mark E. Ziffer, Henry J. Snaith, and David S. Ginger. Impact of microstructure on local carrier lifetime in perovskite solar cells. *Science*, 348(6235):683 – 686, 2015. Cited by: 2012.

[211] Tinghuan Yang, Yang Yang, Tianqi Niu, Erxin Zhao, Nan Wu, Shuang Wang, Xin Chen, Shumei Wang, Yajie Wang, Yin Wu, Zheng Zhang, Cheng Ma, Yongshuai Gong, Dongxue Liu, and Kui Zhao. Facet orientation-dependent strain relaxation stabilizes fapbi3 perovskite solar cells. *ACS Energy Letters*, 10(1):427–438, 2025.

[212] Overcoming shockley-queisser limit using halide perovskite platform? *Joule*, 6(4):756–771, 2022.

[213] Margdaline Musanga Ligavo, Sebastian Waita, Francis Wanjala Nyongesa, and Mmantsae Diale. Surface passivation of perovskite thin films through sequential physical vapour deposition for improved stability, structural, optical and morphological properties. *Optical Materials*, 159:116613, 2025.

[214] Junke Wang, Shuaifeng Hu, Zehua Chen, Zhongcheng Yuan, Pei Zhao, Akash Dasgupta, Fengning Yang, Jin Yao, Minh Anh Truong, Gunnar Kusch, Esther Y-H. Hung, Nick R. M. Schipper, Laura Bellini, Guus J. W. Aalbers, Zonghao Liu, Rachel A. Oliver, Atsushi Wakamiya, René A. J. Janssen, and Henry J. Snaith. Exposing binding-favourable facets of perovskites for tandem solar cells. *Energy Environ. Sci.*, 18:7680–7694, 2025.

[215] Chunqing Ma, Felix T. Eickemeyer, Sun-Ho Lee, Dong-Ho Kang, Seok Joon Kwon, Michael Grätzel, and Nam-Gyu Park. Unveiling facet-dependent degradation and facet engineering for stable perovskite solar cells. *Science*, 379(6628):173–178, 2023.

[216] Chunqing Ma, Min-Chul Kang, Sun-Ho Lee, Seok Joon Kwon, Hyun-Woo Cha, Cheol-Woong Yang, and Nam-Gyu Park. Photovoltaically top-performing perovskite crystal facets. *Joule*, 6(11):2626–2643, 2022.

[217] Dongni Li, Xiangyu Sun, Yao Zhang, Zhen Guan, Yansong Yue, Qingya Wang, Lu Zhao, Fangze Liu, Jing Wei, and Hongbo Li. Uniaxial-oriented perovskite films with controllable orientation. *Advanced Science*, 11(19):2401184, 2024.

[218] Highly efficient and stable perovskite solar cells via a multifunctional hole transporting material. *Joule*, 8(6):1691–1706, 2024.

[219] Bo Xu, Dongqin Bi, Yong Hua, Peng Liu, Ming Cheng, Michael Grätzel, Lars Kloo, Anders Hagfeldt, and Licheng Sun. A low-cost spiro[fluorene-9,9-xanthene]-based hole transport material for highly efficient solid-state dye-sensitized solar cells and perovskite solar cells. *Energy Environ. Sci.*, 9:873–877, 2016.

[220] Shen Wang, Zihan Huang, Xuefeng Wang, Yingmin Li, Marcella Günther, Sophia Valenzuela, Pritesh Parikh, Amanda Cabreros, Wei Xiong, and Ying Shirley Meng. Unveiling the role of tbp-litfsi complexes in perovskite solar cells. *Journal of the American Chemical Society*, 140(48):16720 – 16730, 2018. Cited by: 251.

[221] Chuanxiao Xiao, Fei Zhang, Zhen Li, Steven P. Harvey, Xihan Chen, Kang Wang, Chun-Sheng Jiang, Kai Zhu, and Mowafak Al-Jassim. Inhomogeneous doping of perovskite materials by dopants from hole-transport layer. *Matter*, 2(1):261 – 272, 2020. Cited by: 50; All Open Access, Bronze Open Access, Green Open Access.

[222] Konrad Domanski, Juan-Pablo Correa-Baena, Nicolas Mine, Mohammad Khaja Nazeeruddin, Antonio Abate, Michael Saliba, Wolfgang Tress, Anders Hagfeldt, and Michael Grätzel. Not all that glitters is gold: Metal-migration-induced degradation in perovskite solar cells. *ACS Nano*, 10(6):6306 – 6314, 2016. Cited by: 1093; All Open Access, Green Open Access.

[223] Andreas Kaltzoglou, Maria Antoniadou, Athanassios G. Kontos, Constantinos C. Stoumpos, Dorothea Perganti, Eirini Siranidi, Vasilios Raptis, Kalliopi Trohidou, Vassilis Psycharis, Mercouri G. Kanatzidis, and Polycarpos Falaras. Optical-vibrational properties of the cs2snx6 (x = cl, br, i) defect perovskites and hole-transport efficiency in dye-sensitized solar cells. *The Journal of Physical Chemistry C*, 120(22):11777–11785, 2016.

[224] Jianbin Xu, Lusheng Liang, Chi-Lun Mai, Zilong Zhang, Qin Zhou, Qiu Xiong, Zhuangzhuang Zhang, Longhui Deng, and Peng Gao. Lewis-base containing spiro type hole transporting materials for high-performance perovskite solar cells with efficiency approaching 20 *Nanoscale*, 12:13157–13164, 2020.

[225] Mahdi Malekshahi Byranvand and Michael Saliba. Defect passivation of perovskite films for highly efficient and stable solar cells. *Solar RRL*, 5(8):2100295.

[226] Weibo Yan, Wensheng Yang, Kangjie Zhang, Hui Yu, Yuntian Yang, Hao Fan, Yuanyuan Qi, and Hao Xin. Enhancing performance and stability of perovskite solar cells through surface defect passivation with organic bidentate lewis bases. *ACS Omega*, 7(36):32383–32392, 2022.

[227] Abdulaziz S.R. Bati, Cheng Liu, Isaiah W. Gilley, Charles B. Musgrave, Aidan Maxwell, Julian A. Steele, Yi Yang, Hao Chen, Haoyue Wan, Jian Xu, Eduardo Solano, Rui Zhang, Chuying Huang, Benjamin Rehl, Nikolaos Lempesis, Virginia Carnevali, Andrea Vezzosi, Lewei Zeng, Luke Grater, Muzhi Li, Nicholas Rolston, Deokjae Choi, Vladislav Sláma, Ursula Rothlisberger, Lianzhou Wang, William A. Goddard, Mercouri G. Kanatzidis, Bin Chen, Osman M. Bakr, and Edward H. Sargent. A chemically bonded monolayer interface enables enhanced thermal stability and efficiency in pb-sn perovskite solar cells. *Joule*, 9(9):102047, 2025.

[228] Adsorption of molecular additive onto lead halide perovskite surfaces: A computational study on lewis base thiophene additive passivation. *Applied Surface Science*, 443:176–183, 2018.

[229] Yuan-Yu Chiu, Shih-Hsuan Chen, Kun-Mu Lee, Tz-Feng Lin, and Ming-Chung Wu. Side chain modulated carbazole-based bifunctional hole-shuttle interlayer simultaneously improves interfacial energy level alignment and defect passivation in high-efficiency perovskite solar cells. *Chemical Engineering Journal*, 477:147208, 2023.

[230] Aron Walsh, David J. Payne, Russell G. Egdell, and Graeme W. Watson. Stereochemistry of post-transition metal oxides: Revision of the classical lone pair model. *Chemical Society Reviews*, 40(9):4455–4463, 2011.

[231] D. Meggiolaro and F. De Angelis. First-principles modeling of defects and ion migration in lead halide perovskites. *ACS Energy Letters*, 3(10):2206–2222, 2018.

[232] Felix O. Kannemann and Axel D. Becke. Atomic volumes and polarizabilities in density-functional theory. *The Journal of Chemical Physics*, 136(3):034109, 01 2012.

[233] Ralph G. Pearson. Hard and soft acids and bases, hsab, part 1: Fundamental principles. *Journal of Chemical Education*, 45(9):581, 1968.

[234] Feng Gao, Hang Li, Boxin Jiao, Liguo Tan, Chengtang Deng, Xianjin Wang, Chao Luo, Changling Zhan, Elke Debroye, Yingchen Peng, Ye Yang, Chenyi Yi, and Qing Zhao. Perovskite facet heterojunction solar cells. *Joule*, 9(2):101787, 2025.

[235] Zhendong Guo, Man Yuan, Gaoyuan Chen, Feng Liu, Ruifeng Lu, and Wan-Jian Yin. Understanding defects in perovskite solar cells through computation: Current knowledge and future challenge. *Advanced Science*, 11(20):2305799, 2024.

[236] Saqib Javaid and Geunsik Lee. The impact of molecular orientation on carrier transfer characteristics at a phthalocyanine and halide perovskite interface. *RSC Adv.*, 11:31776–31782, 2021.

[237] Wenhui Li, Chuanli Wu, and Xiuxun Han. Controlling molecular orientation of small molecular dopant-free hole-transport materials: Toward efficient and stable perovskite solar cells. *Molecules*, 28(7), 2023.

[238] Sourav Nath, Raymond J. Butcher, Werner Kaminsky, Suman Adhikari, Asmet N. Azizova, Ömer Faruk Tutar, Elizaveta V. Panova, Ghodrat Mahmoudi, Rosa M. Gomila, Antonio Frontera, and Damir A. Safin. A structural versatility of the lead(ii) coordination compounds with n-(pyridin-2-ylmethylene)isonicotinohydrazide. *Inorganic Chemistry Communications*, 182:115459, 2025.

[239] R. D. Shannon. Revised effective ionic radii and systematic studies of inter-

atomic distances in halides and chalcogenides. *Acta Crystallographica Section A*, 32(5):751–767, 1976.

[240] Riming Nie, Peikun Zhang, Jiaxing Gao, Cheng Wang, Weicun Chu, Luyao Li, Kaiyu Wang, Dongmin Qian, Fanrong Lin, Xuefeng Xia, Yong Wu, Lingfeng Chao, Chunyang Miao, Xiaoming Zhao, Wanlin Guo, and Zhuhua Zhang. Enhanced coordination interaction with multi-site binding ligands for efficient and stable perovskite solar cells. *Nature Communications*, 16(1):6438, 2025.

[241] Alejandro Garrote-Márquez, Lucas Lodeiro, Rahul Suresh, Norge Cruz Hernández, Ricardo Grau-Crespo, and Eduardo Menéndez-Proupin. Hydrogen bonds in lead halide perovskites: Insights from ab initio molecular dynamics. *The Journal of Physical Chemistry C*, 127(32):15901–15910, August 2023.

[242] Liangyou Lin, Timothy W. Jones, Terry Chien-Jen Yang, Xinyu Li, Congcong Wu, Zichen Xiao, Haijin Li, Jinhua Li, Jingwen Qian, Lin Lin, Javen Qinfeng Shi, Samuel D. Stranks, Gregory J. Wilson, and Xianbao Wang. Hydrogen bonding in perovskite solar cells. *Matter*, 7(1):38–58, 2024.

[243] Z. Yu et al. Hydrogen bond-assisted dual passivation for blue perovskite light-emitting diodes. *ACS Applied Materials & Interfaces*, 2023. Preprint/author-accepted manuscript.

[244] Christian M. Wolff, Pietro Caprioglio, Martin Stolterfoht, and Dieter Neher. Nonradiative recombination in perovskite solar cells: The role of interfaces. *Advanced Materials*, 31(52):1902762, 2019.

[245] John A. Brehm, Hiroyuki Takenaka, Chan-Woo Lee, Ilya Grinberg, Joseph W. Bennett, Michael Rutenberg Schoenberg, and Andrew M. Rappe. Density functional theory study of hypothetical $pbtio_3$-based oxysulfides. *Phys. Rev. B*, 89:195202, May 2014.

[246] Małgorzata Wierzbowska, Kamil Wojtkowiak, Alicja Mikłas, and Aneta Jezierska. Consequences of the pbs bond formation for lead halide perovskites. *Chemistry – A European Journal*, 30(63):e202402205.

[247] Xiaojia Xu, Hao Zhang, Erpeng Li, Pengbin Ru, Han Chen, Zhenhua Chen, Yongzhen Wu, He Tian, and Wei-Hong Zhu. Electron-enriched thione enables strong pb–s interaction for stabilizing high quality cspbi3 perovskite films with low-temperature processing. *Chem. Sci.*, 11:3132–3140, 2020.

[248] Ruven L. Davidovich, Vitalie Stavila, Dmitry V. Marinin, Elena I. Voit, and Kenton H. Whitmire. Stereochemistry of lead(ii) complexes with oxygen donor ligands. *Coordination Chemistry Reviews*, 253(9):1316–1352, 2009.

[249] Yun Wang, Bobby G. Sumpter, Jingsong Huang, Haimin Zhang, Porun Liu, Huagui Yang, and Huijun Zhao. Density functional studies of stoichiometric surfaces of orthorhombic hybrid perovskite ch3nh3pbi3. *The Journal of Physical Chemistry C*, 119(2):1136–1145, 2015.

[250] J. Clay Jr. Hamill, Oluwaseun Romiluyi, Sara A. Thomas, Jacquelyn Cetola, Jeffrey Schwartz, Michael F. Toney, Paulette Clancy, and Yueh-Lin Loo. Sulfur-donor solvents strongly coordinate pb2+ in hybrid organic–inorganic perovskite precursor solutions. *The Journal of Physical Chemistry C*, 124(27):14496–14502, 2020.

[251] Cheng Wang, Riming Nie, Yiming Dai, Huanyu Tai, Bingjian Zhu, Luyao Zhao, Yong Wu, Wanlin Guo, and Sang Il Seok. Enhancing the inherent stability of perovskite solar cells through chalcogenide-halide combinations. *Energy Environ. Sci.*, 17:1368–1386, 2024.

[252] Konstantinos D. Demadis, Chris M. Hartshorn, and Thomas J. Meyer. The localized-to-delocalized transition in mixed-valence chemistry. *Chemical Reviews*, 101(9):2655–2686, 2001. PMID: 11749392.

[253] Paul F. Barbara, Thomas J. Meyer, and Mark A. Ratner. Contemporary issues in electron transfer research. *The Journal of Physical Chemistry*, 100(31):13148–13168, 1996.

[254] M D Newton and N Sutin. Electron transfer reactions in condensed phases. *Annual Review of Physical Chemistry*, 35(Volume 35,):437–480, 1984.

[255] Christian Wehrenfennig, Giles E. Eperon, Michael B. Johnston, Henry J. Snaith, and Laura M. Herz. High charge carrier mobilities and lifetimes in organolead trihalide perovskites. *Advanced Materials*, 26(10):1584 – 1589, 2014. All Open Access, Green Open Access, Hybrid Gold Open Access.

[256] Girish K H. Advances in surface passivation of perovskites using organic halide salts for efficient and stable solar cells. *Surfaces and Interfaces*, 26:101420, 2021.

[257] Cheng Bi, Yuchuan Shao, Yongbo Yuan, Zhengguo Xiao, Chenggong Wang, Yongli Gao, and Jinsong Huang. Understanding the formation and evolution of interdiffusion grown organolead halide perovskite thin films by thermal annealing. *Journal of Materials Chemistry A*, 2(43):18508 – 18514, 2014. Cited by: 289.

[258] Amalie Dualeh, Nicolas Tétreault, Thomas Moehl, Peng Gao, Mohammad Khaja Nazeeruddin, and Michael Grätzel. Effect of annealing temperature on film morphology of organic-inorganic hybrid pervoskite solid-state solar cells. *Advanced Functional Materials*, 24(21):3250 – 3258, 2014. Cited by: 911.

[259] Wan-Jian Yin, Tingting Shi, and Yanfa Yan. Unusual defect physics in ch3nh3pbi3 perovskite solar cell absorber. *Applied Physics Letters*, 104(6), 2014. Cited by: 2501.

[260] Daniele Meggiolaro, Edoardo Mosconi, and Filippo De Angelis. Formation of surface defects dominates ion migration in lead-halide perovskites. *ACS Energy Letters*, 4(3):779–785, 2019.

[261] Jiahua Tao, Chunhu Zhao, Zhaojin Wang, You Chen, Lele Zang, Guang Yang, Yang Bai, and Junhao Chu. Suppressing non-radiative recombination for efficient and stable perovskite solar cells. *Energy Environ. Sci.*, 18:509–544, 2025.

[262] Jincheol Kim, Jae Sung Yun, Yongyoon Cho, Da Seul Lee, Benjamin Wilkinson, Arman Mahboubi Soufiani, Xiaofan Deng, Jianghui Zheng, Adrian Shi, Sean Lim, Sheng Chen, Ziv Hameiri, Meng Zhang, Cho Fai Jonathan Lau, Shujuan Huang, Martin A. Green, and Anita W. Y. Ho-Baillie. Overcoming the challenges of large-area high-efficiency perovskite solar cells. *ACS Energy Letters*, 2(9):1978 – 1984, 2017. Cited by: 156; All Open Access, Green Open Access.

[263] Efat Jokar, Cheng-Hsun Chien, Amir Fathi, Mohammad Rameez, Yu-Hao Chang, and Eric Wei-Guang Diau. Slow surface passivation and crystal relaxation with additives to improve device performance and durability for tin-based perovskite solar cells. *Energy and Environmental Science*, 11(9):2353 – 2362, 2018. Cited by: 457.

[264] J. Suo, B. Yang, and A. Hagfeldt. Passivation strategies through surface reconstruction toward highly efficient and stable perovskite solar cells on n–i–p architecture. *Energies*, 14(16):4836, 2021.

[265] J. Lee et al. Polymer functional layers for perovskite solar cells. *Polymers*, 17(19):2607, 2025.

[266] Bowen Yang, Jiajia Suo, Francesco Di Giacomo, Selina Olthof, Dmitry Bogachuk, YeonJu Kim, Xiaoxiao Sun, Lukas Wagner, Fan Fu, Shaik M. Zakeeruddin, Andreas Hinsch, Michael Grätzel, Aldo Di Carlo, and Anders Hagfeldt. Interfacial passivation engineering of perovskite solar cells with fill factor over 82% and outstanding operational stability on n-i-p architecture. *ACS Energy Letters*, 6(11):3916–3923, 2021.

[267] Kristofer Tvingstedt, Olga Malinkiewicz, Andreas Baumann, Carsten Deibel,

Henry J. Snaith, Vladimir Dyakonov, and Henk J. Bolink. Radiative efficiency of lead iodide based perovskite solar cells. *Scientific Reports*, 4, 2014. Cited by: 285; All Open Access, Gold Open Access, Green Open Access.

[268] Defects in perovskite halides and their effects in solar cells. *Nature Energy*, 2016.

[269] Surface passivation for efficient and stable perovskite solar cells in ambient air: The structural effect of amine molecules. *Ceramics International*, 50(5):7528–7537, 2024.

[270] Xiaoming Chang, Randi Azmi, Tinghuan Yang, Nan Wu, Sang Young Jeong, Herui Xi, Drajad Satrio Utomo, Badri Vishal, Furkan H. Isikgor, Hendrik Faber, Zhaoheng Ling, Mingjie He, Marco Marengo, Pia Dally, Adi Prasetio, Yu-Ying Yang, Chuanxiao Xiao, Han Young Woo, Kui Zhao, Martin Heeney, Stefaan De Wolf, Leonidas Tsetseris, and Thomas D. Anthopoulos. Solvent-dripping modulated 3d/2d heterostructures for high-performance perovskite solar cells. *Nature Communications*, 16(1):1042, Jan 2025.

[271] Hsien Tsai, Wanyi Nie, Jean-Christophe Blancon, Constantinos C. Stoumpos, Reza Asadpour, Boris Harutyunyan, Amanda J. Neukirch, Rafael Verduzco, Jared J. Crochet, Sergei Tretiak, Laurent Pedesseau, Jacky Even, Muhammad A. Alam, Gautam Gupta, Jun Lou, Pulickel M. Ajayan, Michael J. Bedzyk, Mercouri G. Kanatzidis, and Aditya D. Mohite. High-efficiency two-dimensional ruddlesden–popper perovskite solar cells. *Nature*, 536:312–316, 2016.

[272] Usman Ali Shah, Gyanendra Shankar, Claudia Malerba, Pier Paolo Bonaccini, Francesca Zarotti, Vittoria Novelli, Aldo Di Carlo, Alberto Mittiga, Francesco Biccari, and Emanuele Calabrò. Comparative study of different passivation layers for n-i-p perovskite solar cell for indoor applications. *Solar RRL*, 9(6):2400849.

[273] Xiongzhuo Jiang, Shi Chen, Yang Li, Lihua Zhang, Nan Shen, Guoge Zhang, Jun Du, Nianqing Fu, and Baomin Xu. Direct surface passivation of perovskite

film by 4-fluorophenethylammonium iodide toward stable and efficient perovskite solar cells. *ACS Applied Materials & Interfaces*, 13(2):2558–2565, 2021. PMID: 33416305.

[274] Arindam Mondal, Akash Lata, Aarya Prabhakaran, and Satyajit Gupta. Nanometer-thick {(FPEA)_2PbX_4; X = I and Br} 2d halide perovskite based thin films for pollutant detection and nonconventional photocatalytic degradation. *Materials Advances*, 2:5712–5722, 2021.

[275] Giulia Lucarelli, Francesca De Rossi, Babak Taheri, Thomas M. Brown, and Francesca Brunetti. Phenethylammonium iodide passivation layers for flexible planar perovskite solar cells. *Energy Technology*, 10(11):2200314, 2022.

[276] Walagedara G.A. Pabasara, Udugama K.D.M. Akmal, and Galhenage A. Sewvandi. Simulation-guided investigation of the effect of 2d perovskites on performances of 2d/3d mixed dimensional perovskite solar cells. *Next Energy*, 9:100467, 2025.

[277] Zeynep Gozukara Karabag, Aliekber Karabag, Ummugulsum Gunes, Xiao-Xin Gao, Olga A. Syzgantseva, Maria A. Syzgantseva, Figen Varlioglu Yaylali, Naoyuki Shibayama, Hiroyuki Kanda, Alwani Imanah Rafieh, Roland C. Turnell-Ritson, Paul J. Dyson, Selcuk Yerci, Mohammad Khaja Nazeeruddin, and Gorkem Gunbas. Tuning 2d perovskite passivation: Impact of electronic and steric effects on the performance of 3d/2d perovskite solar cells. *Advanced Energy Materials*, 13(45):2302038.

[278] Reduced hysteresis and enhanced air stability of low-temperature processed carbon-based perovskite solar cells by surface modification. *Electrochimica Acta*, 443:141935, 2023.

[279] Wenchao Dai, Dong Xue, Haru Kimata, Xiangtao Zou, Tomoya Nakamura, At-

sushi Wakamiya, and Kazuhiro Marumoto. Performance improvement mechanism of perovskite solar cells by device interface control. *Solar RRL*, 9, 2025.

[280] Nam Joong Jeon, Jun Hong Noh, Yohan Chan Kim, Won Seok Yang, Seungchan Ryu, and Sang Il Seok. Solvent engineering for high-performance inorganic–organic hybrid perovskite solar cells. *Nature Materials*, 13(9):897–903, 2014.

[281] A. D. Taylor et al. A general approach to high-efficiency perovskite solar cells by any antisolvent. *Nature Communications*, 12(1):1878, 2021.

[282] Y. K. Ren et al. Controllable intermediates by molecular self-assembly for optimizing the fabrication of large-grain perovskite films via one-step spin coating. *Journal of Alloys and Compounds*, 708:287–293, 2017.

[283] Yujun Yao, Xiaoping Zou, Jin Cheng, Dan Chen, Chuangchuang Chang, Tao Ling, and Haiyan Ren. Impact of delay time before annealing mai–pbi2–dmso intermediate phase on perovskite film quality and photo-physical properties. *Crystals*, 9(3):151, 2019.

[284] Junwei Xiang, Chuanzhou Han, Yanjie Cheng, Qiaojiao Gao, Wenjing Hu, Yang Zhou, Anyi Mei, Yinhua Zhou, and Hongwei Han. Recent progress and advances of perovskite crystallization in carbon-based printable mesoscopic solar cells. *Advanced Materials*, 37(9):2415405.

[285] Sanghyun Paek, Cristina Roldán-Carmona, Kyung Taek Cho, Marius Franckevičius, Hobeom Kim, Hiroyuke Kanda, Nikita Drigo, Kun-Han Lin, Mingyuan Pei, Rokas Gegevičius, Hyung Joong Yun, Hoichang Yang, Pascal A. Schouwink, Clémence Corminboeuf, Abdullah M. Asiri, and Mohammad Khaja Nazeeruddin. Molecular design and operational stability: Toward stable 3d/2d perovskite interlayers. *Advanced Science*, 7(19):2001014.

[286] Dewei Ma and Yidan He. Syntheses of needle-shaped layered perovskite (c6h5ch2nh3)2pbi4 bundles via a two-step processing technique. *Journal of Alloys and Compounds*, 696:1213–1219, 2017.

[287] Rishabh Sahani, Neetesh Kumar, Carlo A. R. Perini, Azina Rahmani, Daniel Muñoz, Diana LaFollette, Jack Lawton, Kunal Datta, Ruipeng Li, Juan-Pablo Correa-Baena, Titel Jurca, Cheng-Yu Lai, and Daniela R. Radu. 2d/3d heterostructure halide perovskite thin films through an innovative spray-deposition of bulky organic cation-containing ammonium salts. *Advanced Materials Interfaces*, 12(9):2400823.

[288] Nanoscience Instruments. How to combat electric charge buildup in scanning electron microscopy. `https://www.nanoscience.com/blogs/how-to-combat-electric-charge-buildup-in-scanning-electron-microscopy/`, 2025. Accessed: 2025-11-06.